広島大学学位請求論文

Materials structure physics on ferroelectric titanates and their aerosol deposition films using synchrotron radiation X-ray diffraction

(放射光X線回折を用いた強誘電体チタン酸化合物とそのエアロゾルデポジション膜の構造物性)

２０２１年

広島大学大学院理学研究科
物理科学専攻

安部　友啓

Abstract

Basically, physical properties of ferroelectrics are based on the crystal structure. In this sense, ferroelectric properties can be understood to some extent from the structural information. The possibility of emergence of ferroelectricity and the magnitude of the spontaneous polarization are often deduced from the crystal symmetry and the atomic coordinates. Therefore, ferroelectrics have long been studied as a target for materials structure physics. In this work, structural studies of ferroelectric titanates are conducted using synchrotron radiation X-ray diffraction (SXRD). The level of crystal structure analysis has been extended to the level of visualizing the state of electron polarization in the real space. The mechanism of ceramic coating has been revealed by the state-of-the-arts structural measurement technology. This study is divided into two parts.

Part 1. Visualization of valence electron density distributions of perovskite-type ferroelectrics $PbTiO_3$ and $BaTiO_3$

Perovskite-type oxides with the chemical formula ABO_3 exhibit various dielectric properties such as piezoelectricity and ferroelectricity depending on the combination of *A*- and *B*-site cations. Among them, titanates with the ferroactive Ti ion at the *B*-site such as barium titanate ($BaTiO_3$, BT) and lead titanate ($PbTiO_3$, PT) have been extensively studied. At room temperature, both BT and PT show ferroelectricity in the tetragonal phase with the space group of *P*4*mm*. However, their ferroelectricity is quite different. The spontaneous polarization of PT is significantly larger than that of BT. The phase transition temperature of PT is also fairly higher. It is interesting that the ferroelectric properties differs so much only by the difference in the *A*-site cation. The first-principles calculations have suggested that the covalency on the Ti-O bonds plays an important role for the ferroelectric instability in perovskite-type titanates, and additionally the Pb-O bonds in PT. The SXRD experiment has previously visualized the total electron density distributions of BT and PT in which a direct evidence of the Pb-O covalent bonds in PT is demonstrated. The electrostatic potential distribution of PT is also evaluated from the SXRD data to suggest that the Pb ion is electronically polarized. In this study, a new method to visualize valence electron density distributions is developed, in which a direct evidence of the electronic polarization of the Pb ion in PT is demonstrated by the SXRD experiment. The difference in the ferroelectricity between BT and PT is discussed based on the valence electron density distributions.

SXRD experiments were performed at the powder diffraction beamline BL02B2 in the synchrotron radiation facility SPring-8. The valence electron density distributions were

evaluated by the maximum entropy method (MEM)/Rietveld method. In the analysis of the valence electron density distributions, first, the inner-core electronic configurations of Pb, Ba, Ti, and O atoms were assumed to be [Xe]$4f^{14}5d^{10}$, [Xe], [Ar], and [He]$2s^2$, respectively, and their scattering factors were calculated by first-principles calculations. Then, using the scattering factors and the crystal structure parameters obtained by the Rietveld method, the structure factor of inner-core electrons F^{core} was calculated. The structure factor of valence electrons F^{val} was deduced by subtracting F^{core} from the measured structure factor F^{obs}. Finally, the valence electron density distrbution was determined by MEM using F^{val}. It has been successfully visualized that the lone-pair electrons of the Pb^{2+} ion are localized in the opposite direction to the Pb-O covalent bonds and the Pb ion is electronically polarized in PT in the ferroelectric phase, whereas the Ba ion is not polarized, and is fully ionized to Ba^{2+} in BT. The spontaneous polarization of PT was evaluated as the sum of the ionic polarization and electroinc polarization estimated from the valence electron density distribution. The contribution from the Pb ion to the electronic polarization is significantly large, which is caused by the anisotropic spatial distribution of the p-component-like lone-pair electrons of the Pb ion.

Part 2. Deposition mechanism of ferroelectric $Bi_4Ti_3O_{12}$ films formed by aerosol deposition method

An aerosol deposition (AD) method is a technique to form a ceramic film at room temperature (RT) without firing only by spraying ceramic fine particles onto a substrate. A very dense film is coated, and the film does not easily peel off even if it is mechanically scratched. There are many discussions on the deposition mechanism of the AD method. One of the plausible is that ”when the particle size of ceramic particles is less than a few microns, the particle collision causes plastic deformation and further miniaturization at RT, which forms nascent surfaces on the particle surface and activates them, and the surfaces chemically recombine resulting in a dense ceramic film”. In this study, in order to confirm the deposition mechanism, the structural characteristics of the ferroelectric $Bi_4Ti_3O_{12}$ (BiT) starting powder and the AD film are investigated by SXRD. In previous studies of the BiT AD film, the plate-like particle shapes of the starting powder was simply supposed to be the cause of the *c*-axis orientation during the film growth. However, BiT is known to have a layered crystal structure. Therefore, it is assumed that if the formation and the activation of the nascent surfaces on the particle surface are related to the film deposition, the origin of the *c*-axis orientation of the BiT AD film may be the crystal structure of the starting powder rather than the shapes of ceramic particles. Thus, non-plate-like BiT powder was prepared in this study as the starting powder to confirm the assumption. The orientation mechanism of the BiT AD film is discussed in light of the characteristic chemical bonding of the BiT starting powder which has been revealed in the electron density distribution map.

BiT powders with non-plate-like shapes were synthesized by the solid-state reaction method. SXRD experiments were carried out at BL02B2 in SPring-8. The Rietveld analysis confirmed that the BiT starting powder with non-plate-like shapes had the same crystal structure as the BiT powder with plate-like shapes. The electron density study revealed that the BiT starting powder essentially had a layered crystal structure with layers stacked in the *c*-axis. The BiT AD film showed the *c*-axis orientation even if the starting powder was not plate-like-shaped. These results suggest that the origin of the *c*-axis orientation of the BiT AD film is not due to the shape of the starting powder, but due to the anisotropy of the chemical bonds. Therefore, in the AD process, it is concluded that the ceramic hard coating is formed by the recombination of weakly bonded planes due to the formation and activation of nascent surfaces on the particle surface by impact of particles.

Contents

Part 1: Visualization of valence electron density distributions of perovskite-type ferroelectrics $PbTiO_3$ and $BaTiO_3$

Chapter 1.1: Introduction

§1.1.1. Perovskite-type oxides

A perovskite-type oxide is a general term for oxides that have the same crystal structure as calcium titanate ($CaTiO_3$) which is known as the mineral name for perovskite. The general formula for perovskite oxides is represented by ABO_3. A and B are cations and O is oxygen. The crystal structure with the highest symmetry is the cubic phase (space group: $Pm\bar{3}m$), with A atom at the corner of the unit cell, B atom at the body center position, and O atom at the face center positions. Fig. 1.1.1 shows the crystal structure of the perovskite-type oxide in the cubic phase. The A-site atom is surrounding by 12 oxygens. The B-site atom is surrounded by 6 oxygens and forms a BO_6 octahedron centerd on the B atom.

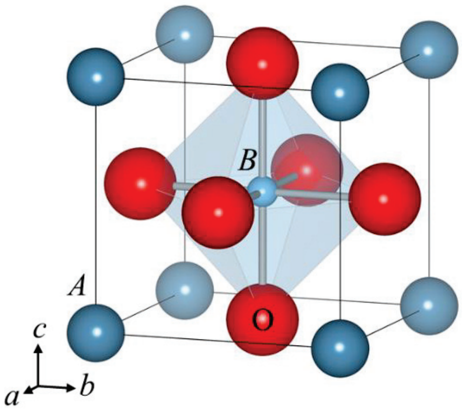

Fig. 1.1.1 Crystal structure of the perovskite-type oxide ABO_3 in the cubic phase (symmetry: $Pm\bar{3}m$). The A-site atom is located at the corner of the unit cell (0, 0, 0). The B-site atom is located at the body center (1/2, 1/2, 1/2). O atoms are located at the face center (1/2, 1/2, 0), (1/2, 0, 1/2) and (0, 1/2, 1/2).

A and *B* are often metal ions. Depending on the combination of the *A* and *B* ions, perovskite-type oxides show various physical properties such as ferroelectricity, energy conversion functionality, superconductivity, electron/ion conductivity, and catalytic function. When the *A* is +3 valent ion and *B* is +3 valent ion, there are bismuth ferrite ($BiFeO_3$), lanthanum aluminate ($LaAlO_3$), and so on. When the *A* is +2 valent ion and *B* is +4 valent ion, there are lead titanate ($PbTiO_3$), barium titanate ($BaTiO_3$), and so on. When the *A* is +1 valent ion and *B* is +5 valent ion, there are potassium niobate ($KNbO_3$), sodium niobate ($NaNbO_3$), and so on. Various ions form perovskite-type crystals.

Many perovskite-type oxides have a cubic structure in the high-temperature high symmetry phase, as shown in Fig. 1.1.1. When the temperature is decreased, the perovskite-type oxides undergo structural phase transition and becomes low symmetry phase. The crystal structure in the low symmetry phase varies greatly depending on the combination of the *A*-site atom and *B*-site atom. Table 1.1.1 shows the structural phase transition temperature and space group of typical perovskite-type oxides [1] [2]. Many of these perovskite-type oxides exhibit interesting physical properties such as dielectric and magnetism, and many studies have been conducted from both basic and applied aspects.

The structural phase transition is a phase transition for a crystal that involves changes in the crystal structure such as atomic displacements and lattice strain. Ferroelectricity and antiferroelectricity emerge when the crystal become a low symmetry structure due to the structural phase transition. The structural phase transition may occur when the normal mode of the transverse wave with low-frequency and temperature sensitivity among lattice vibrations freezes and spontaneous displacement of atoms ocures. As the temperature decreases, the frequency of the normal mode decreases. This is the softening of the phonons, and the softened normal mode is called the soft mode. The mechanism of the softening is generally explained by the anharmonicity of lattice vabrations. When the lattice vibration is anharmonic, the restoring force of the lattice vibration decrease as the temperature decreases, resulting in a decrease in frequency. When the phase transition temperature is reached, the frequency of the soft mode becomes zero, the atomic displacement pattern corresponding to the soft mode freezes, and a low symmetry phase is realized. Which normal mode among lattice vibrations becomes soft mode is determined by the crystal structure, the mass and thermal vibration of constituent atoms, and the interaction between atoms including the bonding state and dipole field [3] [4].

Table 1.1.1. Phase transition temperature and space group change of typical perovskite-type oxides [1] [2].

Material	Phase transition temperature [K]	Space group		
$BaTiO_3$	403	$Pm\bar{3}m$	$\rightarrow$	$P4mm$
	278		$\rightarrow$	$Amm2$
	198		$\rightarrow$	$R3m$
$BaZrO_3$	-		$Pm\bar{3}m$	
$PbTiO_3$	763	$Pm\bar{3}m$	$\rightarrow$	$P4mm$
$SrTiO_3$	105	$Pm\bar{3}m$	$\rightarrow$	$I4/mcm$
	< 0			
$LaAlO_3$	834	$Pm\bar{3}m$	$\rightarrow$	$R\bar{3}c$
$KNbO_3$	708	$Pm\bar{3}m$	$\rightarrow$	$P4mm$
	498		$\rightarrow$	$Amm2$
	263		$\rightarrow$	$R3m$
$KTaO_3$	< 0		$Pm\bar{3}m$	
$PbZrO_3$	505	$Pm\bar{3}m$	$\rightarrow$	$Pbam$
$PbHfO_3$	488	$Pm\bar{3}m$	$\rightarrow$	$R\bar{3}m$
	436		$\rightarrow$	$Pnam$

There are roughly two types of the soft modes that are often observed in perovskite-type dielectrics that undergo a structural phase transition. One is the mode at the center of the Brillouin zone, which is called the Γ_{15} mode and causes a ferroelectric phase transition. The other is the mode at the zone boundary, which is called the M_3 and R_{25} mode. Fig. 1.1.2 shows the Brillouin zone in the cubic structure of the perovskite-type oxides [5]. Notations such as Γ, M and R in phonon mode mean phonons belonging to each point of Γ, M and R in the Brillouin zone.

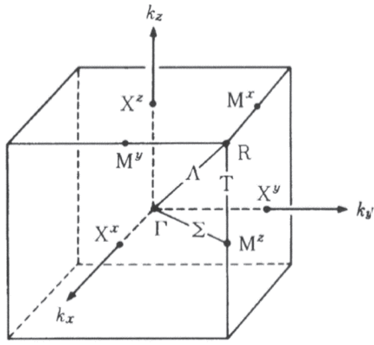

Fig. 1.1.2. Brillouin zone of the perovskite-type oxides in the cubic phase [5].

Γ_{15} mode is transverse optical (TO) mode. The direction of atomic displacements when the Γ_{15} mode freezes is in the ⟨0 0 1⟩ direction. Ferroelectric phase transition occurs when the Γ_{15} mode freezes. Fig. 1.1.3 shows the atomic displacements when the Γ_{15} mode freezes [5], (a) Slater mode, (b) Last mode, and (c) oxygen octahedral displacement mode.

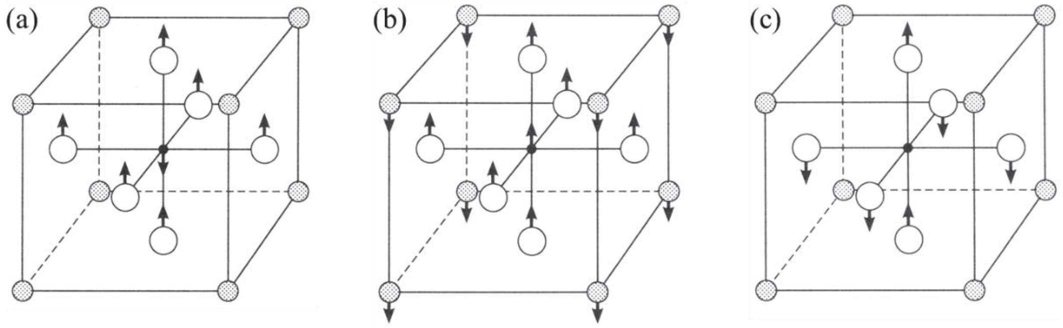

Fig. 1.1.3 Atomic displacements when the Γ_{15} mode freezes [5]. (a) Slater mode, (b) Last mode and (c) oxygen octahedral displacement mode.

M_3 and R_{25} modes are transverse acoustic (TA) modes with rotational displacement of the BO_6 octahedron in the crystal. Fig. 1.1.4 shows the rotational displacements when the M_3 and R_{25} modes freeze [5], (a) the M_3 mode and (b) the R_{25} mode. When the M_3 mode freezes, the upper and lower BO_6 octahedra rotate in the same direction. On the other hand, when the R_{25} mode freezes, the upper and lower BO_6 octahedra rotate in the opposite direction. When these modes freeze, adjacent octahedra always rotate in opposite directions, resulting in a superlattice suructure in a low symmetry phase.

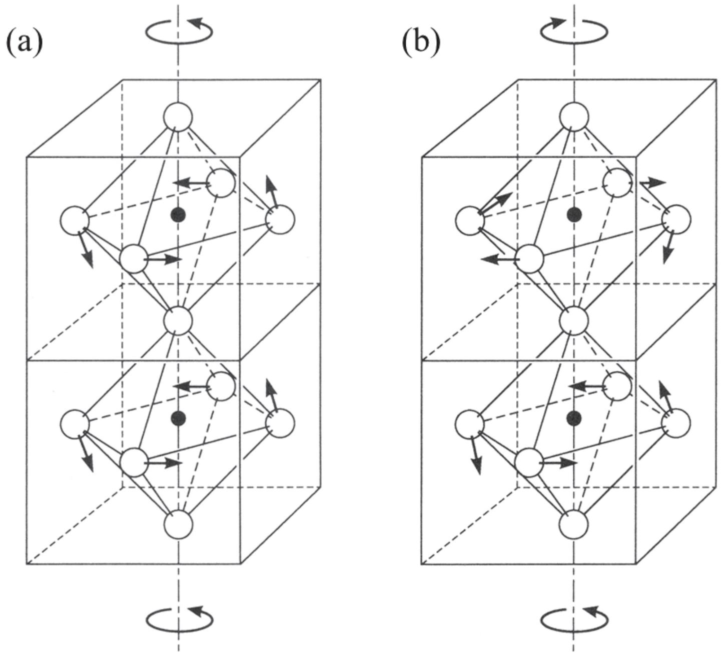

Fig. 1.1.4. Atomic displacements when the M_3 and R_{25} modes freeze [5]. (a) The M_3 mode and (b) the R_{25} mode.

What kind of soft mode exists depends on materials. In genetal, M_3 and R_{25} modes do not freeze for materials that the Γ_{15} mode freezes, while the Γ_{15} mode does not freeze for materials that the M_3 and R_{25} modes freeze. This is known as the separation of the phase transition mode in successive phase transitions. To classify the stability of the perovskite-type structure and the properties of soft modes, classification by a torelance factor t has been proposed. The torelance factor t is expreced by the following equation as a parameter expressing the degree of space around atoms.

$$t = \frac{r_A + r_O}{\sqrt{2}(r_B + r_O)} \tag{1.1.1}$$

r_A, r_B and r_O are the ionic radii of the A-site, B-site, and O atoms, respectively. Shannon's ionic radius is often used as the ionic radius [6]. $t = 1$ indicates that the crystal has an ideal perovskite-type structure. The ideal perovskite-type structure is a dence structure in which A-site and B-site ions are in close contact with adjacent O ions. When $t > 1$, there is more spatial space around the B site than around the A site, while when $t < 1$, there is more spatial space around the A site than around the B site. Table 1.1.2 shows the ionic radii of the A-site atom and B-site atom and the tolerance factor t of typical perovskite-type dielectrics. In the calculation of the tolerance factor, by considering only the coordinations of the first neighboring atoms, O atoms, the ionic radii in the case of 12 coordinations and 6 coordinations were used for the *A*-site atom and *B*-site atom, respectively. For the O atom, 2-coordinated ionic radius of 1.35 Å, which is considerd to be coordinated only with the *B*-site atoms which is the first neighboring atoms, and 6-coordinated ionic radius of 1.40 Å considering coordination with the *A*-site atoms which is the second neighboring atoms were used.

Table 1.1.2. Formal valence and ionic radius of the *A*-site atom and *B*-site atom and tolerance factor of perovskite-type dielectrics. The tolerance factor is calculated by considering that the *A*-site atom has 12 coordinates, the *B*-site atom has 6-coordinates. For O atoms, 2-coordinated ionic radius of 1.35 Å and 6-coordinated ionic radius of 1.40 Å are used.

Material	*A*-site atom		*B*-site atom		Tolerance factor *t*	
	Formal valence	r_A (Å)	Formal valence	r_B (Å)	r_O = 1.35 Å	r_O = 1.40 Å
$BaTiO_3$	2+	1.61	4+	0.605	1.071	1.062
$PbTiO_3$	2+	1.49	4+	0.605	1.027	1.019
$KNbO_3$	1+	1.64	5+	0.64	1.062	1.054
$KTaO_3$	1+	1.64	5+	0.64	1.062	1.054
$LaAlO_3$	3+	1.36	3+	0.535	1.017	1.009
$CeAlO_3$	3+	1.34	3+	0.535	1.009	1.001
$SrTiO_3$	2+	1.44	4+	0.605	1.009	1.002
$SrZrO_3$	2+	1.44	4+	0.72	0.953	0.947
$BiFeO_3$	3+	1.45	3+	0.645	0.992	0.985
$PbZrO_3$	2+	1.49	4+	0.72	0.970	0.964
$PbHfO_3$	2+	1.49	4+	0.71	0.975	0.969
$NaNbO_3$	1+	1.39	5+	0.64	0.974	0.967
$AgNbO_3$	1+	1.37	5+	0.64	0.966	0.950
$LiNbO_3$	1+	1.25	5+	0.64	0.924	0.919
$LiTaO_3$	1+	1.25	5+	0.64	0.924	0.919

Figure 1.1.5 shows a correlation diagram of various perovskite-type dielectrics arranged by the ionic radius of the *A*-site atom and the ionic radius of the *B*-site atom, the so-called Goldschmidt diagram [7]. The structure of ABO_3-type crystals is roughly divided into two types. One is the perovskite-type structure which prototype structure is cubic structure (space group: $Pm\overline{3}m$). The other is an ilmenite-type structure and $LiNbO_3$-type ilmenite-type structure. In Fig. 1.1.5, among the perovskite-type structures, materials

which soft mode is the Γ_{15} mode and the R_{25} mode are shown in red and blue, respectively. $SrTiO_3$, a perovskite-type oxide that the Γ_{15} mode is soften with freezing of the R_{25} mode is shown in purple. $KTaO_3$, $BaSnO_3$ and $BaZrO_3$ that do not undergo structural phase transition are shown in black. Materials having ilmenite-type and $LiNbO_3$-type ilmenite-type structure are shown in green. Since the ionic radius of the O atom changed depending on the coordination number, the value of the tolerance factor differs slightly between Fig. 1.1.5 (a) and (b). In general, for dielectrics with $t > 1$, the freezing of the zone-centered mode, the Γ_{15} mode, which causes ferro atomic displacements often occurs. On the other hand, for dielectrics with $t < 1$, the freezing of the zone boundary modes, the M_3 and R_{25} modes, which causes the anti-ferro atomic displacements often occurs. R. Blinc *et al.* proposed a method for classifying materials that undergo displacive structural phase transitions as shown in Table 1.1.3 [8]. Glazer *et al.* devised the symbol "Glazer notation" to classify features of anti-ferro atomic displacement such as octahedral rotation and tilt for materials that undergo the phase transition due to the rotational displacement of the oxygen octahedron [9]. Table 1.1.4 shows the Glazer notaion classifies into 23 types [10].

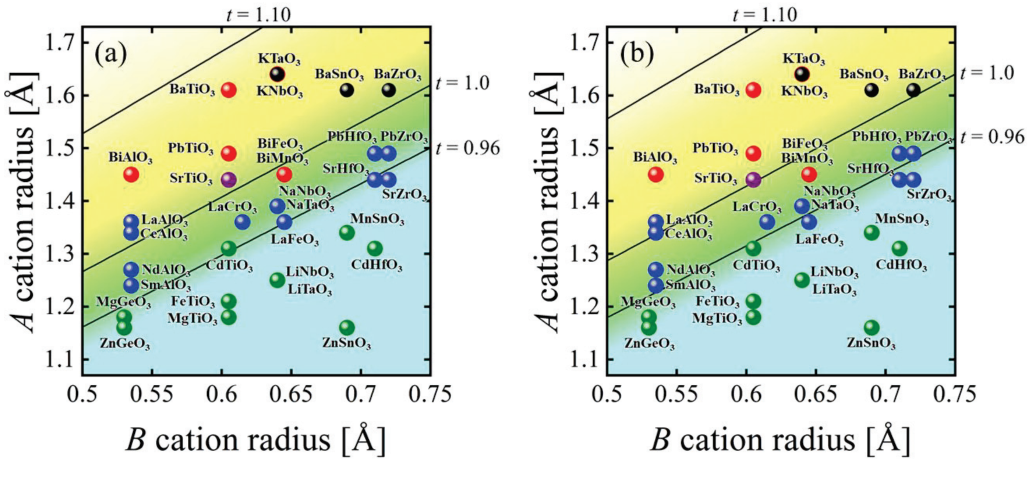

Fig. 1.1.5. Goldschmidt diagram [7]. The ionic radius of O atom is (a) 1.35 Å and (b) 1.40 Å. Red and blue solid circle indicate perovskite-type oxides which soft mode is the Γ_{15} mode and the R_{25} mode, respectively. Purple solid circle indicates $SrTiO_3$, a perovskite-type oxide that the Γ_{15} mode is soften with freezing of the R_{25} mode. Black solid circle indicates $KTaO_3$, $BaSnO_3$ and $BaZrO_3$ that do not undergo structural phase transition. Green solid crcle indicates materials having ilmenite-type and $LiNbO_3$-type ilmenite-type structure.

Table 1.1.3. Classification of materials that undergo distortive structural phase transition [8].

	Ferroelectrics	Antiferroelectrics	Other structural phase transition
Phase transition due to ferro atomic displacement	$BaTiO_3$ $PbTiO_3$		SiO_2 NH_4Cl
Phase transition due to antiferro atomic displacement	$LiTaO_3$ $BiFeO_3$	$PbZrO_3$	$SrTiO_3$ NH_4Br

Table 1.1.4. Classification of space groups by Glazer notation [10].

Tilt system number	Tilt system symbol	Space group	Tilt system number	Tilt system symbol	Space group
1	$a^+ b^+ c^+$	*Immm*	13	$a^- b^- b^-$	*I2/a*
2	$a^+ b^+ b^+$	*Immm*	14	$a^- a^- a^-$	$R\bar{3}c$
3	$a^+ a^+ a^+$	$Im\bar{3}$	15	$a^0 b^+ c^+$	*Immm*
4	$a^+ b^+ c^-$	*Pmmn*	16	$a^0 b^+ b^+$	*I4/mmm*
5	$a^+ a^+ c^-$	$P4_2/nmc$	17	$a^0 b^+ c^-$	*Cmcm*
6	$a^+ b^+ b^-$	*Pmmn*	18	$a^0 b^+ b^-$	*Cmcm*
7	$a^+ a^+ a^-$	$P4_2/nmc$	19	$a^0 b^+ c^-$	*I2/m*
8	$a^+ b^- c^-$	$P2_1/m$	20	$a^0 b^- b^-$	*Imma*
9	$a^+ a^- c^-$	$P2_1/m$	21	$a^0 a^0 c^+$	*P4/mbm*
10	$a^+ b^- b^-$	*Pnma*	22	$a^0 a^0 c^-$	*I4/mcm*
11	$a^+ a^- a^-$	*Pnma*	23	$a^0 a^0 a^0$	$Pm\bar{3}m$
12	$a^- b^- c^-$	$F\bar{1}$			

§1.1.2. Crystal structure and ferroelectric phase transition of $BaTiO_3$ and $PbTiO_3$

Many basic and applied researchs have been conducted especially on $BaTiO_3$ (BT) and $PbTiO_3$ (PT), among the perovskite-type ferroelectrics. BT and PT transform from the cubic structure (space group: $Pm\bar{3}m$) to tetragonal structure (space group: $P4mm$) due to ferro atomic displacement in the <0 0 1> direction, and exibit ferrelectricity. BT and PT have the same space group in the tetragonal phase and the directions of spontaneous polarization P_S of BT and PT in the tetragonal phase are the same direction, *c*-axis direction. However, the phase transition temperature T_C, spontaneous atomic displacement pattern, and magnitude of P_S are different.

BT has successive phase transitions, from cubic $Pm\bar{3}m$ phase to tetragonal $P4mm$ phase at $T_C = 403$ K, to orthorhombic $Amm2$ phase at $T_C = 278$ K, to rhombohedral $R3m$ phase at $T_C = 198$ K with freezing of the Γ_{15}^X, Γ_{15}^Y and Γ_{15}^Z modes [11]. On the other hand, PT undergoes only single-phase transition, from cubic $Pm\bar{3}m$ phase to tetragonal $P4mm$ phase at $T_C = 763$ K with freezing of one of the Γ_{15}^X, Γ_{15}^Y and Γ_{15}^Z modes [12]. Fig. 1.1.6 shows model diagrams of atomic displacements of BT and PT in the tetragonal phase [13]. The atomic displacements pattern of BT is represented by the Slater mode, while that of PT is represented by a linear combination of the Slater mode and Last mode. In BT, which is dominated by the Slater mode, the displacement directions of Ti and O atoms are opposite, while in PT, which is dominated by the Last mode, the displacement directions of Ti and O atoms are the same. In addition, the atomic displacements of PT are larger than those of BT, and the tetragonality, *a*-axis to *c*-axis ratio used as a measure of tetragonal strain, is 1.011 for BT [14] and 1.065 for PT [15] at room temperature (RT). The value of P_S at RT is reported to be 26 μC/cm^2 for BT [16] and 75 μC/cm^2 for PT [17].

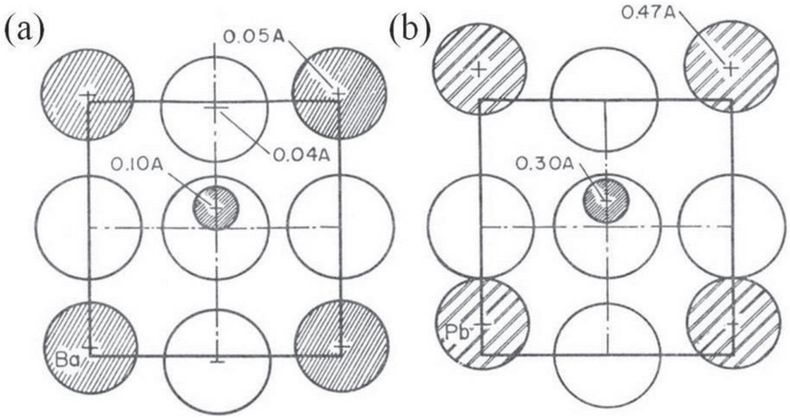

Fig. 1.1.6 Model diagram of atomic displacements of (a) $BaTiO_3$ and (b) $PbTiO_3$ [13].

In addition to BT and PT, $KNbO_3$ (KN) is one of the perovskite-type ferroelectrics that has the tetragonal structure with a space group of $P4mm$ in the ferroelectric phase. Table 1.1.5 shows the ferroelectric phase transition temperature T_C, the tetragonality c/a, measured spontaneous polarization P_S^{obs}, and calculated spontaneous polarization P_S^{cal} of BT, PT and KN [18] [19] [20] [21] [22]. Here, P_S^{cal} is calculated by a point charge model using the ferro atomic displacement obtained by the crystal structure analysis, assuing that each ion is a point charge with an ideal formal valence. Comparing these materials, the larger c/a, the higher T_C and P_S^{obs}. P_S^{obs} is larger than P_S^{cal} in these materials, which means that each atom in the crystal is not an ion with the ideal valence, and it is inappropriate to approximate each ion to the point charge. In other words, in order to understand the mechanism of spontaneous polarization from the crystal structure, it is necessary to conider the spread of electron charge in the crystal and understand the ionic state and electronic polarization of each atom.

Table 1.1.5. Ferroelectric phase transition temperature T_C, the tetragonality c/a, measured spontaneous polarization P_S^{obs}, and calculated spontaneous polarization P_S^{cal} of $BaTiO_3$, $PbTiO_3$ and $KNbO_3$ [18] [19] [20] [21] [22]. P_S^{cal} is calculated based on the point charge model.

Material	T_C [K]	c/a	P_S^{obs} [μC/cm^2]	P_S^{cal} [μC/cm^2]
$BaTiO_3$	403	1.011	26	19
$PbTiO_3$	763	1.065	75	54
$KNbO_3$	691	1.017	31	26

§1.1.3. Ferroelectric phase transition of $BaTiO_3$ and $PbTiO_3$ from the viewpoint of electronic states

Ionic bonds are one of the bonds between atoms that form perovskite-type crystals. However, the anisotropic atomic displacements realized in perovskite-type ferroelectrics cannot be explained only by the ionic bonds. The electrostatic interaction, which is the main interaction of the ionic bonds, is a long-range force. Since the electrostatic force is an isotropic force, the space group of the perovskite-type crystal should be the most symmetric $Pm\bar{3}m$ when only the electrostatic force is acting. In addition, when the distance between atoms becomes small and electrons overlap, a repulsive force is generated due to Pauli's principle, and the atoms cannot approach each other anymore. Since such a repulsive force works evenly around the *A* site and *B* site, the space group should be $Pm\bar{3}m$. In other words, the symmetry of $Pm\bar{3}m$ of the perovskite-type crystals is not broken, and the low symmetry phase does not emerge only by the electrostatic force, that is, ionic bonds, and repulsive force. In 1975, G. A. Samara *et al*. pointed out that the short-range interaction between atoms, that is, covalent bonds, is important to cause the polar atomic displacement [23].

It has been pointed out from the first-principles calculations that orbital hybridization between Ti and O atoms is crucial to allow ferroelectricity of BT and PT [24] [25]. It has been also demonstrated that the orbital hybridization between the Pb and O atoms plays an important role in the ferroelectricity of PT. It is said that the orbital hybridization between the Pb and O atoms localizes the lone-pair electrons of the Pb ion and increases the contribution of electronic polarization to the sponataneous polarization, resulting in huge spontaneous polarization. The density of states [25] and band structure [24] in the ferroelectric phase of PT obtained by first-principles calculations are shown in Fig. 1.1.7 and Fig. 1.1.8, respectively. By changing from the cubic phase to tetragonal phase, the entire density of states distributions of the 3d orbital of the Ti atom and the 6s orbital of the Pb atom shift to low energy. The energy of the 2p orbital of the O atom is similar to the energies of the 3d orbital of the Ti atom and 6s orbital of the Pb atom. These results indicate that the atomic displacements due to the ferroelectric phase transition are accompanied by the orbital hybridization of Ti 3d - O 2p and Pb 6s - O 2p. Since the orbital hybridization of Ti 3d – O 2p is the same for BT [24], it is expected that the orbital hybridization between the Pb and O atoms will cause the large *c*/*a* and spontaneous polarization observed in PT. Figure 1.1.9 shows the valence electron density distribution of PT in the ferroelectric phase obtained by the first-principles calculations [25]. The distributions when the displacement of the Ti atom is (a) 0 Å, (b) 0.08 Å, (c) 0.16 Å and (d) 0.21 Å are shown. The larger the displacement of the Ti atom, the more the valence electron density distribution of the Pb atom becomes distributed in a cap shape. This anisotropic distribution is due to the localizarion of lone-pair electrons, and it seems that electronic polarization exists in the Pb atom.

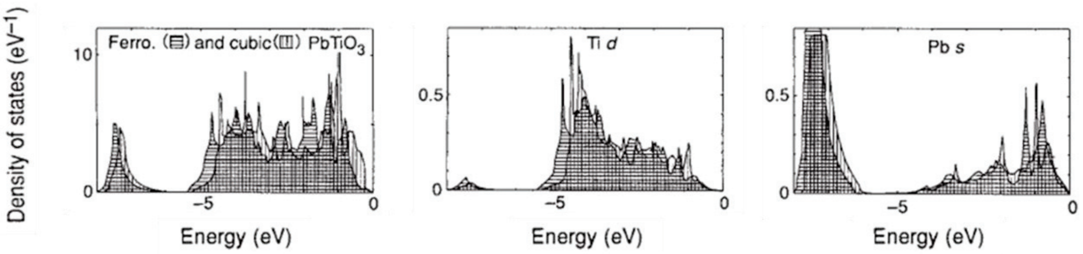

Fig. 1.1.7 Density of states of $PbTiO_3$ obtained by the first-priciples calculations [25]. Vertical and horizontal stripes indicate the density of states in the cubic and tetragonal phases, respectively.

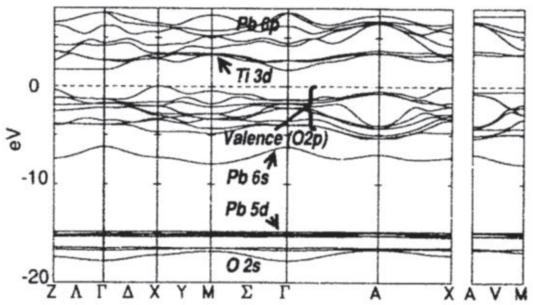

Fig. 1.1.8. Band structure of $PbTiO_3$ in the ferroelectric phase obtained by the first-principles calculations [24].

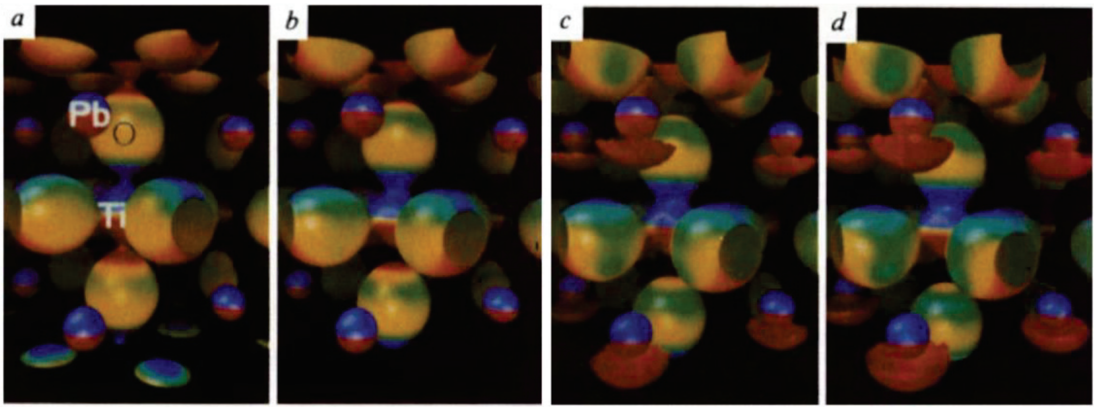

Fig. 1.1.9. Valence electron density distribution of $PbTiO_3$ in the ferroelectric phase obtained by the first-principles calculations [25]. The distributions when the atomic displacement of the Ti atom is (a) 0 Å, (b) 0.08 Å, (c) 0.16 Å and (d) 0.21 Å. The isosurface level is 0.26*e* Å^{-3}. The color of the isosurface indicates the *z* compornent of the electric field in the crystal.

In 2000, H. Miyazawa *et al.* reported that in addition to the strong hybridization of Pb 6s- O 2p, the high ferroelectricity of PT is induced by the hybridization of Pb 6p – O 2p [26]. Fig. 1.1.10 shows the partial density of state PT in the ferroelectric phase obtained by first-principles calculations. The energies of the electrons occupying Ti 3d and O 2p, and Pb 6s and O 2p at the top of the valence band are about the same, which indicates that there are orbital hybridizations in Ti 3d - O 2p and Pb 6s – O 2p. More specifically, in Fig. 1.1.10 (b), not only Pb 6s but also Pb 6p is hybridized with O 2p.

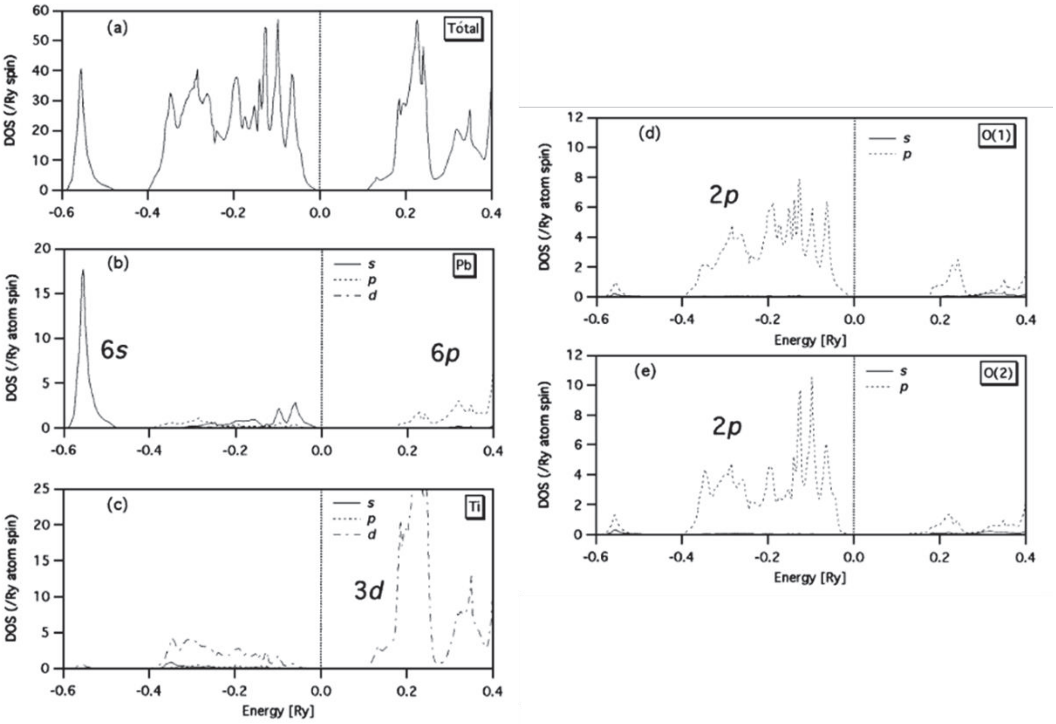

Fig. 1.1.10 Partial density of state of $PbTiO_3$ in the ferroelectric phase [26]. (a) Total density of state and partial density of state of (b) Pb, (c) Ti, (d) O(1), and (e) O(2). O(1) and O(2) represent the O atom in the first and second nearest position to the Ti atom, respectively. Energy = 0 indicates the top of the valence band.

§1.1.4. Charge density study by synchrotron radiation X-ray diffraction.

The combination of synchrotron radiation powder X-ray diffraction experiments and the maximum entropy method (MEM) is a powerful tool to elucidate experimentally the electronic states related to the ferroelectricity as pointed out in the first-principles calculations.

In 2001, Kuroiwa *et al.* performed powder X-ray diffraction experiments using high-energy synchrotron radiation and determined the total electron density distributions of $BaTiO_3$ and $PbTiO_3$ experimentally for the first time by the MEM/Rietveld analysis [27]. Fig. 1.1.11 and Fig. 1.1.12 show the two-dimensional (2D) electron density distributions of BT and PT in the tetragonal phase for (a) (1 0 0) plane and (b) (2 0 0) plane, respectively. The orbital hybridizations between not only the Ti-O bond but also Pb-O bond were visualized as predicted by the first-principles calculations. In 2006, using the same structure factors $F(h\ k\ l)$, the electrostatic potential distribution and the electric field distribution of PT in the tetragonal phase were visualized by using the Ewald method [28]. Fig. 1.1.13 shows (a) the electrostatic potential and (b) electric field derived from the electrostatic potential, respectively. The *z*-compornent are shown as color on the electron density isosurface of $0.84e$ Å^{-3}. In Fig. 1.1.13 (a), Ti is a cation and O is an anion. It should be noted that there is a color distribution on the electron density isosurface of Pb i.e., electronic polarization is observed.

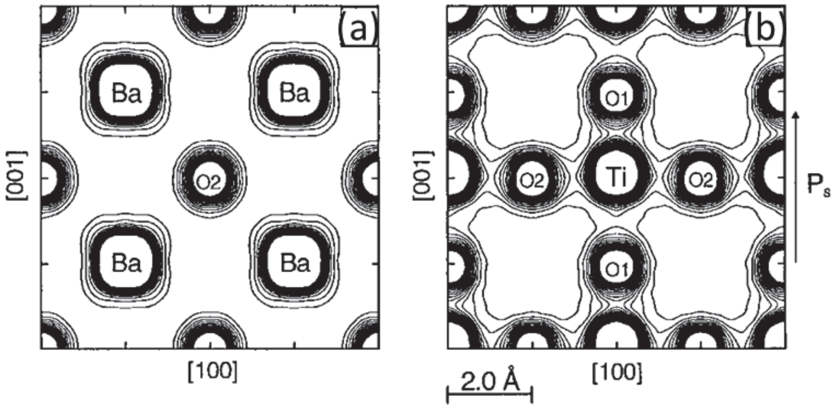

Fig. 1.1.11. 2-dimensional total electron density distribution of $BaTiO_3$ in the tetragonal phase. [27]. (a) (1 0 0) plane and (b) (2 0 0) plane. Contour lines are drawn from $0.4e$ Å^{-3} to $2.0e$ Å^{-3} with $0.2e$ Å^{-3} step.

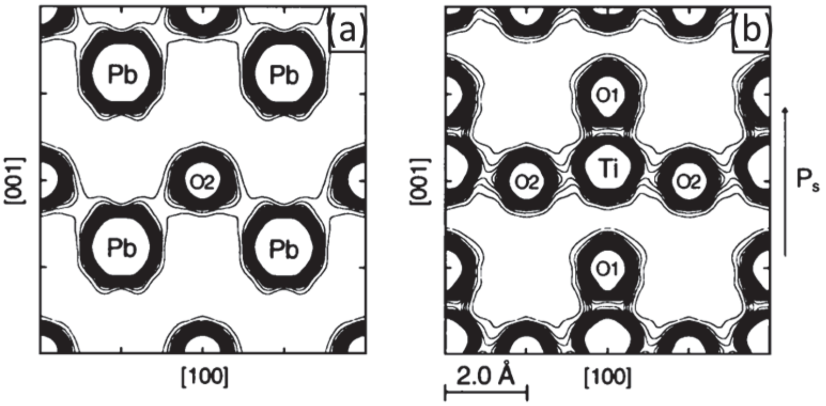

Fig. 1.1.12. 2-dimensional total electron density distribution of $PbTiO_3$ in the tetragonal phase. [27]. (a) (1 0 0) plane and (b) (2 0 0) plane. Contour lines are drawn from 0.4*e* $Å^{-3}$ to 2.0*e* $Å^{-3}$ with 0.2*e* $Å^{-3}$ step.

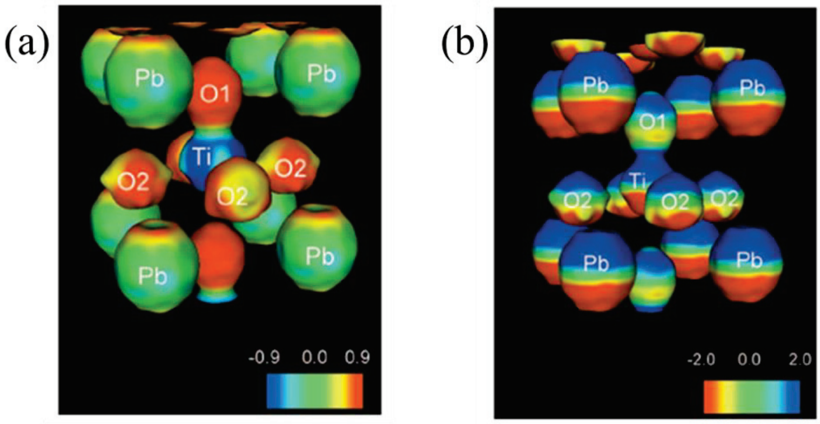

Fig. 1.1.13. (a) Electrostatic potential and (b) electric field of $PbTiO_3$ by synchrotron radiation X-ray diffraction experiment [28]. The electrostatic potential and electric field were calculated based on the Ewald method using observed structure factors of $PbTiO_3$. The *z*-component of the electrostatic potential and electric field are colored on the electron density isosurface of 0.86 *e* $Å^{-3}$. The color range is (a) -0.9*e* $Å^{-1}$ (red) to 0.9*e* $Å^{-1}$ (blue) and (b) -2.0*e* $Å^{-2}$ (red) to 2.0*e* $Å^{-2}$ (blue).

§1.1.5. Purpose

The perovskite-type oxides *AB*O_3 which show various physical properties depending on the combination of *A*- and *B*-site atoms have been studied for a long time. In 1975, G. A. Samara *et al*. pointed out that short-range interactions due to the covalent bonding between atoms as well as long-range electrostatic interactions due to the ionicity of the atoms are important to induce the atomic displacements realized in the perovskite-type ferroelectrics [23]. At the end of the 20th century, a computational physics approach to derive electronic state in the crystal structure without making any assumption was applied to perovskite-type ferroelectrics, which made it possible to discuss ferroelectrics based on electron theory in addition to the theoretical study of ferroelectrics which had been mainly based on phenomenology and shell models. The first-principles calculations suggested that the tetragonal structure of ATiO$_3$ was caused by the orbital hybridization between Ti and O [24] [25].

At the same time, there was a major development in the field of experiments. Synchrotron radiation was used to increase the brilliance of X-rays, and the spatial distribution of the total electron in crystals was able to be determined. In 2001, Y. Kuroiwa *et al*. performed powder X-ray diffraction experiments using high-energy synchrotron radiation and determined the total electron density distributions of BaTiO$_3$ and PbTiO$_3$ by MEM/Rietveld analysis [27]. Not only the orbital hybridization between the Ti-O bond but also that between the Pb-O bond was demonstrated. In 2006, the electrostatic potential distribution and electric field distribution of the PbTiO$_3$ in the ferroelectric phase were visualized to suggest the electronic polarization of the Pb ion [28].

In this study, a method to visualize the electron density distribution of valence electrons is developed. The total and valence electron density distributions of PbTiO$_3$ and BaTiO$_3$ are determined to discuss the difference of ferroelectrisity between PbTiO$_3$ and BaTiO$_3$. Synchrotron radiation X-ray powder diffraction experiments were performed using a large Debye–Scherrer camera installed at the powder diffraction bemline BL02B2 in the synchrotron radiation facility SPring-8 and the electron density distributions were analyzed. In order to discuss at the valence electron level, diffraction data with a high statistical accuracy over a wide Q range from low-Q to high-Q were measured. To determine the valence electron density distributions, first, structure factors of inner-core electrons $F_{\mathrm{cal}}^{\mathrm{core}}$ is calculated by assuming that the inner-core electron configrations of Pb, Ba, Ti, and O are [Xe]$4f^{14}5d^{10}$, [Xe], [Ar], and [He]$2s^2$, respectively. Then the structure facture of valence electrons F^{val} is estimated by subtracting $F_{\mathrm{cal}}^{\mathrm{core}}$ from the observed structure factor $F_{\mathrm{obs}}^{\mathrm{total}}$. Finally, the valence electron density distribution are analyzed by Maximum entropy method using F^{val}.

Chapter 1.2: Experiment

§1.2.1. Sample preparation

PbTiO$_3$ single crystals were grown by the flux method as shown in Fig. 1.2.1. PbO (99.99%) and TiO$_2$ (99.99%) were used as raw materials. The raw material powders were mixed at the PbO:TiO$_2$ ratio of 86:14. The mixture was put into a platinum crucible and heated at 1100 °C for more than 10 h in air. The mixture was slowly cooled to 1000 °C at a rate of 4 – 8 °C/h followed by cooling to room temperature. To remove the flux, the obtained PT single crystals were washed by an aqueous solution of nitric acid. The PT single crystals were grinded in an agate mortar to obtaine PT powder sample. The PT single crystals were provided by Prof. Yuji Noguchi in Kumamoto University.

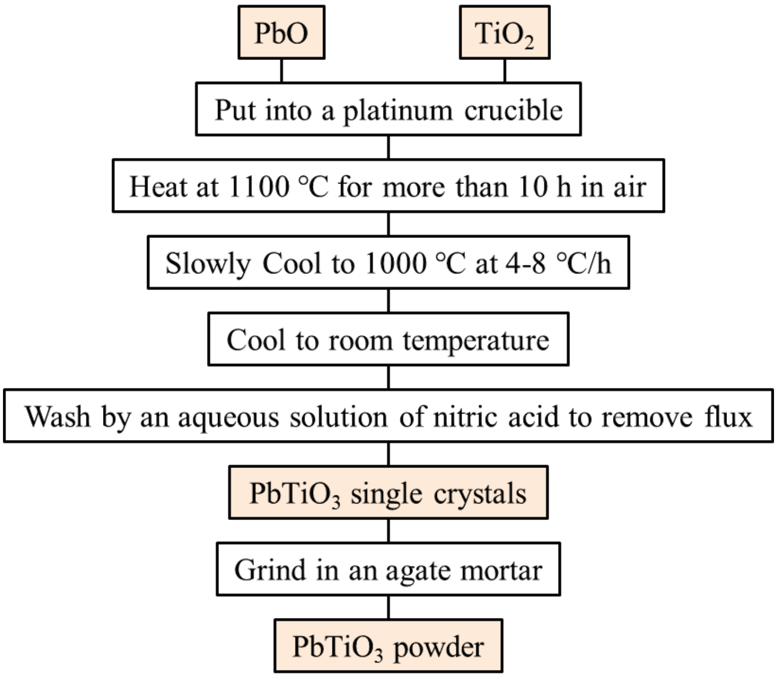

Fig. 1.2.1. Sample preparation procedure of PbTiO$_3$ powder.

BT-05 (Sakai Chemical Industry Co., Ltd.) with the particle size of 500 nm was prepared as the BaTiO$_3$ powder sample. When BT is left in the air, carbon dioxide gas is often absorbed on the surface of BT particles, and barium carbonate (BaCO$_3$) is formed. The process of removing as much BaCO$_3$ as possible was carried out. BaCO$_3$ is known to be decomposed by acetic acid CH_3COOH. The reaction formula is represented as follows.

$$CH_3COOH + BaCO_3 \rightarrow (CH_3COO)_2Ba + CO_2 + H_2O \tag{1.2.1}$$

$BaCO_3$ was removed by washing the surface of BT particles with acetic acid, further washing with water and then drying.

The powder samples of PT and BT were sealed in a glass capillary with an inner diameter of 0.2 mm.

§1.2.2. Synchrotron radiation X-ray diffraction experiments at SPring-8 BL02B2

In this study, synchrotron radiation X-ray diffraction experiments were perfomed at the powder diffraction beamline BL02B2 in SPring-8, a large synchrotron radiation facility constructed in Harima Science Park City, Hyogo Prefecture. Synchrotron radiation is the light emitted in the tangential direction when a charged particle accelerated to near the speed of light is bend by a magnetic field. The advantage of the synchrotron radiation powder diffraction experiment is that the intensity correction due to extinction or absorption effects is not required. The extinction effect means that the diffraction intensity from the crystal deviates from the value expected from the kinematic diffraction theory due to multiple diffraction inside the crystal. The absorption effect is the effect that the X-ray intensity is weakened by the core electron excitation of the elements contained in the sample. These two effects deteriorate the accuracy of intensity of Bragg reflections especially at the low-angle range. Low-angle reflections contain much information about the outer-shell electrons. If these reflection intensities are not estimated correctly, reliable analysis results cannot be obtained. In the synchrotron radiation powder X-ray diffraction, since a powder sample with a small crystallite size, and synchrotron radiation X-rays with extremely high brightness and short wavelength (high energy) are used, the extinction effect and absorption effect can be ignored [29]. Besides, by using the synchrotron radiation with excellent angular resolution, the overlap between Bragg reflections can be minigated. The overlap of Bragg reflections is a drawback of the powder X-ray diffraction, but the use of synchrotron radiation makes it easier to reduce the overlap of the Bragg reflections compared to laboratory X-ray diffraction experiments.

SPring-8 is one of the largest synchrotron radiation facility in the world. The emitted light has a wide energy range from vacuum ultraviolet rays to hard X-rays and has the highest brightness in the world. The brightness of SPring-8 is about 100 million times higher than the brightness obtained from conventional X-ray generators. It is possible to measure weak diffracted light from a small sample that could not be measured with conventional indoor light sources in short time. In addition, high energy gamma rays and infrared rays can be also used. High-energy synchrotron radiation can be used as a driving force for chemichal reactions in addition to structural analysis and is therefore applied in a wide range of fields such as life science, medicine, and industry. The generation process of synchrotron radiation is shown below. First, an electron beam generated by an electron gun is accelarated by a linear accelarator to 1 GeV. The electron beam is accelerated to 8 GeV with a synchrotron and injected into a storage ring with a circumference of 1436 m. Synchrotron radiation is generated by the bending magnet and the insertion device in the strage ring while maintaining the energy of 8 GeV. The synchrotron radiation is guided to the hatches inside and outside the strage ring through the beam line and used for various experiments.

SPring-8 BL02B2 is a beam line for powder diffraction using a bending magnet as the light source. Fig. 1.2.2 shows a scematic diagram of the optical system of BL02B2. The optical system of BL02B2 is mainly composed of a vertical focusing mirror and a double-crystal monochromator. The vertical focusing mirror is installed for the purpose of removing high frequency compornent, etc., and it is used properly depending on the energy E of the emitted light, Si when $E \leq 15.5$ keV, Ni when $15.5 \text{ keV} \leq E \leq 28.2$ keV and Pt when $28.3 \text{ keV} \leq E$. The double-crystal monochromator is installed for the purpose of improving parallelism and energy resolution. The (1 1 1) plane of the Si dispersive crystal is normally used. Energy up to 37 keV can be used, and energy resolution $\Delta E/E$ is about 2×10^{-4}.

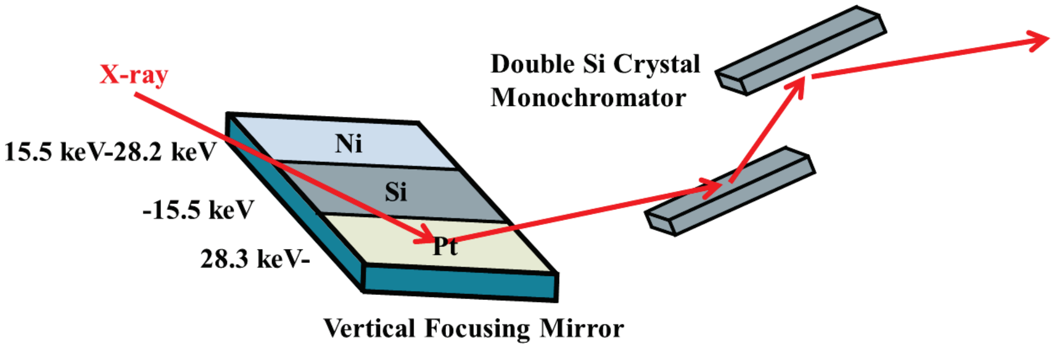

Fig 1.2.2. Schematic view of the optical system of SPring-8 BL02B2.

A large Debye–Scherrer camera is installed in the experimental hatch of SPring-8 BL02B2. Fig. 1.2.3 shows a photograph and schematic disgram of the large Debye–Scherrer camera [30] [31]. A curved imaging plate (IP) camera with a camera radius of 286.48 mm and a MYTHEN camera with a camera radius of 477.46 mm are mounted on the 2θ axis. The sample enclosed in a capillary is fixed on the ω-axis, and X-rays are exposed for measurements. During exposure, the sample continues to rotate around the ω-axis to minimize the nonuniformity of the diffracted X-ray intensities on the Debye–Sherrer ring due to the particle size distribution of the sample. This is particularly important for obtaining reliable powder diffraction patterns. The center axis alignment of the sample is adjusted by moving each angle of the 5-axis goniometer head so that the sample does not move due to the rotation of the ω-axis on the TV monitor using the CCD camera mounted on the lower side of the camera. For the temperature dependence experiments, a He gas circulation refrigerator that can control the temperature at a low temperature of 15 - 300 K, a low temperature N_2 gas flow device that can control the temperature at a temperature of 90 - 300 K, and a high temperature N_2 gas flow device that can control the temperature at a high temperature of 300 – 1100 K are installed.

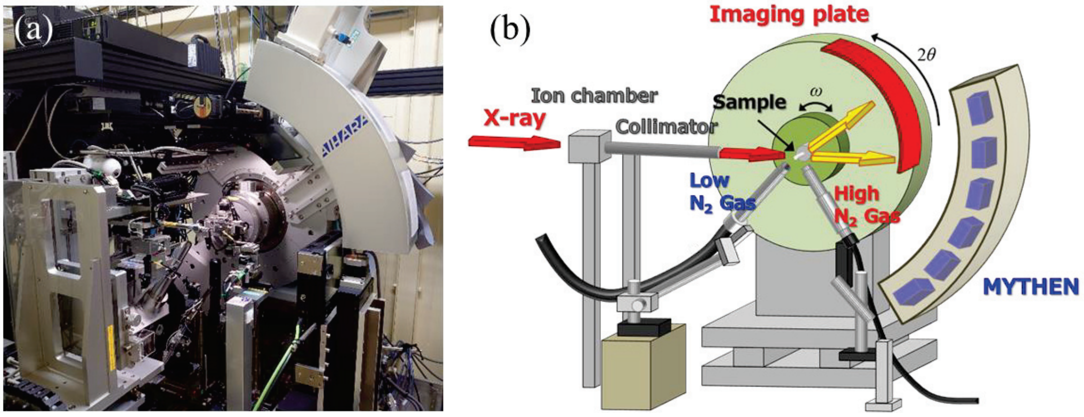

Fig. 1.2.3. Large Debye–Scherrer camera installed at SPring-8 BL02B2. (a) Photograph and (b) Schematic view [30] [31].

§1.2.3. Experimental conditions

In this study, diffraction patterns were measured by using the above experimental equipments. When deciding the energy of the synchrotron radiation to be used, it is necessary to avoid the energies such that the energy E of the synchrotron radiation is slightly higher than the K-edge energy of the constituent elements. Fig. 1.2.4 shows the energy dependence of the linear absorption coefficient of (a) Pb, (b) Ba, (c) Ti and (d) O. When an energy slightly higher than the K-edge energy of each element is irradiated, the electron in the K-shell jumps out of the binding of the nucleus, which causes the electrons in the high energy state to transition to the electron orbital of the vacant inner shell. At that time, the energy difference is emitted as characteristic X-rays. The characteristic X-ray is also called fluorescent X-ray and causes an increase in background intensity. Normally, energy smaller than the absorption edge is used to reduce the background intensity.

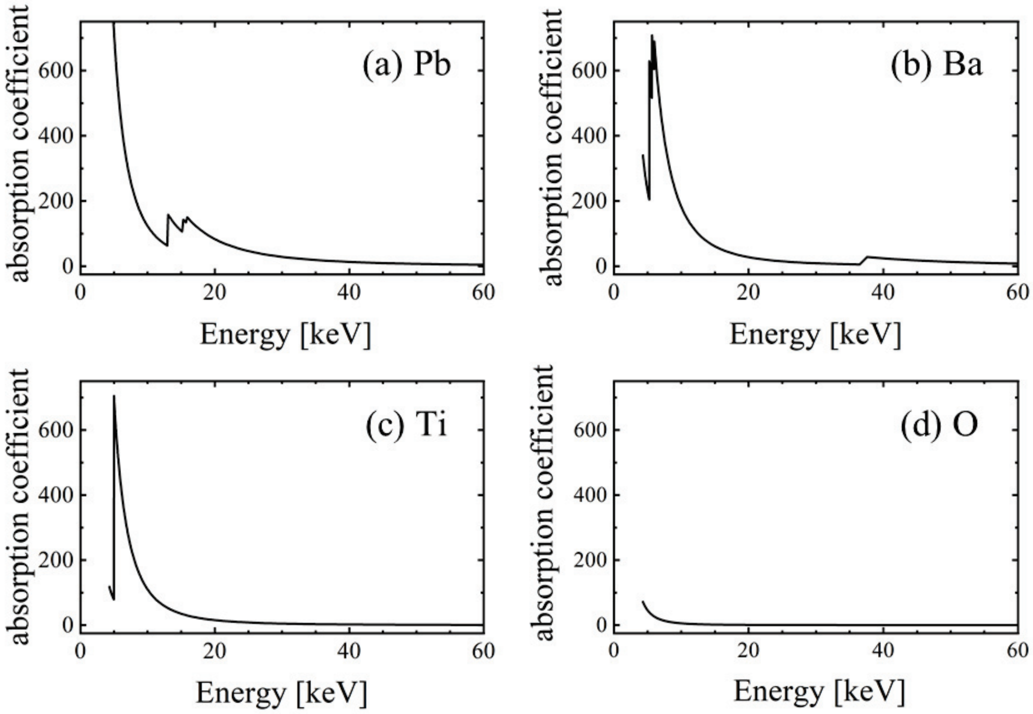

Fig. 1.2.4. Energy dependence of the absorption coefficient for (a) Pb, (b) Ba, (c) Ti, and (d) O.

High-energy E = 35 keV ($PbTiO_3$) and 30 keV ($BaTiO_3$) X-rays that can obtain more Bragg reflections and reduce the absorption effect were used for valence electron density analysis. The diffraction patterns were measured by the curved IP. In order to accurately determine the valence electron density distribution, thermal vibration parameters of each atom must be accurately determined. However, when IP is used, it is usually not possible to extend the measurement time beyond the saturation time determined by the strong diffraction peak on the low-angle side. Therefore, in this experiments, to avoid the high-intensity diffraction peaks on the low-angle side and measure the diffraction peaks on the high-angle side for a longer time, the measurements were performed with reference to the method devised by E. Nishibori *et al.* [32] [33] [34]. Fig. 1.2.5 shows a schematic view of the experimental setting. First, the diffraction data was measured for a long time as usual (Data-low). Next, by rotating the IP on the ω-axis to avoid diffraction peaks with high intensity, low-intensity diffraction peaks on the high-angle side were measured for a longer time (Dat-high). In this way, two data sets, Data-low and Data-high, were measured. The details of the experimental conditions are shown in Table 1.2.1.

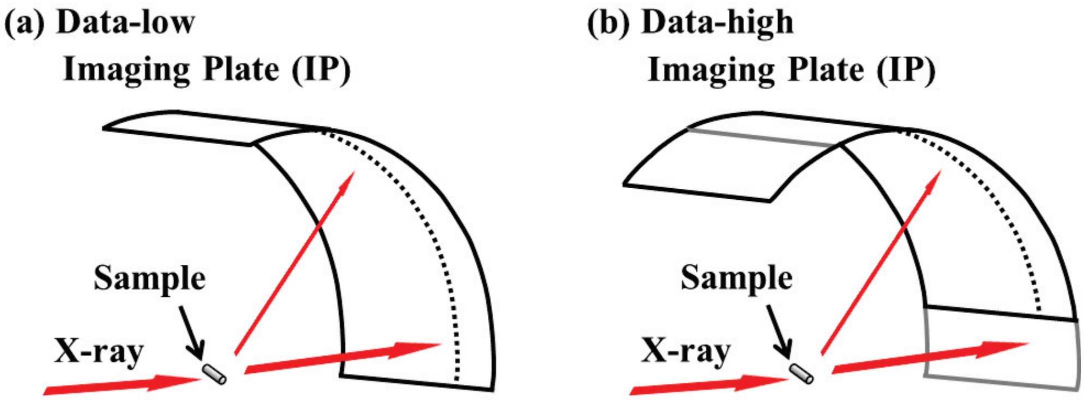

Fig. 1.2.5. Schematic view of the experimental setting.

Table 1.2.1. Experimental conditions of $PbTiO_3$ and $BaTiO_3$.

Material	Wavelength [Å]	Temp. [K]	Dataset name	Measurement time [min.]	Saturation time [min.]
$PbTiO_3$	0.35350(3)	91	Data-low	35	50
			Data-high	150	384
	0.35348(5)	850	Data-low	36.5	53
			Data-high	115.2	444
$BaTiO_3$	0.41279(7)	330	Data-low	35	49
			Data-high	280	408
		473	Data-low	27	41
			Data-high	168	196

Chapter 1.3: Analysis

Powder diffraction patterns measured by the synchrotron radiation X-ray diffraction experiments were analyzed by the maximum emtropy method (MEM)/Rietveld analysis [35] [36]. In this section, the principles and characteristics of the Rietveld analysis [37], MEM [38] and MEM/Rietveld analysis are described. A valence electron density analysis is also explained. The program used for the MEM/Rietveld method was provided by Prof. Makoto Sakata, Prof. Eiji Nishibori, and Prof. Masaki Takada. The program "sp6" [32] was used for the Rietveld analysis. The program "ENIGMA" [39] was used for the MEM analysis. The crtstall structures and 3-dimensional electron density distributions were visualized by the program "VESTA" [40].

§1.3.1. Rietveld analysis

The Rietveld analysis is a method devised by H. M. Rietveld in 1969 for an angular-dispersive neutron diffraction using a nuclear reactor [37]. Currently, the Rietveld analysis has been widely applied to an angle-dispersive X-ray diffraction using characteristic X-rays and synchrotron radiation, and a time-of flight neutron diffraction with a pulsed neutron source.

Various information is contained in the powder diffraction pattern. Lattice parameters are obtained from peak positions. Atomic positions, occupancies and temperature factors, so-called crystal structure parameters are derived from the integrated intensity of the diffraction profile. A lattice strain and crystallite size are obtained from the profile spread. A mass fraction can be estimated from the scale factor in the mixture. The Rietveld analysis is a general-purpose powder diffraction data analysis technology that can simultaneously obtain these important physical quantities.

In the Rietveld analysis, by fitting the diffraction pattern calculated based on the approximate structural model so that it matches the measured pattern as well as possible, the information contained in the whole diffraction pattern are elicited. When the diffraction intensities y_i ($i = 1, 2, 3 \ldots$) are measured at constant 2θ interval by the powder X-ray diffraction experiment, A set of variable parameters x that minimize the residual sum of squares $S(x)$ is refined by the nonlinear least squares method.

$$S(x)=\sum_i w_i[y_i-f_i(x)]^2 \tag{1.3.1}$$

Here, $f_i\ (x) \equiv f\ (2\theta_i\ ;\ x_1\ ,\ x_2\ ,\ x_3\ ,\ldots)$ and $w_i\ (=1\ /\ y_i)$ are the calculated intensity and statistical weight for i-th measurement point.

A reliability factor, R-factor is an indicator for evaluating the result of the Rietveld analysis. There are several R-factors. In this study, R_{wp}, R_I and R_F are used. The R_{wp}, R_I and R_F are defined as follows.

$$R_{\mathrm{wp}}=\left\{\sum_i w_i[y_i-f_i(x)]^2/\sum_i w_i{y_i}^2\right\}^{\frac{1}{2}} \tag{1.3.2}$$

$$R_I=\sum_H |I'_{\mathrm{obs}}(H)-I_{\mathrm{cal}}(H)|\,/\sum_H |I'_{\mathrm{obs}}(H)| \tag{1.3.3}$$

$$R_F=\sum_H \big||F'_{\mathrm{obs}}(H)|-|F_{\mathrm{cal}}(H)|\big|\,/\sum_H |F'_{\mathrm{obs}}(H)| \tag{1.3.4}$$

Here, $I'_{\mathrm{obs}}\ (H)$ and $I_{\mathrm{cal}}\ (H)$ are estimated observed and calculated values of the integrated intensity of the Bragg reflection, $F'_{\mathrm{obs}}\ (H)$ is an estimated observed value of the crystal structure factor, and H is the Miller index ($h\ k\ l$), respectively. R_{wp} is a weighted reliability factor for diffraction pattern fitting. R_I and R_F are reliability factors comparing calculated and observed values for the integrated intensity and the structure factor, respectively. The smaller the R-factors are, the more consistent the calculation intensities of the assumed structure model are, and the more reliable the analysis results are.

When fitting to each diffraction profile by the Rietveld analysis, it is necessary to set the half width W of the diffraction peaks to an appropriate value. In this study, the half-width function was defined by Eq. (1.3.5).

$$W=(u+v\times\tan\theta+w\times\tan^2\theta+p\times\sec^2\theta)^{\frac{1}{2}} \tag{1.3.5}$$

Here, u, v, w and p are the values input as parameters in the Rietveld analysis. In this analysis, only u, v and w were variables, and p was fixed to 0.

$PbTiO_3$ has plate-like crystallites due to cleavage. Therefore, it is necessary to consider the Miller index ($h\ k\ l$) dependence of the half width with respect to the diffraction intensity. Fig. 1.3.1 shows the definition of the angle φ that should be considered in the Rietveld analysis for a sample with plate-like crystallites. As shown in Fig. 1.3.1 (a), for a crystallite with a thin flat outer shape due to properties such as cleavage, the crystallite is thin in the direction parallel to $\boldsymbol{n}$ and thick in the direction perpendicular to $\boldsymbol{n}$. In the diffraction phenomenon, the crystallite size affects the half width of the diffraction peak. If the crystallite size is small, the diffraction peak becomes broad. For the crystallite shown in Fig. 1.3.1, the half width of the diffraction peaks whose scattering factor is close to the $\boldsymbol{n}$-direction is broad because the crystallite size in the $\boldsymbol{n}$-direction is small. Therefore, as shown in Fig. 1.3.1 (b), the peak profile fitting was performed by defining the angle φ. The direction of the normal vector $\boldsymbol{n}$ of the cleavage plane is $\varphi = 0°$, and the region of φ angle from 0° to 90° is divided into four parts, φ_i (i = 1, 2, 3, 4). The half width of the peak was devided into four corresponding to φ_i. In other words, the half width of the peak for $0° < \varphi < \varphi_1$ is represented by the same (u_1, v_1, w_1), and the half width is classified into four systems.

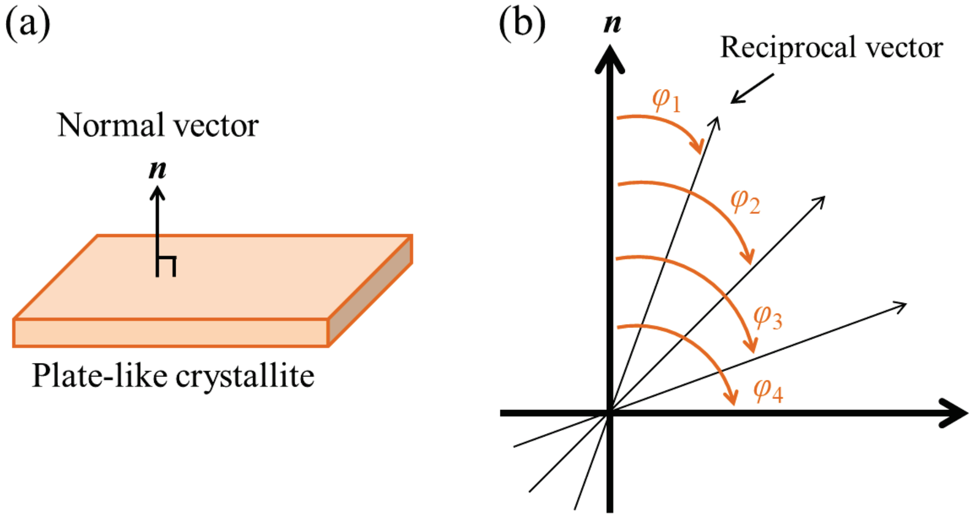

Fig. 1.3.1. Definition of the angle φ that should be considered in the Rietveld analysis for a sample with plate-like crystallites. (a) Normal vecter $\boldsymbol{n}$ of the plate-like crystallite. (b) Angle φ between the normal vector and the reciprocal lattice vector.

§1.3.2. Rietveld analysis considering the ionic state of atoms

The crystal structure factor is descrived as follows,

$$F(\boldsymbol{k}) = \sum_{j} f_j T_j \exp{(2\pi i \boldsymbol{k} \cdot \boldsymbol{r_j})} \tag{1.3.6}$$

Here, the T_j is a temperature factor $T(h\ k\ l)$ and represented by a Gaussian function with $\sin\theta / \lambda$ as a variable. The f_j is an atomic scattering factor and a damping function with $\sin\theta / \lambda$ as a variable, which can be approximated well by the Gaussian function. In order to estimate the thermal vibration parameter U_{ij} accurately, it is necessary to examine whether the model of the atmic scattering factor is a neutral atom or an ion. The difference in the values of the atomic scattering factors according to the model is remarkable in the low-angle region. Fig. 1.3.2 shows the diffraction angle dependence of the atomic scattering factors of Pb, Ti and O when using X-rays of 35 keV, and Ba, Ti and O when using X-rays of 30 keV. Here, ion species Pb, Pb^{2+}, Pb^{4+}, Ba, Ba^{2+}, Ti, Ti^{2+}, Ti^{4+}, O and O^{1-} described in the International Tables for Crystallography C [41] are plotted. Since the value of f at $2\theta = 0°$ is equal to the number of electrons in the atom, f in the low-angle range varies greatly depending on the ionic state of each atom. This affects the analysis of temperature factors related to the intensity decay rate. Each ion in the crystal is not stricyly in an ionic state of formal valence. Ions may have a valence that is not an integer, or a neutral state. Even for NaCl, which is consideres to be an ionic crystal, the degree of ionicity is said to be 0.94 [42]. Therefore, improper assumption of ionic valence and analysis of temperature factors may affect the result of separated F_{obs}, and lead to erroneous electron density distribution in the MEM analysis. It is required to perform the Rietveld analysis that does not depend on the assumed ionic states. When performing a precision electron density analysis, first, thermal vibration parameters were obtained by the Rietveld fitting using the diffraction data in the high angle range where the values of atomic scattering factors are equal regardless of the ionic state of atoms by excluding the low-angle data. After that, the Reitveld analysis was performed again using the entire range of the data without fitting the temperature factors.

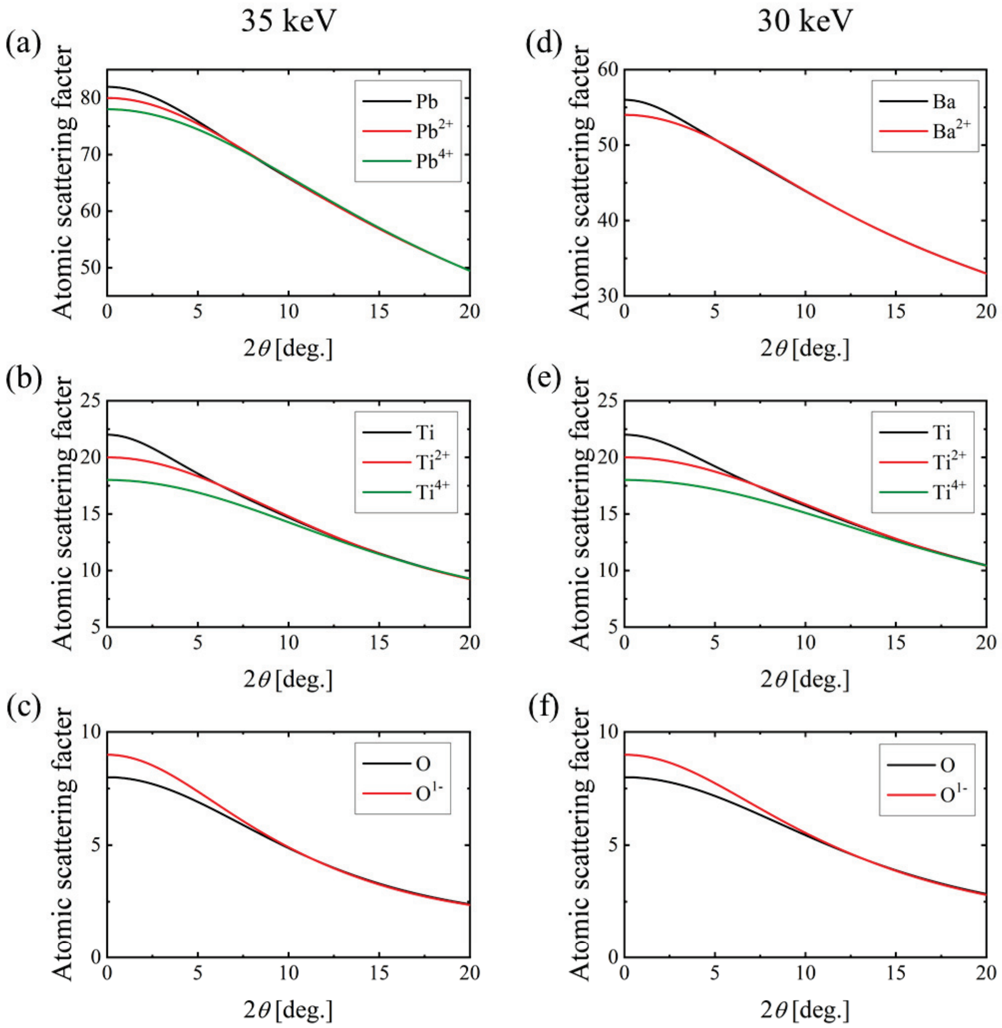

Fig. 1.3.2. Diffraction angle dependence of the scattering factor. (a) Pb, (b) Ti and (c) O when using X-rays of 35 keV. (d) Ba, (e) Ti and (f) O when using X-rays of 30 keV.

§1.3.3. Maximum Entropy Method (MEM)

Maximum Entropy Method (MEM) is a method to draw statistically most conclusive conclusions using information entropy (uncertainty of information to be processed) based on limited information. In 1976, the MEM was proposed by J. Burg as a method for underground exploration, and achived epoch-making success in various data processing in the field of geophysics. Since then, it has been spotlighted in the field of signal processing and has been applied to spectral analysis from a finite region of a signal. Nowadays, the MEM has been applied in various fields as a method for spectral analysis and image processing [43].

In MEM, a solution that maximizes information entropy is found under the constraint that it matches the information obtained by the experiment [38]. When MEM is used to determine the electron or nuclear densities, crystal structure factors are estimated so that the density distribution is dispersed as much as possible within the error range with respect to the observed structure factor. Non-zero crystal structures are estimated for the censored part of the high-angle region that cannot be measured. The main purpose of the electron density analysis is to observe outer electrons such as binding electrons and conduction electrons rather than inner electrons. These electrons are distributed spatially apart from the nucleus and make a large contribution to the diffraction intensities of low-angle reflection. When the single crystal method is used, an extinction effect becomes remarkable in the reflections in the low-angle region, but the correction is difficult. Since the extinction effect is negligible in the angle-dispersive powder diffraction method and the reflections hardly overlap in the low-angle region, the MEM analysis using powder diffraction data is suitable for visualization of chemical bonds [36] [44]. Fig. 1.3.3 shows the structure factors of Si obtained by the MEM electron density analysis and observed by the experiment [45]. The structure factors obtained by the MEM electron charge density analysis agree well with the observed structure factors, and a smooth curve was obtained even for the censored part of the high-angle region that cannot be measured.

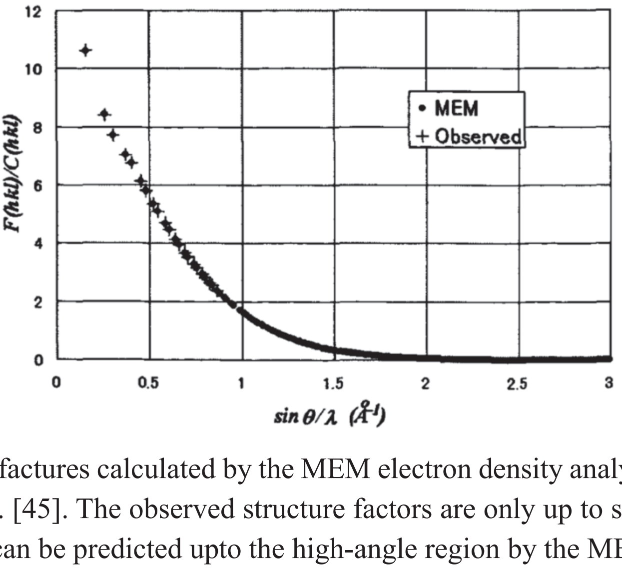

Fig. 1.3.3. Structure factures calculated by the MEM electron density analysis and observed by the experiment of Si. [45]. The observed structure factors are only up to $\sin\theta / \lambda = 0.8$ Å^{-1}, but the structurefactors can be predicted upto the high-angle region by the MEM analysis.

Here, the theory of MEM is descrived. In the case of X-rays, by considering the electron density distribution $\rho(xyz)$ in the unit cell as one scatter, the structure factor can be discrived by Eq. (1.3.7).

$$F(hkl) = V\int \rho(xyz)e^{-2\pi i(hx+ky+lz)}dxdydz \tag{1.3.7}$$

Hereafter let $r = (x, y, z)$ and $H = (h, k, l)$. The information entropy is expressed by Eq. (1.3.8).

$$S = -\sum_{r} \rho'(r)\ln\frac{\rho'(r)}{\rho'_0(r)} \tag{1.3.8}$$

Here, $\rho(r)$ and $\rho_0(r)$ are an actual electron chare density and standard electron density represented as follows.

$$\rho'(r) = \rho(r)/\int \rho(r)\,dr \tag{1.3.9}$$

$$\rho'_0(r) = \rho_0(r)/\int \rho_0(r)\,dr \tag{1.3.10}$$

The binding function C is expressed by Eq. (1.3.11).

$$C = \frac{1}{N}\sum\frac{|F_{\mathrm{obs}}(H) - F_{\mathrm{cal}}(H)|^2}{\sigma_H^2} \tag{1.3.11}$$

Here, $F_{\mathrm{obs}}(H)$ is the crystal structure factor obtained by the experiment, N is the number of $F_{\mathrm{obs}}(H)$, and σ_H is the standard deviation with respect to $F_{\mathrm{obs}}(H)$, respectively. $F_{\mathrm{cal}}(H)$ is expressed as follows.

$$F_{\mathrm{cal}}(H) = V\int \rho(r)\exp\,(-2\pi i r\cdot H)dr \tag{1.3.12}$$

From the theory of error, C is expected to be 1. From Eqs. (1.3.7) and (1.3.10), the following equation is obtained as the bound entropy $Q(\lambda)$.

$$Q(\lambda) = -\sum_{r} \rho'(r)\ln\frac{\rho'(r)}{\rho'_0(r)} - \frac{\lambda}{2}(C-1) \tag{1.3.13}$$

Here, λ is the Lagrange multiplier. Eq. (1.3.14) is finally obtained by using the condition for maximizing Eq. (1.3.12), $\partial Q(\lambda)/\partial\rho(r) = 0$, and some approximations.

$$\rho(r) = \exp\left[\begin{array}{c}\ln\rho_0(r) + \frac{\lambda F_0}{N}\sum\frac{1}{\sigma_H^2}\{F_{\mathrm{obs}}(H) - F_{\mathrm{cal}}(H)\} \\ \times\exp\,(-2\pi i r\cdot H)\end{array}\right] \tag{1.3.14}$$

Here, F_0 is the number of total electrons in the unit cell. By approximating $F_{\mathrm{cal}}(H)$ as the Fourier transformation of $\rho_0(r)$ as Eq. (1.3.15), the right side of Eq. (1.3.13) is a function that depends on only $\rho_0(r)$.

$$F_{\mathrm{cal}}(H) = V \int \rho_0(r) \exp(-2\pi i r \cdot H)\, dr \tag{1.3.15}$$

In the actual calculations, a uniform electron density distribution is given as an initial value of $\rho_0(r)$. The electron density distribution is obtained by repeating the calculation by inserting the obtained $\rho(r)$ into $\rho_0(r)$ until C becomes 1 or less. The electron density distribution obtained by this method does not depend on the initial value $\rho_0(r)$, and only the accuracy of $F_{\mathrm{obs}}(H)$ is important.

Figure 1.3.4 shows the electron density distributions of the Si (110) plane obtained by the Fourier synthesis method and MEM [38]. Both electron density distributions are obtained using same measured structure factors $F(Q)$ included in the range of $d > 0.58$ Å ($Q < 0.86$ Å^{-1}). It is said that the Fourier synthesis method can accurately derive the electron density distribution at the atomic position. However, to derive the electron density distribution in the real space by the Fourier synthesis method, the structure factor of the whole reciprocal space (Q-space) must be used in principle. When only limited structure factors with a narrow reciprocal space are obtained by the experiment, an unnatural distribution such as a negative electron density distribution appears due to a truncation effect. In such case, it is difficult to get information about a distribution with low density such as bonding electrons. On the other hand, in the electon density distribution obtained by MEM, the existence of covalent bonds between Si atoms can be clearly confirmed as compared with the Fourier synthesis method. This is because the truncation effect is reduced by estimating high-Q structure factors that have not been measured in the calculation of MEM. When discussing bonding electrons, the MEM method that can derive the noise-less electron density distribution from a finite number of structure factors is effective.

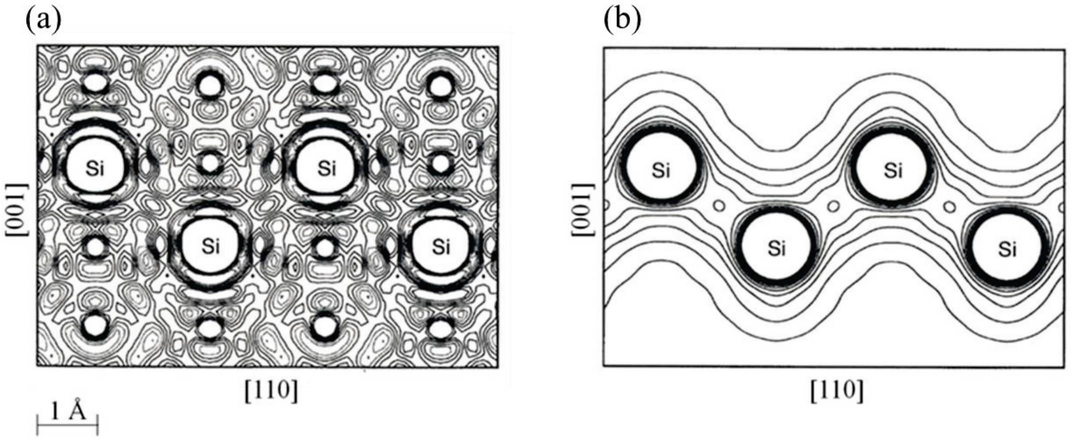

Fig. 1.3.4. Difference in electron density distribution of (1 1 0) plane of Si due to difference in analysis method [38]. (a) Fourier synthesis (contour map: -3.0 ~ 3.0 e Å^{-3}, 0.3e Å^{-3} step). (b) MEM electron density analysis (contour map: 0.1 ~ 2.0e Å^{-3}, 0.1e Å^{-3} step). The electron density distribution was analyzed using structural factors in the same range (d > 0.58 Å) measured by the X-ray diffraction experiment.

To derive the electron density distribution, it is required to pay attention to what information $F_{\mathrm{obs}}(Q)$ mainly contains depending on the range of Q. Fig. 1.3.5 shows a comparison between the measured structure factors F_{obs} used to derive the electron density distribution in Fig. 1.3.4 [38] and the calculated structure factors F_{sim} simulated by assuming that Si is Si^{+4} ion [46]. There is almost no difference between the F_{obs} and F_{sim} in the range where the diffraction index is large, while the difference is large in the range where the index is small. This means that the information about outer shell electrons and bonding electrons is included in the small Q range of F. Careful attention to the estimation of F in low-Q range is required to discuss covalent properties.

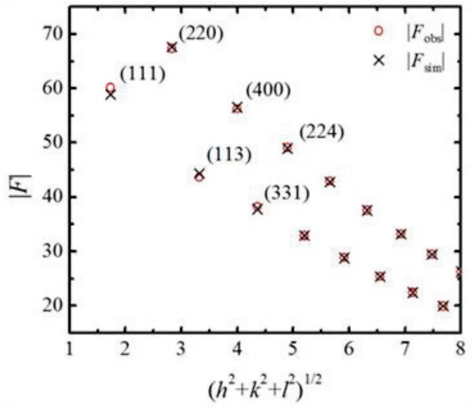

Fig. 1.3.5. Comparison between measured structure factors F_{obs} and calculated structure factors F_{cal} in ion model of Si. [46]. F_{cal} were calculated by assuming that Si is Si^{4+}. F_{obs} and F_{cal} have a slight difference in low-angle diffraction.

On the other hand, as already mentioned above, the high-Q data is involved in the truncation of the Fourier trandform. Q has the following relationship with d in the Bragg's equation (1.3.16).

$$2d\sin\theta = \lambda \tag{1.3.16}$$

$$Q = 4\pi\sin\theta/\lambda = 2\pi/d \tag{1.3.17}$$

Using high-Q data means that we can observe the spatial distribution of electron density in the crystal with the small d, that is, in detail. In this sense, the minimum d is used as a measure of spatial resolution. In the MEM analysis, an unmeasured high-Q F is estimated, but an error may occur in this estimation. Using the measured high-Q data is also effective in preventing this estimation error. However, in the case of X-ray diffraction, since the atomic scattering factor and temperature factor act to reduce the intensity sharply as Q becomes higher, high-Q data has low statistical accuracy and may lead to inaccurate results. Therefore, to analyze the MEM electron density distribution, it is required to measure F_{obs} with high statistical accuracy in a wide Q range from low-Q to high-Q.

§1.3.4. Consideration of weight for the MEM electron density analysis

The MEM electron density analysis is a powerful technique for visualizing the chemical bonding state between atoms. In ordinary Rietveld analysis, deviations that do not consider the intensity distribution are obtained when deriving the standard deviations of the structure factors. As a result, physically meaningless noise may occur in the electron density distribution derived by MEM. This is because the MEM analysis selects "the solution with the maximum information entropy" from the given information. Researches have been conducted to understand this tendency and visualize electron density distributions with higher accuracy [47] [48]. R. Y. De Vries *et al.* simulated the diffraction experiment by considering a virtial crystal structure with H_2O as a constituent molecule and investigated to which angle range the electron density distribution derived by the MEM analysis is dragged with respect to the diffraction data [49]. Fig 1.3.6 (a) shows the crystal structure of H_2O (space group $P2/m$) that was considered as a model. Since the actual H_2O crystal has a three-dimensional hydrogen bond network as typified by ice Ih (space group $P6_3/mmc$), this crystal structure is a virtual crystal devided only for the MEM study. They calculated the structure factors F_{MEM} based on this structure. F_{obs} was created by adding a random error to F_{MEM}. The error is devised to follow a Gaussian distribution. The electron density analysis in which the actual structure factors F_{obs} and the structure factosr F_{MEM} estimated by MEM are matched within the range of the standard deviation σ_{obs} of F_{obs}. Unlike ordinary structure analysis, σ_{obs} is also used as analysis data. The standardized residuals ΔF is defined by Eq. (1.3.18).

$$\Delta F = \frac{|F_{\mathrm{obs}}| - |F_{\mathrm{MEM}}|}{\sigma_{\mathrm{obs}}} \tag{1.3.18}$$

If F_{MEM} is correctly estimated, ΔF is caused only by the random error of F_{obs}, so a histogram with ΔF on the horizontal axis and frequency on the vertical axis should have a Gaussinan distribution with a half width of 1. Fig. 1.3.6 (b) shows the MEM electron density distribution analyzed using 1752 independent structure factors F_{obs} in the range of $d > 0.36$ Å. Fig. 1.3.6 (c) shows the histogram of ΔF expressed by Eq. (1.3.18) together with the ideal Gaussian distribution. The electron density distribution is noisy and seems to be far from the model in Fig. 1.3.6 (a). The histogram is quite different from the Gaussian distribution. For low-order indices of large diffraction intensity, data also exist in the range where $|\Delta F| > 5$. On the contrary, the central part of the distribution contains many high-order indices of small diffraction intensity. The reason for such a distribution is due to the principle of MEM and is because the MEM analysis selects "the solution eith the maximum information entropy S" from the given information. In X-ray diffraction experiments, the higher the order of the diffraction index, the more rapidly the intensity decreases. Therefore, the number of data with low diffraction intensity is generally much larger that the number of data with high diffraction intensity. Since the entropy S of MEM is larger as the diffraction intensity is smaller, these are overweighted, which leads to the analysis results drawn to the higher-order diffraction data. As a result, on the contrary, in the case of low-order diffraction data, the weight in the analysis becomes too small and $|\Delta F|$ becomes large. The electron density distribution induced by such inappropriate weights (Fig. 1.3.6 (b)) does not reproduce the original crystal structure model (Fig. 1.3.6 (a)).

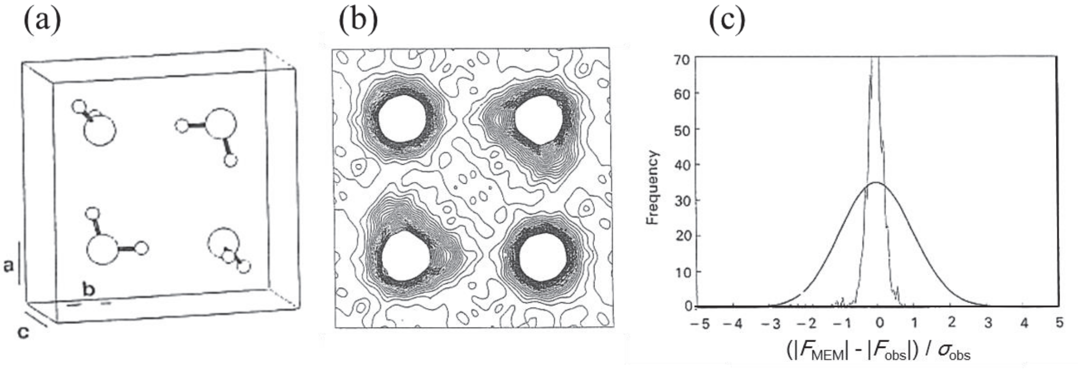

Fig. 1.3.6. (a) Crystal structure of H_2O. (b) MEM electron density distribution of H_2O. (c) Histgram of standardized residuals [49]. Results of the MEM analysis using 1752 noisy structure factor data sets. Histgram spacing of standardized residuals is 0.05. The solid line shows the ideal Gaussian distribution. The histgram has a sharp distribution, and there are values outside the drawing range of the graph.

R. Y. De Vries *et al.* suggested to add weights based on the power of reciprocal lattice vector $|H|^{-n}$ in the MEM analysis as a method to reduce such inappropriate weights [49]. This method means that the analysis is performed by weighting the low-order diffraction intensities with small H. Fig. 1.3.7 shows (a) the electron density distribution of H_2O re-analyzed using the weight of $|H|^{-4}$ and (b) the histogram of the standardized residuals ΔF. The noise of the electron density distribution is greatly reduced. In addition to the strong covalent bond between O and H, the hydrogen bond is clearly visualized. The histogram of ΔF approaches the ideal Gaussian distribution, and all diffraction peaks are within the range of $|\Delta F| < 5$.

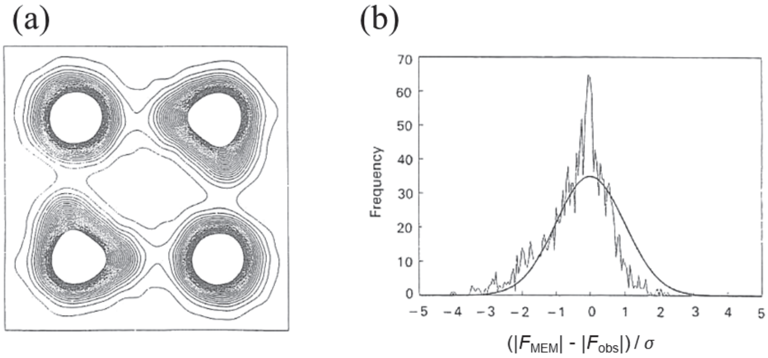

Fig. 1.3.7. MEM analysis results using weighting. (a) MEM electron density distribution. (b) Histgram of standardized residuals [49]. Histgram spacing of standardized residuals is 0.05. The solid line shows the ideal Gaussian distribution. The histogram approached the shape of the ideal Gauusian distribution.

As a method to reduce improper weighting, it is effective to add weights based on the power of the reciprocal lattice vecter $|H|^{-2n}$ in the MEM analysis. However, this method tends to reduce the standardized residual in the angular range where Hj is large and the intensity is small. In this study, to mitigate this tendency, C_w which is the binding function multiplied by the weight function w_j was used.

$$C_w = \frac{1}{N_F}\sum_{j}^{N_F} w_j \left|\frac{F_{\mathrm{obs}}(H_j) - F_{\mathrm{MEM}}(H_j)}{\sigma_{\mathrm{obs}}(H_j)}\right|^2 \tag{1.3.19}$$

The weight function is based on the power of the magnitude of the reciprocal lattice vector.

$$w_j = \frac{1}{|H_j|^{2n}}\left(\frac{1}{N_F}\sum_{i}^{N_F}\frac{1}{|H_i|^{2n}}\right) \tag{1.3.20}$$

When using this weight in the analysis, The MEM analysis was performed by changing $\sigma_{\mathrm{obs}}(H_j)$ which is the standard deviation of $F_{\mathrm{obs}}(H_j)$ to a new $\sigma'(H_j)$ by multiplying the weight without changing the conventional MEM analysis program ENIGMA. The expression of $\sigma'(H_j)$ is as follows.

$$\sigma'(H_j) = {w_j}^{-\frac{1}{2}}\sigma_{\mathrm{obs}}(H_j) = |H_j|^n \left(\frac{1}{N_F}\sum_{i}^{N_F}\frac{1}{|H_i|^{2n}}\right)^{-\frac{1}{2}} \sigma_{\mathrm{obs}}(H_j) \qquad (1.3.21)$$

§1.3.5. MEM/Rietveld analysis

Taking advantage of the features of the Rietveld method and MEM descrived above, the electron charge density distribution is obtained from the X-ray powder diffraction pattern by a well-combined MEM/Rietveld analysis. Here, the MEM/Rietveld method is discrived [35] [50].

In powder diffraction experiments, since all Bragg reflections are projected on the 2θ axis, the reflections overlap each other. Therefore, to obtain the electron density distribution from the powder diffraction pattern, the following process must be taken.

(1) To separate multiple overlapping Bragg reflections (profile separation) and extract the integrated intensity of each refrection.

(2) To obtain the absolute value of the crystal structure factors by making various corrections to the obtained integrated intensity.

(3) To build a crystal structure model and determine the phase of the crystal structure factors based on the model.

(4) To perform the MEM analysis using the obtained crystal structure factors.

The processes (1) to (3) are performed by the Rietveld analysis. In the process (1), the following profile separation is performed by using the structure model that best matches the powder diffraction pattern obtained by the Rietveld analysis. Let Y_{o} be the measured intensity and Y_{c} be the calculated intensity at a certain Bragg angle 2θ. Where Y_{c} is the sum of the calculated intensities of M peaks ($Y_{\mathrm{c}1} + Y_{\mathrm{c}2} + \ldots + Y_{\mathrm{c}M}$). Based on this calculated intensity, Y_{o} is proportionally distributed to M observed intensities ($Y_{\mathrm{o}1}$, $Y_{\mathrm{o}2}$, …, $Y_{\mathrm{o}l}$, …, $Y_{\mathrm{o}M}$) from Eq. (1.3.22).

$$Y_{\mathrm{o}l}(2\theta) = Y_{\mathrm{o}}(2\theta) \times \frac{Y_{cl}}{\sum_{m=1}^{M} Y_{cm}(2\theta)} \qquad (1.3.22)$$

Various corrections required for the process (2) are included in the Rietveld analysis as parameters when calculating the diffraction pattern from the crystal structure model. The process (3) is performed using the refined crystal structure model. The electron density analysis is performed by MEM using the crystal structure factors obtained by the processes (1) to (3) of the Rietveld analysis [36]. If the obtained electron density distribution contradicts the crystal structure model, improve the crystal structure model so that it matches the electron density distribution, and perform the Rietveld analysis again. By repeating such a cycle, finally the crystal structure model and electron density distribution that best match the measured data are obtained. Fig. 1.3.8 shows the flowchart of the MEM/Rietveld method [50].

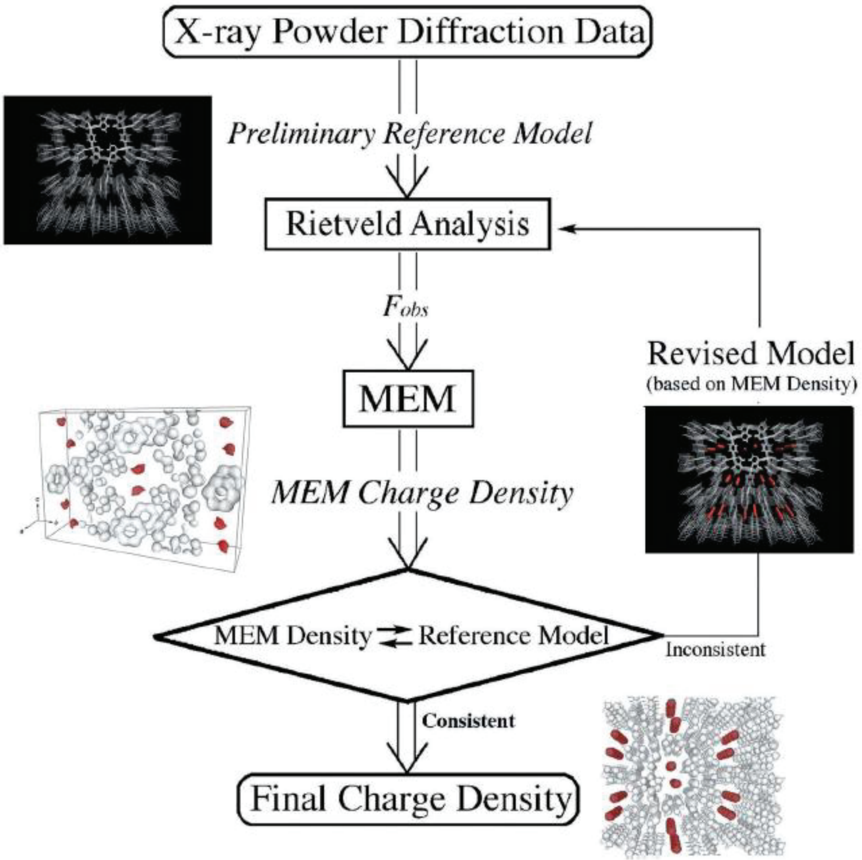

Fig. 1.3.8. Flowchart of MEM/Rietveld method [50].

§1.3.6. Core/multishell analysis for $BaTiO_3$

$BaTiO_3$ is known to have a composite structure composed of an inner tetragonal core, a gradient lattice strain layer (GLSL) and a surface cubic layer [51] [52]. Fig. 1.3.9 shows the model of the composite structure of BT proposed by T. Hoshina *et al*. [51]. The center of the particle (core) has a tetragonal structure, and the surface of the particle (shell) has a cubic structure. The GLSL exists between the core and shell to relax the lattice mismatch. The tetragonal distortion of the GLSL increases as it approaches the core from the shell. The core/multi-shell model [53] is used to analyze the composite structure. Fig. 1.3.10 shows the core/multi-shell model. In this study, the Rietveld analysis was performed using three phases of tetragonal BT (T0, T1, and T2) and one phase of cubic BT (C) by assuming the GSLS as two phases of tetragonal BT (T1 and T2) with different tetragonal strains.

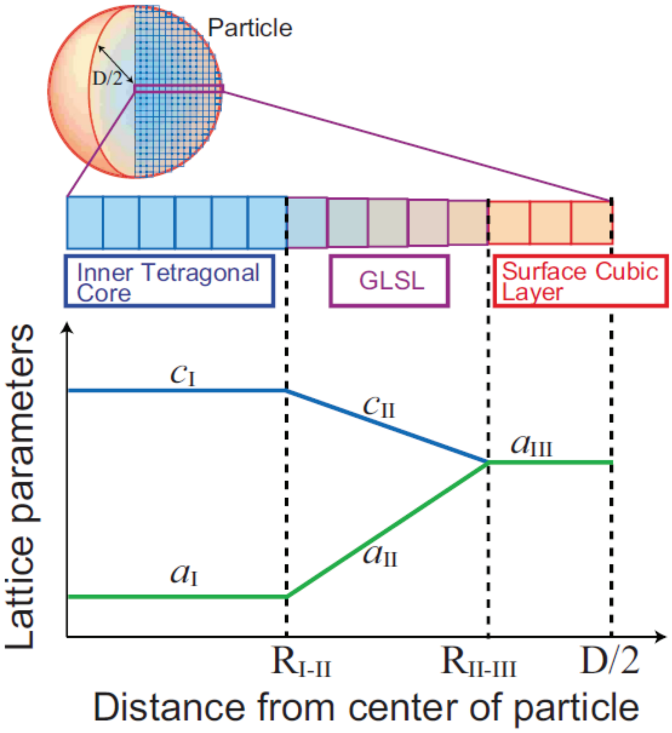

Fig. 1.3.9. Model of composite structure of $BaTiO_3$ particles [51].

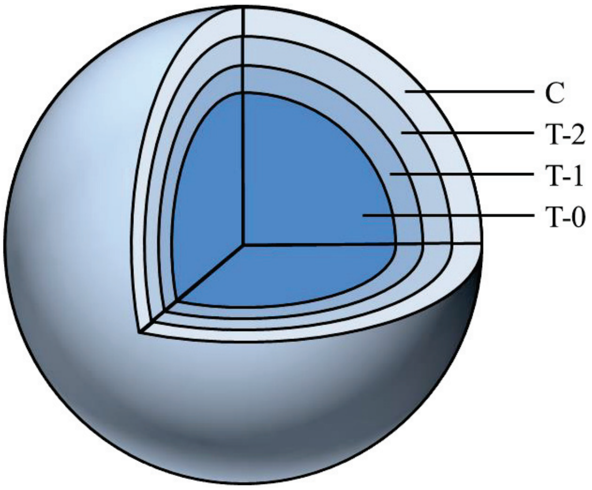

Fig. 1.3.10. Core/multi-shell model of $BaTiO_3$ particles.

§1.3.7. Valence electron density analysis

In this study, a method to visualize the electron density distribution of valence electrons have been developed. Each atom in the crystal has an anisotropic and distorted electron density distribution due to interactions and orbital hybridizations. Such an effect on the inner-core electrons is small, and their density distirbution is thought to be similar to that of isolated atoms. The valence electron density distribution which reflects the bonding state of the atoms in the crystal is derived by calculating the core electron density distribution and subtracting it from the total electron density distribution determined by the SXRD experiments. The relationship between the total electron density distribution $\rho_{\mathrm{obs}}^{\mathrm{total}}$ obtained experimentally, the calculated core electron density distribution $\rho_{\mathrm{cal}}^{\mathrm{core}}$, and the valence electron density distribution ρ^{valence} is given by Eq. (1.3.23).

$$\rho^{\mathrm{valence}} = \rho_{\mathrm{obs}}^{\mathrm{total}} - \rho_{\mathrm{cal}}^{\mathrm{core}} \tag{1.3.23}$$

When obtaining the valence electron density distribution ρ^{valence}, instead of taking the difference between $\rho_{\mathrm{obs}}^{\mathrm{total}}$ and $\rho_{\mathrm{cal}}^{\mathrm{core}}$ directly in the real space, the same idea as the difference Fourier synthesis method is applied and the difference of the structure factor F which is a quantity in the reciprocal space is taken. The structure factors $F_{\mathrm{obs}}^{\mathrm{total}}$, $F_{\mathrm{cal}}^{\mathrm{core}}$ and F^{valence} which are the Fourier transformation of $\rho_{\mathrm{obs}}^{\mathrm{total}}$, $\rho_{\mathrm{cal}}^{\mathrm{core}}$ and ρ^{valence} have the following relationship.

$$F^{\mathrm{valence}} = F_{\mathrm{obs}}^{\mathrm{total}} - F_{\mathrm{cal}}^{\mathrm{core}} \tag{1.3.24}$$

$F^{\mathrm{valence}}(hkl)$ of $PbTiO_3$ and $BaTiO_3$ were estimated as follows. First, the scattering factors of the core electrons of Pb, Ba, Ti, and O atom were calculated by first-principles calculations using the relativistic Dirac-Fock calculation program [54] [55]. Table 1.3.1 shows the assumed electron configrations of Pb, Ba, Ti, and O atoms. Next, the scattering factors of core electrons and crystal structure parameters obtained from the Rietveld analysis were used to calculate $F_{\mathrm{cal}}^{\mathrm{core}}(hkl)$. Finally, $F^{\mathrm{valence}}(hkl)$ of PT and BT were obtained by subtracting $F_{\mathrm{cal}}^{\mathrm{core}}(hkl)$ from $F_{\mathrm{obs}}^{\mathrm{total}}(hkl)$ as shown in Eq. (1.3.24). The valence electron density distributions of PT and BT were determined by MEM analysis using the dataset of $F^{\mathrm{valence}}(hkl)$. Such a process is similar to the process of the core differential Fourier synthesis (CDFS) method proposed by S. Kitou *et al.* [56] [57]. The Fourier synthesis is used in the CDFS method, while in this study, MEM is used instead of the Fourier synthesis to analyze the electron density distribution accurately without truncation errors in the Fourier transform from a limited number of experimentally obtained structure factors.

Table 1.3.1. Assumed electron configrations of Pb, Ba, Ti, and O atoms for valence electron density analysis.

Total	Core	Valence
[Pb]	[Xe] $4f^{14}5d^{10}$	$6s^2 6p^2$ ($4e^-$)
[Ba]	[Xe]	$6s^2$ ($2e^-$)
[Ti]	[Ar]	$3d^2 4s^2$ ($4e^-$)
[O]	[He] $2s^2$	$2p^4$ ($4e^-$)

Chapter 1.4: Results and discussion

§1.4.1. Visualization of valence electron density distributions of $PbTiO_3$ and $BaTiO_3$

First, the total electron density distributions are determined by the MEM/Rietveld method. Figure 1.4.1 shows diffraction patterns of $PbTiO_3$ at (a) 91 K (ferroelectric phase) and (b) 850 K (paraelectric phase) and Fig. 1.4.2 shows diffraction patterns of BT at (a) 330 K (ferroelectric phase) and (b) 473 K (paraelectric phase). The brighter whites indicate higher diffraction intensities. The upper figure is Data-low and the lower one is Data-high. The intensities of the diffraction image were integrated with a width of 2.5 mm (51 pixel) with respect to the diffraction angle 2θ to create one-dimensional (1D) diffraction data.

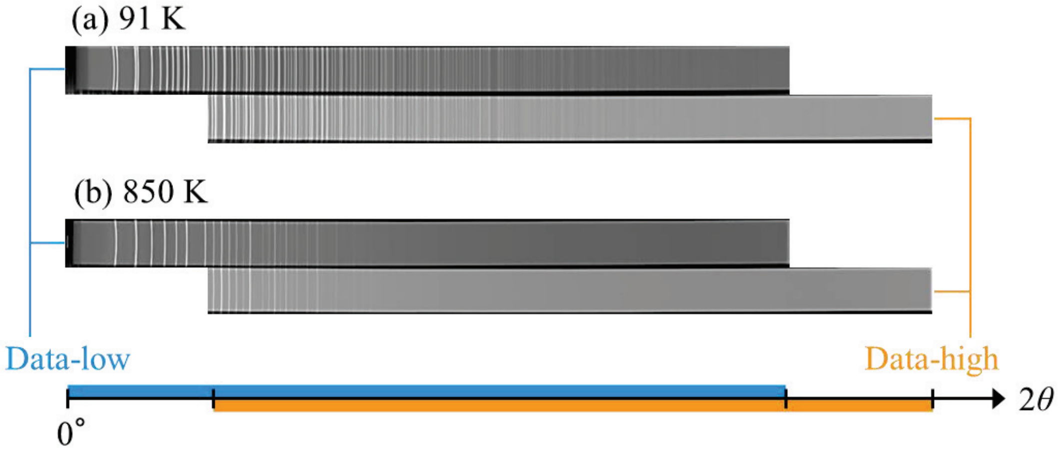

Fig. 1.4.1. Diffraction patterns of $PbTiO_3$ at (a) 91 K (ferroelectric phase) and (b) 850 K (paraelectric phase) recorded on the curved imaging plate.

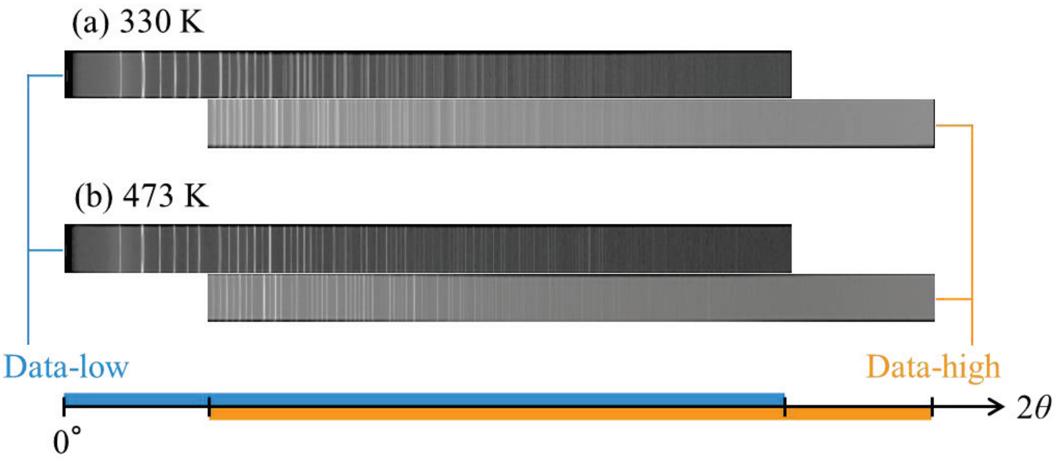

Fig. 1.4.2. Diffraction patterns of $BaTiO_3$ at (a) 330 K (ferroelectric phase) and (b) 473 K (paraelectric phase) recorded on the curved imaging plate.

Figure 1.4.3 shows Rietveld profile fitting results of PT at (a) 91 K and (b) 850 K. The upper figure is Data-low and the lower one is Data-high. The final structure models are based on the application of a neutral atom model to the atomic scattering factors and an anisotropic model to the thermal vibration parameters of each atom. The coordinates and thermal vibration parameters of each atom were analyzed using data in the angular range of $15° \leq 2\theta$, where the atomic scattering factor is independent of ionic valence, since it is not obvious what individual atoms are ionized in the crystal as discrived in §1.3.2. The reliability factors are $R_{\mathrm{wp}} = 2.29\%$, $R_{\mathrm{I}} = 1.41\%$ and $R_{\mathrm{F}} = 0.96\%$ for 91 K, and $R_{\mathrm{wp}} = 1.76\%$, $R_{\mathrm{I}} = 2.41\%$ and $R_{\mathrm{F}} = 2.40\%$ for 850 K, respectively. Table 1.4.1 and Fig.1.4.4 shows the determined crystal structure parameters and ORTEP models of PT at (a) 91 K and (b) 850 K. In Fig. 1.4.4, the size of the ellipse represents the magnitude of the thermal vibration parameters. In the tetragonal phase, the direction of the spontaneous atomic displacement of the Ti and O ions is the same. The tetragonality c/a is about 1.072.

(a) 91 K

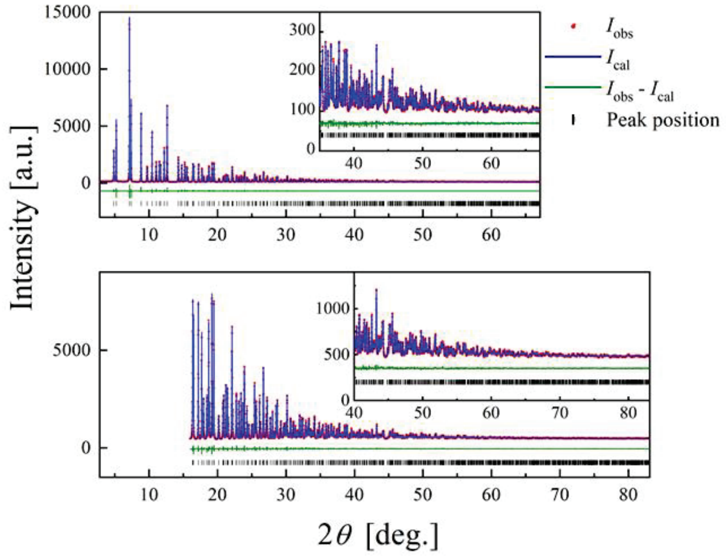

(b) 850 K

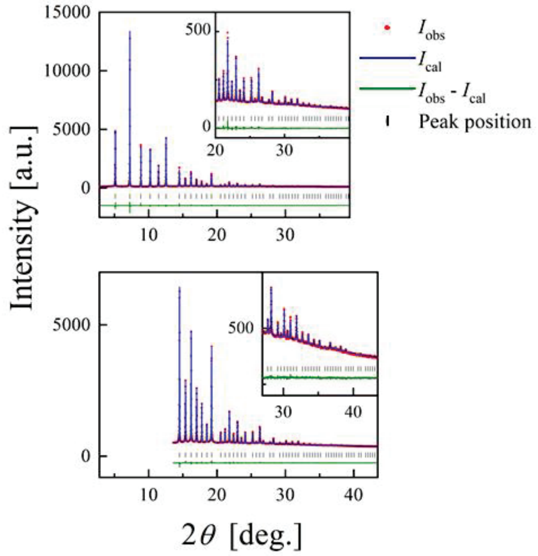

Fig. 1.4.3. Rietveld profile fitting results of $PbTiO_3$ at (a) 91 K (ferroelectric phase, space group: *P*4*mm*) and (b) 850 K (paraelectric phase, space group: $Pm\overline{3}m$). The red dot, blue line, green line, and | represent the observed intensity, calculated intensity, residual from I_{obs} minus I_{cal}, and peak position, respectively. The analysis range is (a) $d > 0.27$ Å ($2\theta < 83.1°$) and (b) $d > 0.48$ Å ($2\theta < 43.5°$). The reliability factors are (a) $R_{wp} = 2.29\%$, $R_I = 1.41\%$ and $R_F = 0.96\%$, and (b) $R_{wp} = 1.76\%$, $R_I = 2.41\%$ and $R_F = 2.40\%$, respectively.

Table 1.4.1. Crystal structure parameters of $PbTiO_3$.

(a) 91 K (ferroelectric phase, space group: $P4mm$). Lattice parameters: $a = b = 3.89046(2)$ Å, $c = 4.17144(2)$ Å, and $\alpha = \beta = \gamma = 90°$ for data with $d > 0.27$ Å.

Atom	x	y	z	U_{11} [10^{-2}Å^2]	U_{22} [10^{-2}Å^2]	U_{33} [10^{-2}Å^2]
Pb	0	0	0	0.258(3)	$= U_{11}$	0.284(2)
Ti	0.5	0.5	0.5417(1)	0.20(1)	$= U_{11}$	0.35(2)
O1	0.5	0.5	0.1198(5)	0.51(7)	$= U_{11}$	0.46(7)
O2	0.5	0	0.6238(3)	0.21(4)	0.32(4)	0.33(5)

(b) 850 K (paraelectric phase, space group: $Pm\bar{3}m$). Lattice parameters: $a = b = c = 3.97292(2)$ Å and $\alpha = \beta = \gamma = 90°$ for data with $d > 0.48$ Å.

Atom	x	y	z	U_{11} [10^{-2}Å^2]	U_{22} [10^{-2}Å^2]	U_{33} [10^{-2}Å^2]
Pb	0	0	0	3.82(2)	$= U_{11}$	$= U_{11}$
Ti	0.5	0.5	0.5	1.75(2)	$= U_{11}$	$= U_{11}$
O	0.5	0.5	0	3.18(9)	$= U_{11}$	1.25(6)

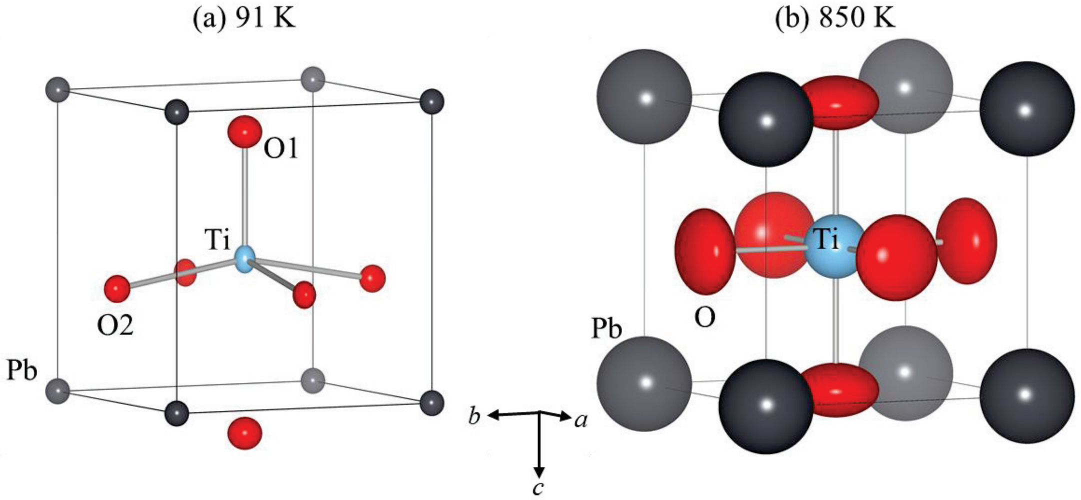

Fig. 1.4.4. ORTEP models of $PbTiO_3$ at (a) 91 K (ferroelectric phase, space group: $P4mm$) and (b) 850 K (paraelectric phase, space group: $Pm\bar{3}m$). The size of the ellipse represents the magnitude of the thermal vibration parameters.

Figure 1.4.5 shows the Rietveld profile fitting results of BT at (a) 330 K and (b) 473 K. The upper figure is Data-low and the lower one is Data-high. The final structure models are based on the application of a neutral atom model to the atomic scattering factors and an anisotropic model to the thermal vibration parameters of each atom. The coordinates and thermal vibration parameters of each atom were analyzed using data in the angular range of $17.5° \leq 2\theta$, where the atomic scattering factor is independent of ionic valence. In the Rietveld analysis, the core/multishell model which consists of three tetragonal phases (T0, T1 and T2) and one cubic phase (C) was used for the data at 330 K (ferroelectric phase). For T1, T2, and C phases (Shell), the atomic coordinates and thermal vibration parameters were fixed. The reliability factors are R_{wp} = 2.43 %, R_{I} = 1.46% and R_{F} = 1.21% for 330 K, and R_{wp} = 2.67%, R_{I} = 1.25% and R_{F} = 1.20% for 473 K, respectively. Table 1.4.2 and Fig. 1.4.6 show the crystal structure parameters and ORTEP models of BT at (a) 330 K and (b) 473 K, respectively. The thickness of each layer was estimated to be about 235.4 nm, 12.8 nm, and 1.9 nm for the inner tetragonal core (T0), GLSL (T1 and T2), and surface cubic layer (C), respectively. The crystal structure parameters of the inner tetragonal core were used as a result at 330 K. In the tetragonal phase, the direction of the spontaneous atomic displacement of the Ti and O ions is the opposite. The tetragonality *c*/*a* is about 1.010.

(a) 330 K

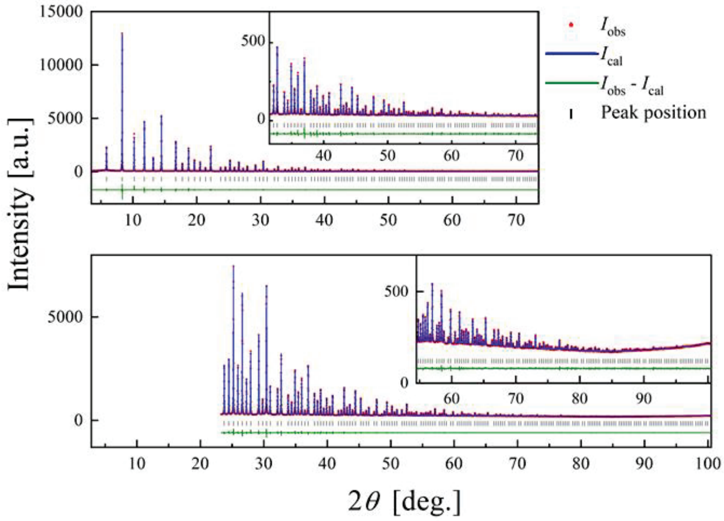

(b) 473 K

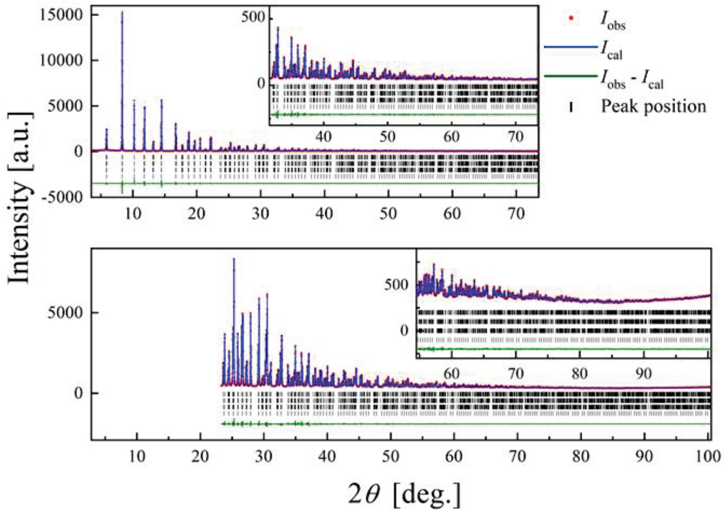

Fig. 1.4.5. Rietveld profile fitting results of $BaTiO_3$ at (a) 330 K (ferroelectric phase, space group: $P4mm$) and (b) 473 K (paraelectric phase, space group: $Pm\overline{3}m$). The red dot, blue line, green line, and | represent the observed intensity, calculated intensity, residual from I_{obs} minus I_{cal}, and peak position, respectively. The analysis range is d > 0.27 Å (2θ < 100.5°). The reliability factors are (a) R_{wp} = 2.43%, R_I = 1.46% and R_F = 1.21%, and (b) R_{wp} = 2.67%, R_I = 1.25% and R_F = 1.20%, respectively.

Table 1.4.2 Crystal structure parameters of $BaTiO_3$ for data with $d > 0.27$ Å.

(a) 330 K (ferroelectric phase, space group: *P*4*mm*). The core/multishell model is used. *x* and *y* coordinates are the same in each phase.

Lattice parameters	T0	T1	T2	C
a [Å]	3.99737(1)	3.99862(5)	4.0032(1)	4.0151(2)
c [Å]	4.03701(1)	4.03110(7)	4.0284(2)	= *a*

Atom	*x*	*y*	*z* (T0)	*z* (T1)	*z* (T2)	*z* (C)
Ba	0	0	0	0	0	0
Ti	0.5	0.5	0.5120(2)	0.511	0.511	0.5
O1	0.5	0.5	-0.0248(3)	-0.019	-0.017	0
O2	0.5	0	0.4829(3)	0.490	0.492	0

Atom	U_{11} (T0) [10^{-2}Å^2]	U_{22} (T0) [10^{-2}Å^2]	U_{33} (T0) [10^{-2}Å^2]	U_{iso} (Shell) [10^{-2}Å^2]
Ba	0.510(3)	$= U_{11}$	0.540(3)	0.55
Ti	0.724(7)	$= U_{11}$	0.66(3)	0.55
O1	0.80(4)	$= U_{11}$	0.4(1)	0.71
O2	0.67(2)	0.59(2)	0.7(1)	0.71

(b) 473 K (paraelectric phase, space group: $Pm\bar{3}m$). Lattice parameters: $a = b = c = 3.97292(2)$ Å and $\alpha = \beta = \gamma = 90°$.

Atom	*x*	*y*	*z*	U_{11} [10^{-2} Å^2]	U_{22} [10^{-2} Å^2]	U_{33} [10^{-2} Å^2]
Ba	0	0	0	0.813(4)	$= U_{11}$	$= U_{11}$
Ti	0.5	0.5	0.5	1.061(7)	$= U_{11}$	$= U_{11}$
O	0.5	0.5	0	1.07(2)	$= U_{11}$	0.95(1)

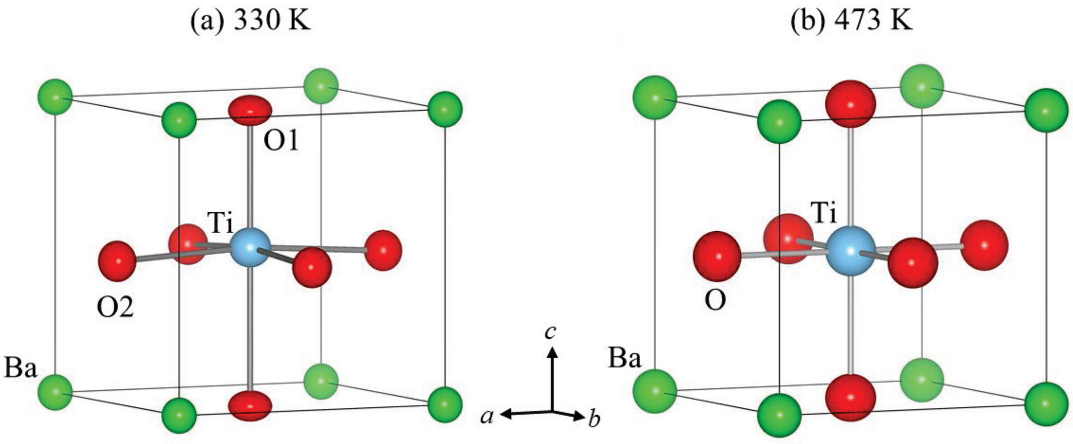

Fig. 1.4.6. ORTEP models of $BaTiO_3$ at (a) 330 K (ferroelectric phase, space group: $P4mm$) and (b) 473 K (paraelectric phase, space group: $Pm\overline{3}m$). The size of the ellipse represents the magnitude of the thermal vibration parameters.

Through the Rietveld analysis, 1080, 90, 1071, and 403 observed structure factors F_{obs} were extracted for PT at 91 K, 850 K, BT at 330 K, and 473 K, respectively. The weight for the MEM electron density analysis descrived in §1.3.4 was considered. Fig. 1.4.7 and Fig. 1.4.8 show the diffraction angle 2θ dependence of the standardized residuals $(|F_{\mathrm{obs}}| - |F_{\mathrm{MEM}}|) / \sigma_{\mathrm{obs}}$ (left) and the histogram of the standardized residuals $(|F_{\mathrm{obs}}| - |F_{\mathrm{MEM}}|) / \sigma_{\mathrm{obs}}$ (right) obtained as a result of the MEM electron density analysis for PT and BT, respectively. The top figure shows the result without weight ($n = 0$). The bottom figure shows the result with weight ($n = 1$). The normal distribution function with standard deviation $\sigma = 1$ is indicated by the black line in the figure of the histogram. The histogram should fit well with the normal distribution function if the MEM analysis is ideally performed. Without weighting, the discrepancy is noticeable on the low-angle side in the left figures, and the histogram in the right figures has a sharp distribution which does not match the normal distribution function. With weighting, the discrypancy on the low-angle side is reduced and the variability is no longer strongly dependent on 2θ in the left figures. The histogram in the right figures approaches the normal distribution function. $n = 1$ was adopted as the value of the weight, and the electron density distribution analyzed with the weight of $n = 1$ was used as the result.

(a) 91 K

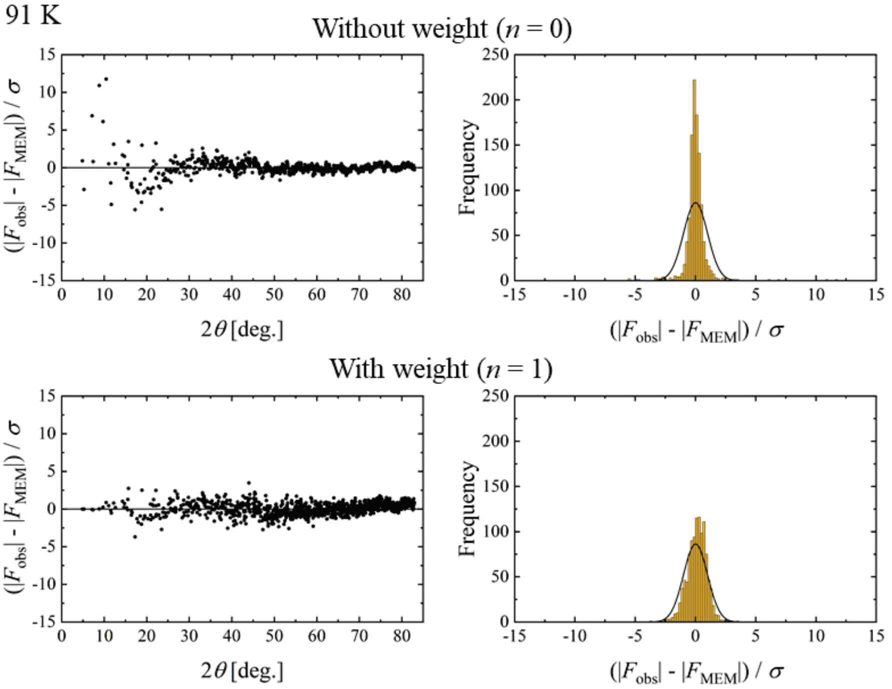

(b) 850 K

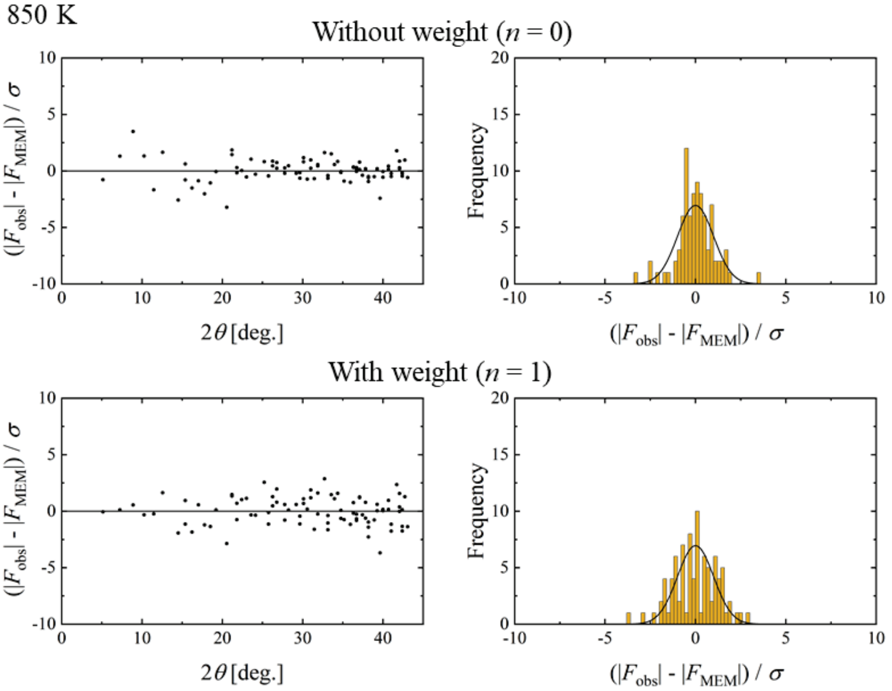

Fig. 1.4.7. Consideration of the weight for the MEM analysis of $PbTiO_3$ at (a) 91 K (ferroelectric phase) and (b) 850 K (paraelectric phase). Top: without weight and bottom: with weight. The left figure and right figure show the standardized residuals ($|F_{obs}|$ - $|F_{MEM}|$) / σ_{obs} as a function of diffraction angle 2θ and the histogram of the standardized residuals ($|F_{obs}|$ - $|F_{MEM}|$) / σ_{obs}, respectively. The histogram ideally follows a normal distribution function with standard deviation $\sigma = 1$, wrriten as a black line. The number of structure factors F_{obs} is (a) 1080 and (b) 87.

(a) 330 K

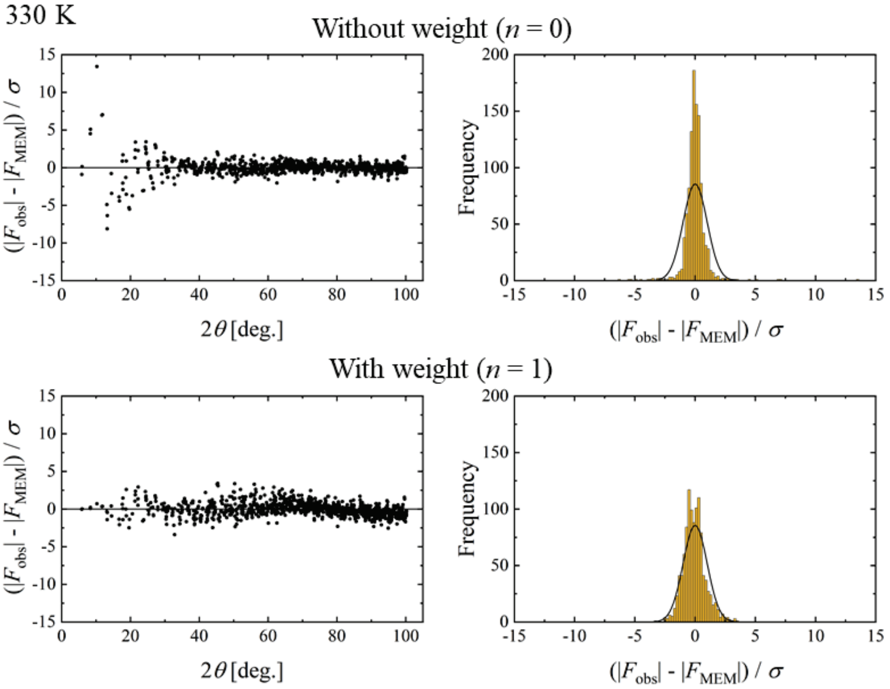

(b) 473 K

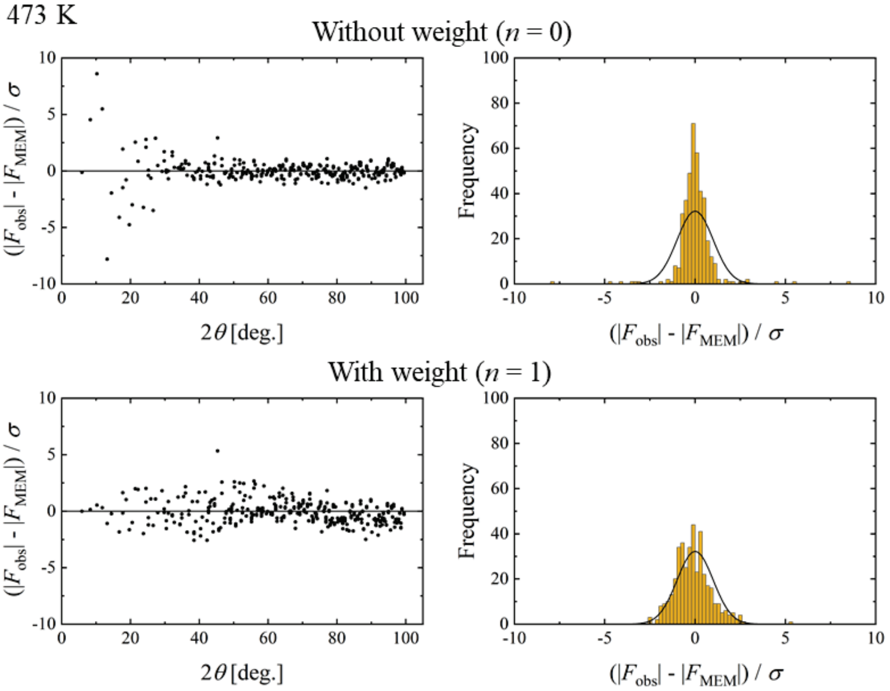

Fig. 1.4.8. Consideration of the weight for the MEM analysis of $BaTiO_3$ at (a) 330 K (ferroelectric phase) and (b) 473 K (paraelectric phase). Top: without weight and bottom: with weight. The left figure and right figure show the standardized residuals $(|F_{\mathrm{obs}}| - |F_{\mathrm{MEM}}|) / \sigma_{\mathrm{obs}}$ as a function of diffraction angle 2θ and the histogram of the standardized residuals $(|F_{\mathrm{obs}}| - |F_{\mathrm{MEM}}|) / \sigma_{\mathrm{obs}}$, respectively. The histogram ideally follows a normal distribution function with standard deviation $\sigma = 1$, wrriten as a black line. The number of structure factors F_{obs} is (a) 1071 and (b) 403.

To obtaine the total electron density distribution, the unit cell was divided into 78 × 78 × 84 units, 80 × 80 × 80 units, 80 × 80 × 80 units, and 80 × 80 × 80 units for PT at 91 K , 850 K , BT at 330 K, and 473 K, respectively. One side of one voxel corresponds to about 0.05 Å.

Figure 1.4.9 shows the total electron density distribution of PT and BT in the paraelectric phase and ferroelectric phase. The face drawn in yellow is an iso-electron density surface of 0.340*e* $Å^{-3}$, that is, the shape of an electron cloud with the electron density of 0.340*e* $Å^{-3}$. The left, right, and top planes are 2-dimensional (2D) electron density distributions for the (100), (200), and (002) planes, respectively. The contour lines are drawn in 0.2*e* $Å^{-3}$ steps, ranging from 0.340*e* $Å^{-3}$ to 1.540*e* $Å^{-3}$. In the paraelectric phase, the total electron denity distributions of PT and BT are similar. There is no overlap of the electron cloud between the *A*-site and O atoms, and the *A*-O bond is ionic. On the other hand, there is an overlap of electron coluds between the Ti and O atoms, and the Ti-O bond is covalent. In the ferroelectric phase, the total electron density distributions of PT and BT look different. There is an overlap of electron clouds between the Pb and O2 atoms, and the Pb-O2 bond is covalent. On the other hand, there is no overlap of electron clouds between the Ba and O atoms, and the Ba-O bond is also ionic in the ferroelectric phase. In PT, the upper Ti-O1 bond is covalent, while the lower Ti-O1 bond is ionic. On the other hand, in BT, both the upper and lower Ti-O1 bonds are covalent, although the magnitude of the electron density between the Ti atom and upper and lower O1 atoms is different. Therefore, Ti has a five-fold coordination in PT, while Ti has a six-fold coordination in BT. These results are consistent with previous results [27].

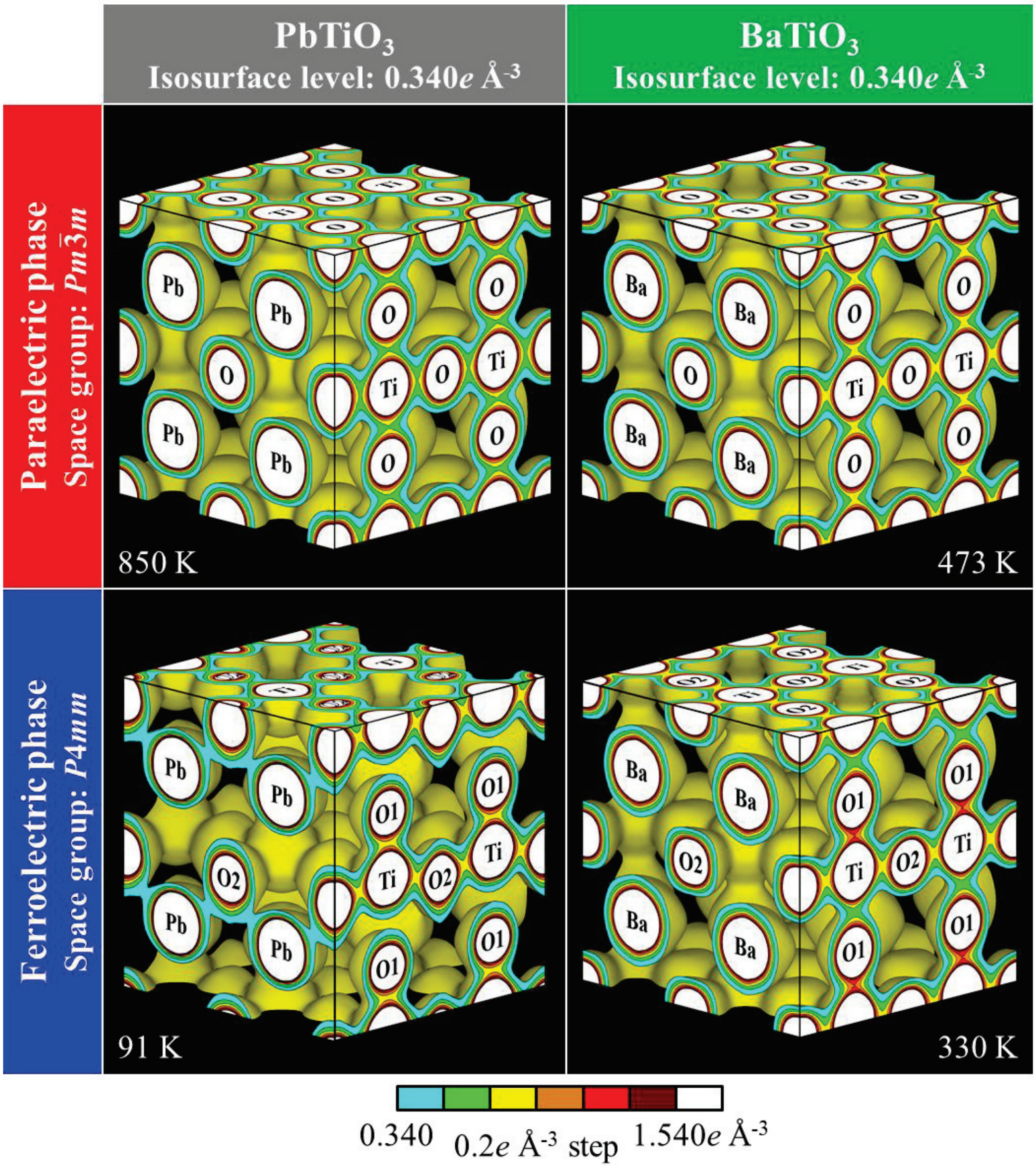

Fig. 1.4.9. Three- and two-dimensional total electron density distributions of PbTiO$_3$ and BaTiO$_3$ in the paraelectric phase and ferroelectric phase. The left, right, and top planes are 2D electron density distributions for the (100), (200), and (002) planese, respectively. The isosurface level is 0.340e Å^{-3}. The contour lines are drawn in 0.2e Å^{-3} steps, ranging from 0.340e Å^{-3} to 1.540e Å^{-3}.

The valence electron density distributions of PT and BT were determined by the valence electron density analysis discrived in §1.3.7. Fig. 1.4.10 shows the valence electron density distributions of PT and BT in the paraelectric phase and ferroelectric phase. The left, right, and top planes are 2D electron density distributions for the (100), (200), and (002) planes, respectively. In the valence electron density distributions, the spatial distribution of the valence electrons, i.e., $6s^26p^2$ ($4e^-$), $6s^2$ ($2e^-$), $3d^24s^2$ ($4e^-$), and $2p^4$ ($4e^-$) electrons are visualized for Pb, Ba, Ti, and O atoms, respectively.

In PT, the valence electrons of the Pb ion are spherically isotropic in the paraelectric phase, while in the ferroelectric phase, those are not spherically isotropic, which corresponds to the spatial distribution of lone-pair electrons of the Pb ion. The lone-pair electrons of the Pb ion are localized in the direction opposite to the Pb-O2 bond. The lone-pair electron of the Pb ion is often descrived as a $6s^2$ lone-pair. However, the lone-pair of the Pb ion seems to have both the 6s component, which is spherically distributed at the atomic position, and the 6p component, which is distributed in a bowl shape in the direction opposite to the Pb-O2 bond. Ti has the six-fold coordination in the paraelectric phase, while Ti has five-fold coordination in the ferroelectric phase.

In BT, there is almost no valence electron at the Ba site in both the paraelectric phase and ferroelectric phase, which demonstrates that the Ba-O bond is essentially ionic. This result indicates that Ba does not contribute to the ferroelectric phase transition. Ti has the six-fold coordination in both the paraelectric phase and ferroelectric phase.

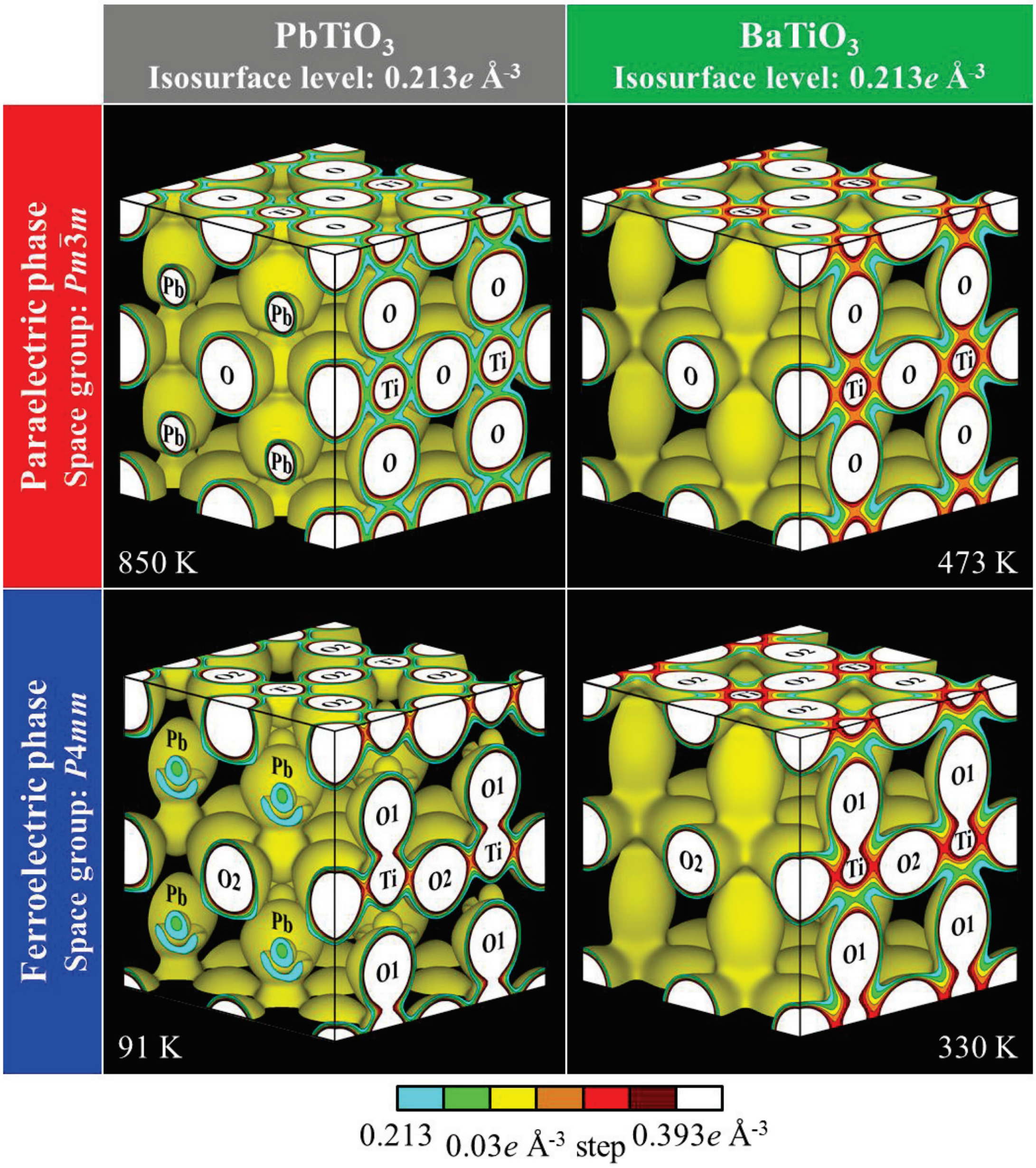

Fig. 1.4.10. Three- and two-dimensional valence electron density distributions of $PbTiO_3$ and $BaTiO_3$ in the paraelectric phase and ferroelectric phase. The left, right, and top planes are 2D electron density distributions for the (100), (200), and (002) planese, respectively. The isosurface level is 0.213*e* Å^{-3}. The contour lines are drawn in 0.03 *e* Å^{-3} steps, ranging from 0.213*e* Å^{-3} to 0.393*e* Å^{-3}.

Here, the valence elentron density distribution determined by this study is compared with that obtained by first-principles calculations [25]. Fig. 1.4.11 shows the valence electron density distribution of $PbTiO_3$ in the ferroelecric phase. The isosurface level is 0.213*e* Å^{-3} and is colored by the *z* component of the electric field from -1.0 *e* Å^{-2} (red) to

2.0 e Å^{-2} (blue). The valence electron density distribution determined by this study agrees well with that obtained by first-principles calculations [25]. The valence electron density distribution had already been calculated in the 1990s by first-principles calculations. In this study, it became possible to experimentally visualize the valence electron density distribution comparable to that obtained by first-principles calculations.

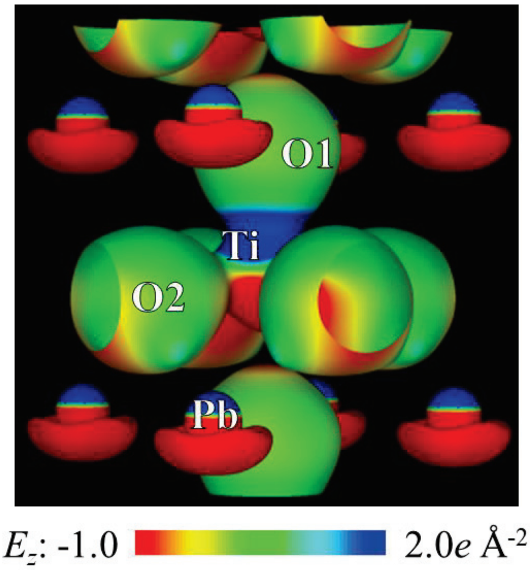

Fig. 1.4.11. Three-dimensional valence electron density distribution of $PbTiO_3$ in the ferroelectric phase. The isosurface level is 0.213e Å^{-3}. The isosurface is colored by the z component of electric field from -1.0e Å^{-2} to 2.0e Å^{-2}.

The chemical bonding nature of PT and BT was revealed by visualizing the total and valence electron density distributions. From the avobe results, the following differences were found in the crystal structure of PT and BT in the ferroelectric phase. The Pb-O bond is covalent, while the Ba-O bond is ionic. In PT, Ti has the five-fold coordination, while in BT, Ti has the 6-fold coordination. These results indicate that PT has a 2D layered structure with a network of covalent bonds in the direction perpendicular to the c-axis, while BT has a structure in which Ba is located between a 3D network of Ti-O bond, as shown in Fig. 1.4.12.

(a) $PbTiO_3$

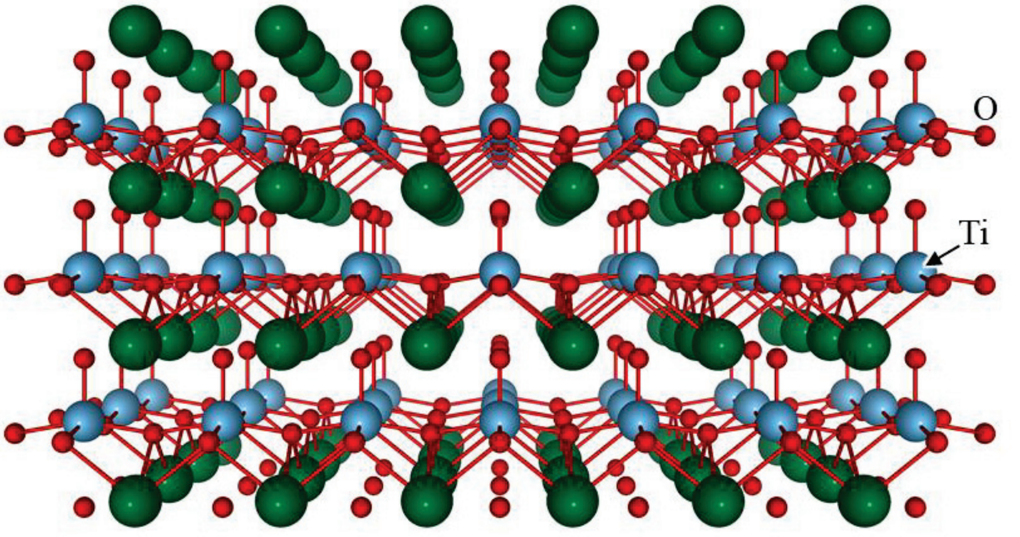

(a) $BaTiO_3$

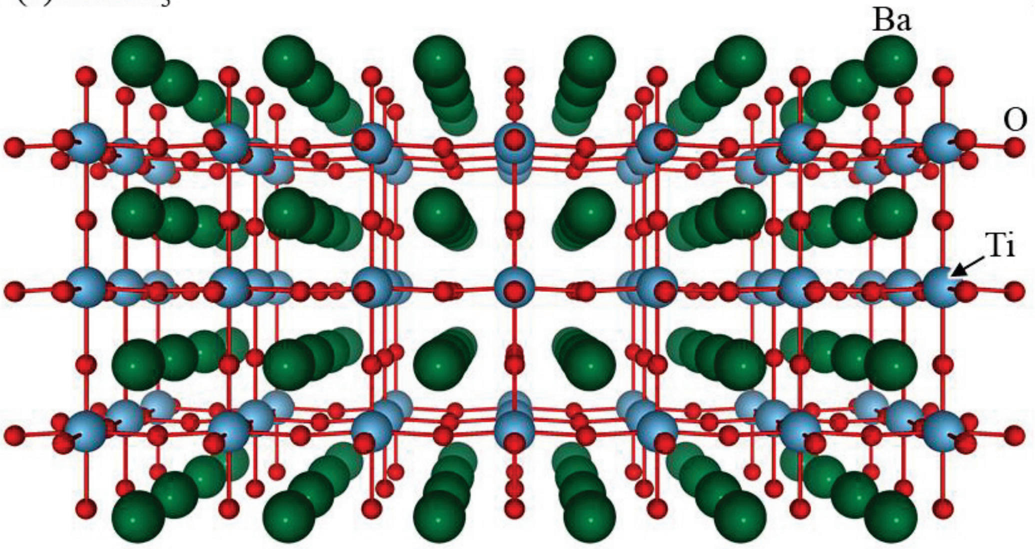

Fig. 1.4.12. Ball-and-stick model of $PbTiO_3$ and $BaTiO_3$ in the ferroelectric phase. The Pb and Ba ions are set to the same color and size.

§1.4.2. Ferroelectrisity of $PbTiO_3$ compared with $BaTiO_3$

Ionic valence of each atom in PT and BT in the ferroelectric phase were estimated by dividing the valene electron density distribution into a region for each atom based on the grid-based Bader analysis [58]. Fig. 1.4.13 shows devided valence electron density distributions of each atom in (a) $PbTiO_3$ and (b) $BaTiO_3$ in the ferroelectric phase by the grid-based Bader analysis. In BT, because there are almost no valence electrons at the Ba site, the background-level electron density of the Ti and O ions spread to the Ba site because of the MEM property. Table 1.4.3 shows estimated number of electrons and valence of each atom in (a) PT and (b) BT in the ferroelectric phase. The errors were calculated by expanding the Bader volume, devided region of the valence electron density distribution by the grid-based Bader analysis, by one voxel. The ionic valence of the Pb atom is less than the formal valence +2, which implies that the Pb atom are not fully ionized and some of the valence electrons ($6s^2 6p^2$) are transferred from Pb to O. In contrast, the ionic valence of the Ba atom is almost the same as the formal valence +2, indicating that the Ba atom is fully ionized to Ba^{2+}.

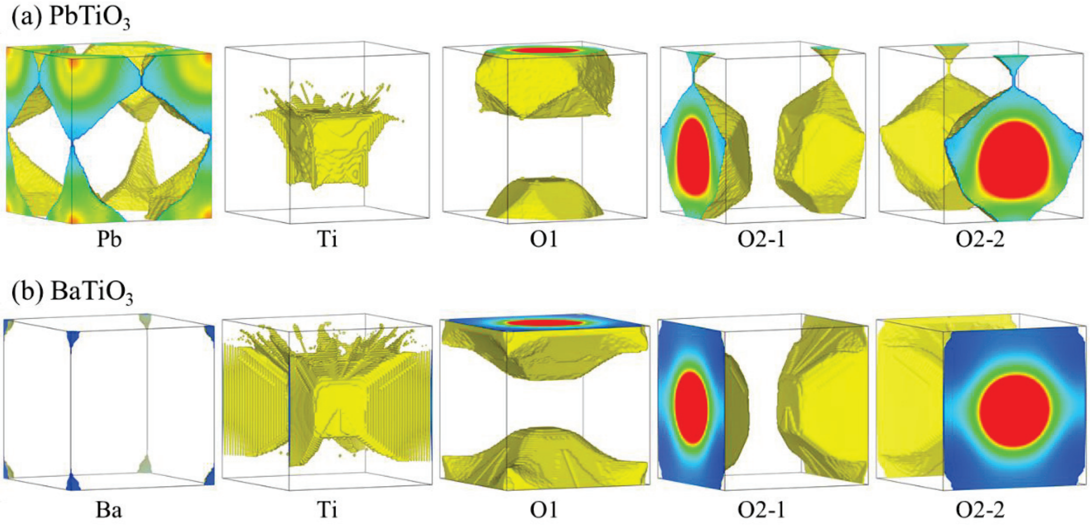

Fig. 1.4.13. Devided valence electron density distributions of each atom in (a) $PbTiO_3$ and (b) $BaTiO_3$ in the ferroelectric phase. Isodurface level is 0.01*e* Å^{-3}.

Table 1.4.3. Estimated number of valence electrons and valence of each atom in (a) $PbTiO_3$ and (b) $BaTiO_3$ in the ferroelectric phase based on the grid-based Bader analysis [58]. The errors were calculated by expanding the Bader volume by 1 voxel.

(a) $PbTiO_3$ at 91 K.

Atom	Number of valence electrons	Ionic valence
Pb	2.15(33)	+1.85(33)
Ti	1.28(26)	+2.72(26)
O1	5.50(29)	-1.50(29)
O2	5.54(31)	-1.54(31)

(b) $BaTiO_3$ at 330 K.

Atom	Number of valence electrons	Ionic valence
Ba	0.0018(20)	+1.9982(20)
Ti	1.00(58)	+3.00(58)
O1	6.15(27)	-2.15(27)
O2	5.43(27)	-1.43(27)

The spontaneous polarization of PT and BT in the ferroelectric phase was estimated as follows. The charge density distribution can be written as

$$\rho_{\mathrm{total}}(\boldsymbol{r}) = \rho_{\mathrm{nucl}}(\boldsymbol{r}) + \rho_{\mathrm{el}}(\boldsymbol{r}), \tag{1.4.1}$$

where $\rho_{\mathrm{nucl}}(\boldsymbol{r})$ and $\rho_{\mathrm{el}}(\boldsymbol{r})$ are positicve charge density distribution and electron density distribution, respectively. By decomposing Eq. (1.4.1) into inner-shell and outer-shell, Eq. (1.4.2) can be obtained.

$$\begin{aligned}\rho_{\mathrm{total}}(\boldsymbol{r}) = {} & \rho_{\mathrm{nucl}}^{\mathrm{inner-shell}}(\boldsymbol{r}) + \rho_{\mathrm{nucl}}^{\mathrm{outer-shell}}(\boldsymbol{r}) \\ & + \rho_{\mathrm{el}}^{\mathrm{inner-shell}}(\boldsymbol{r}) + \rho_{\mathrm{el}}^{\mathrm{outer-shell}}(\boldsymbol{r}) \\ = {} & \left\{\rho_{\mathrm{nucl}}^{\mathrm{inner-shell}}(\boldsymbol{r}) + \rho_{\mathrm{el}}^{\mathrm{inner-shell}}(\boldsymbol{r})\right\} \\ & + \left\{\rho_{\mathrm{nucl}}^{\mathrm{outer-shell}}(\boldsymbol{r}) + \rho_{\mathrm{el}}^{\mathrm{outer-shell}}(\boldsymbol{r})\right\} \\ = {} & \rho^{\mathrm{inner-shell}}(\boldsymbol{r}) + \rho^{\mathrm{outer-shell}}(\boldsymbol{r}).\end{aligned} \tag{1.4.2}$$

Here, $\rho_{\mathrm{nucl}}^{\mathrm{inner-shell}}(\boldsymbol{r})$ and $\rho_{\mathrm{nucl}}^{\mathrm{outer-shell}}(\boldsymbol{r})$ are positive charge density distribution corresponding to the number of electrons in $\rho_{\mathrm{el}}^{\mathrm{inner-shell}}(\boldsymbol{r})$ and $\rho_{\mathrm{el}}^{\mathrm{out-shell}}(\boldsymbol{r})$, respectively. Fig. 1.4.14 shows a schematic view of the division of the $\rho_{\mathrm{total}}(\boldsymbol{r})$. Only the electron density distribution can be determined by X-ray diffraction experiments. The positive charge (nucleus) is assumed to exist as a point charge at an atomic position. The spread of $\rho_{\mathrm{nucl}}(\boldsymbol{r})$ is extremely small compared to $\rho_{\mathrm{el}}(\boldsymbol{r})$. The valence electron density distribution determined in this study is $\rho_{\mathrm{el}}^{\mathrm{outer-shell}}(\boldsymbol{r})$.

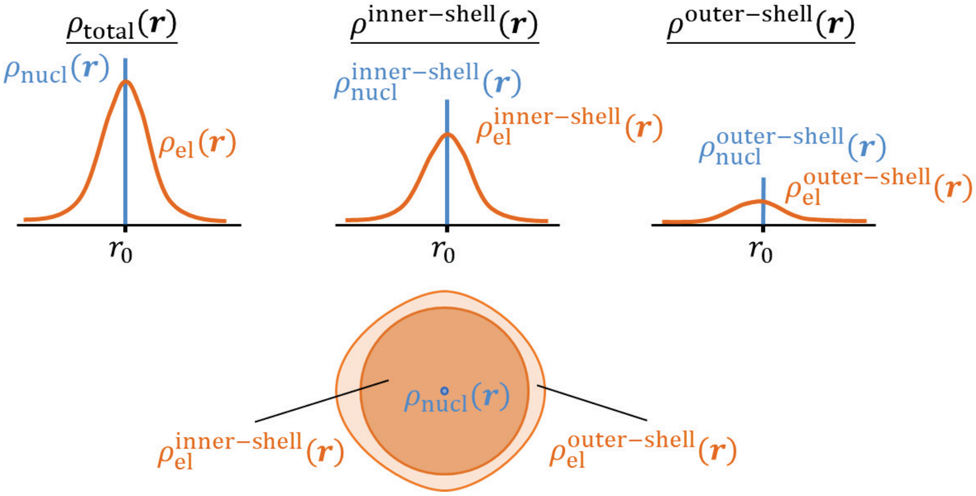

Fig. 1.4.14. Schematic view of the division of the $\rho_{\mathrm{total}}(\boldsymbol{r})$.

For $\rho^{\mathrm{inner-shell}}(\boldsymbol{r})$, there is no contribution to the spontaneous polarization, as $\int_{V_j} \rho^{\mathrm{inner-shell}}(\boldsymbol{r})\,\mathrm{d}\boldsymbol{r} = 0$ in the range V_j of a certain atom j and the distribution is isotropic. On the other hand, for $\rho^{\mathrm{outer-shell}}(\boldsymbol{r})$, $\int_{V_j} \rho^{\mathrm{outer-shell}}(\boldsymbol{r}) d\boldsymbol{r} \neq 0$ due to the transitions of electrons due to the covalent bonding, etc., and the distribution is aanisotropic, resulting in electric polarization.

Then, $\rho^{\mathrm{outer-shell}}(\boldsymbol{r})$ can be transformed as follows:

$$\begin{aligned}\rho^{\mathrm{outer-shell}}(\boldsymbol{r}) &= \rho_{\mathrm{nucl}}^{\mathrm{outer-shell}}(\boldsymbol{r}) + \rho_{\mathrm{el}}^{\mathrm{outer-shell}}(\boldsymbol{r}) \\ &= \rho_{\mathrm{nucl}}^{\mathrm{outer-shell}}(\boldsymbol{r}) + \rho_{\mathrm{el}}^{\mathrm{outer-shell,point}}(\boldsymbol{r}) \\ &\quad - \rho_{\mathrm{el}}^{\mathrm{outer-shell,point}}(\boldsymbol{r}) + \rho_{\mathrm{el}}^{\mathrm{outer-shell}}(\boldsymbol{r}) \\ &= \left\{\rho_{\mathrm{nucl}}^{\mathrm{outer-shell}}(\boldsymbol{r}) + \rho_{\mathrm{el}}^{\mathrm{outer-shell,point}}(\boldsymbol{r})\right\} \\ &\quad + \{-\rho_{\mathrm{el}}^{\mathrm{outer-shellpoint}}(\boldsymbol{r}) + \rho_{\mathrm{el}}^{\mathrm{outer-shell}}(\boldsymbol{r})\} \\ &= \rho_{\mathrm{m}}^{\mathrm{outer-shell}}(\boldsymbol{r}) + \rho_{\mathrm{d}}^{\mathrm{outer-shell}}(\boldsymbol{r}).\end{aligned} \tag{1.4.3}$$

Here, $\rho_{\mathrm{el}}^{\mathrm{outer-shell,point}}(\boldsymbol{r})$ is a delta function that satisfies the following conditions:

$$\begin{gathered}\rho_{\mathrm{el}}^{\mathrm{outer-shell,point}}(\boldsymbol{r} = \text{atomic position}) = \frac{n_{\mathrm{el}}^{\mathrm{outer-shell}}}{v}, \\ \rho_{\mathrm{el}}^{\mathrm{outer-shell,point}}(\boldsymbol{r} \neq \text{atomic position}) = 0,\end{gathered} \tag{1.4.4}$$

where v is the volume of a voxel, $n_{\mathrm{el}}^{\mathrm{outer-shell}}$ is the number of valence electrons of the atom j. $n_{\mathrm{el}}^{\mathrm{outer-shell}}$ is represented by Eq. (1.4.5).

$$
\begin{aligned}
n_{\mathrm{el}}^{\mathrm{outer-shell}} &= v\int_{V_j} \rho_{\mathrm{el}}^{\mathrm{outer-shell}}(\boldsymbol{r})\mathrm{d}\boldsymbol{r}, \\
&= v\int_{V_j} \rho_{\mathrm{el}}^{\mathrm{outer-shell,point}}(\boldsymbol{r})\mathrm{d}\boldsymbol{r}.
\end{aligned} \tag{1.4.5}
$$

For $\rho_{\mathrm{m}}^{\mathrm{outer-shell}}(\boldsymbol{r})$, $v\int_{V_j}\rho_{\mathrm{m}}^{\mathrm{outer-shell}}(\boldsymbol{r})\,\mathrm{d}\boldsymbol{r} = Z_j$, where Z_j is the valence of the atom j, which means that the point charge of the valence Z_j exists in the atomic position, resulting in the ionic polarization (monopole). On the other hand, for $\rho_{\mathrm{d}}^{\mathrm{outer-shell}}(\boldsymbol{r})$, $\int_{V_j}\rho_{\mathrm{d}}^{\mathrm{outer-shell}}(\boldsymbol{r})dr = 0$, but the anisotropy of $\rho_{\mathrm{el}}^{\mathrm{outer-shell}}(\boldsymbol{r})$ causes electric dipole moments, i.e., the electronic polarization (dipole). Fig. 1.4.15 shows a schematic view of $\rho_{\mathrm{m}}^{\mathrm{outer-shell}}(\boldsymbol{r})$ and $\rho_{\mathrm{d}}^{\mathrm{outer-shell}}(\boldsymbol{r})$.

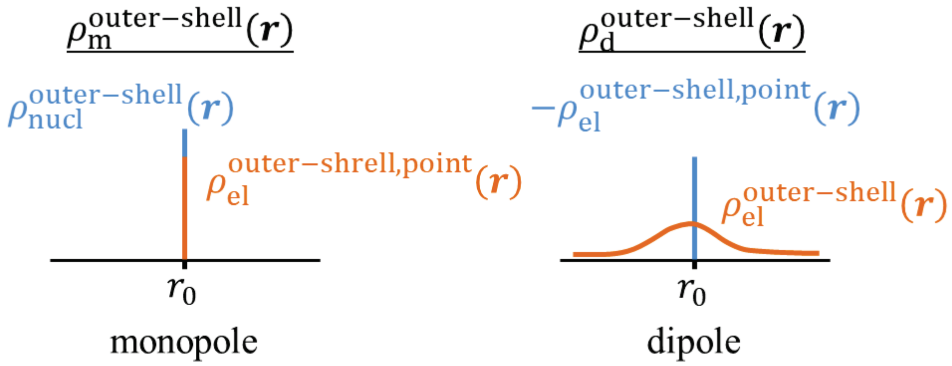

Fig. 1.4.15. Schematic view of $\rho_{\mathrm{m}}^{\mathrm{outer-shell}}(\boldsymbol{r})$ and $\rho_{\mathrm{d}}^{\mathrm{outer-shell}}(\boldsymbol{r})$.

Therefore, to calculate the spontaneous polarization $\boldsymbol{P}_{\mathrm{S}}$, first, the valence electron density distribution is divided into each atom. The ionic polarization $\boldsymbol{P}_{\mathrm{I}}$ is calculated by the point-charge model using the valence estimated from $\rho_{\mathrm{m}}^{\mathrm{outer-shell}}(\boldsymbol{r})$.

$$
\boldsymbol{P}_{\mathrm{I}} = \frac{1}{V_{\mathrm{unit\ cell}}}\sum_j eZ_j\Delta\boldsymbol{r}_j, \tag{1.4.6}
$$

where e is the elementary charge, $V_{\mathrm{unit\ cell}}$ is the volume of the unit cell, Z_j is the estimated valence of atom j, and $\Delta\boldsymbol{r}_j$ is the displacement vector. The electronic polarization $\boldsymbol{P}_{\mathrm{E}}$ is represented by the Eq. (1.4.7) from the definition of polarization.

$$
\begin{aligned}
\boldsymbol{P}_{\mathrm{E}} &= \frac{1}{V_{\text{unit cell}}} \int^{V_{\text{unit cell}}} \boldsymbol{r}\rho_{\mathrm{d}}^{\text{outer-shell}}(\boldsymbol{r})\, \mathrm{d}\boldsymbol{r} \\
&= \frac{1}{V_{\text{unit cell}}} \sum_{\text{unit cell}} \boldsymbol{r}\rho_{\mathrm{d}}^{\text{outer-shell}}(\boldsymbol{r}) \\
&= \frac{1}{V_{\text{unit cell}}} \left\{ \sum_{\text{atom 1}} \boldsymbol{r}\rho_{\mathrm{d}}^{\text{outer-shell}}(\boldsymbol{r}) + \sum_{\text{atom 2}} \boldsymbol{r}\rho_{\mathrm{d}}^{\text{outer-shell}}(\boldsymbol{r}) \right. \\
&\qquad \left. + \cdots + \sum_{\text{atom } j} \boldsymbol{r}\rho_{\mathrm{d}}^{\text{outer-shell}}(\boldsymbol{r}) \right\} \\
&= \frac{1}{V_{\text{unit cell}}} (\mu_{\text{atom 1}} + \mu_{\text{atom 2}} + \cdots + \mu_{\text{atom } N}).
\end{aligned} \tag{1.4.7}
$$

The contribution of each atom to the electronic polarization is

$$
\boldsymbol{P}_{\text{E,atom } j} = \frac{1}{V_{\text{unit cell}}} \mu_{\text{atom } j}. \tag{1.4.8}
$$

Since the origin is in the atomic position, the contribution to the electronic polarization of the $\rho_{\mathrm{el}}^{\text{outer-shell,point}}$ is negligible. Therefore, the electronic polarization is calculated using $\rho_{\mathrm{el}}^{\text{outer-shell}}(\boldsymbol{r})$, i.e., the valence electron density distribution, rather than $\rho_{\mathrm{d}}^{\text{outer-shell}}$. The spontaneous polarization $\boldsymbol{P}_{\mathrm{S}}$ is calculated by summing $\boldsymbol{P}_{\mathrm{I}}$ and $\boldsymbol{P}_{\mathrm{E}}$.

The valence electron density distribution has already been divided by the grid-based Bader analysis as shown in Fig. 1.4.13. Using divided valence electron density distribution and estimated valence of each atom, the ionic polarization and electronic polarization of PT were calculated. Fig. 1.4.16 shows a schematic view of the calculation method for the electronic polarization using the Pb ion as an example. The contribution of each voxel to the electronic polarization is larger when the valence electron density is larger and when the z-component of $\boldsymbol{r}_j$ is larger. The contributions of each atom in PT to the electronic polarization were estimated to be 13.5 μC/cm^2, 1.3 μC/cm^2, 0.2 μC/cm^2 and 4.4 × 2 μC/cm^2 for the Pb, Ti, O1, and O2 ions, respectively. Then the electronic polarization $\boldsymbol{P}_{\mathrm{E}}$ of PT was calculated to be 23.8 μC/cm^2. The ionic polarization $\boldsymbol{P}_{\mathrm{I}}$ of PT was estimated to be 47.4 μC/cm^2. Finaly, the spontaneous polarization of PT was calculated to be 71.2 μC/cm^2 which is consistent with the experimental value of 75 μC/cm^2 [17]. The contribution of electronic polarization to the spontaneous polarization is comparably large, about 33%. Among them, the contribution of the Pb ion is the largest, which is thought to be caused by the asymmetric p-component of the lone-pair electrons of the Pb ion.

The spontaneous polarization of BT was also estimated in the same way. The contribution of each atom in BT to the electronic polarization was estimated to be 0.00 μC/cm^2, -0.02 μC/cm^2, -0.15 μC/cm^2 and -0.34 × 2 μC/cm^2 for the Ba, Ti, O1, and O2 ions, respectively. Then the electronic polarization of BT was calculated to be about -0.9 μC/cm^2. The ionic polarization of BT was estimated to be 13.9 μC/cm^2. Finaly, the spontaneous polarization of BT was calculated to be 13.0 μC/cm^2 which is not consistent with the experimental value of 26 μC/cm^2 [16]. The reason why the spontaneous polarization could not be estimated well in BT is thought to be that, as shown in Fig. 1.4.13, there is almost no valence electron at the Ba site, and because of the MEM property, the background-level valence electrons of the Ti and O ions spread to the Ba site, and the valence electron density distribution was not separated well, or the measured value of spontaneous polarization of BT is affected by the domein boundary and the gradient lattice strain layer.

These estimations are possible because the valence electron density distribution has been determined. If the total electron density distribution is used, these estimations cannot be made correctly because of the large contribution of inner-core electrons.

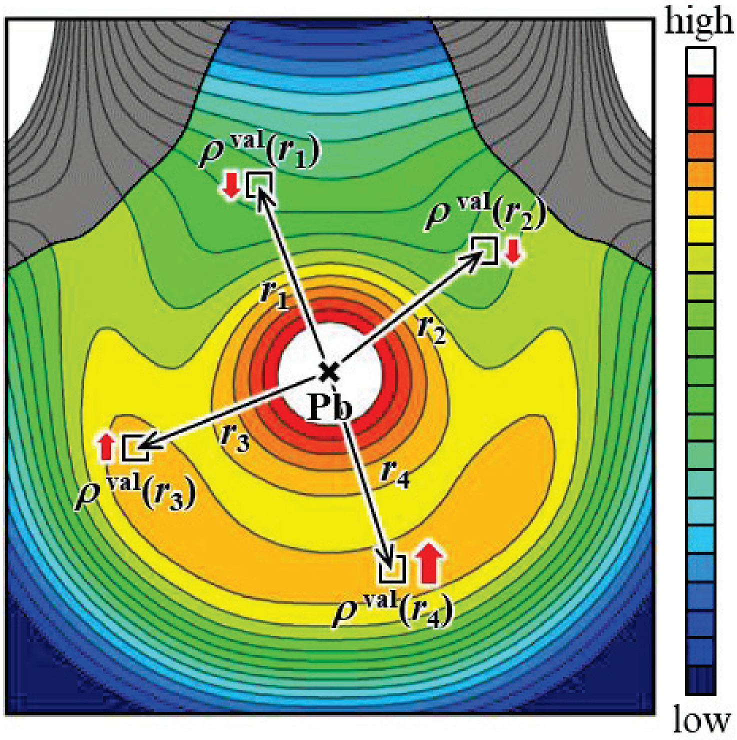

Fig. 1.4.16. Schematic view of the calculation method for the electronic polarization using the Pb ion as an example. Divided two-dimensional valence electron density distribution of the Pb ion. “×” mark indicates the atomic position of Pb. Squares represent voxels of the valence electron density distribution. Black arrows in dicate vectors from the origin to each voxel. Red arrows represent the magnitude of the contribution of each voxel to the electronic polarization. The contribution of each voxel to the electronic polarization is larger when the valence electron density is larger and when the z-component of $\boldsymbol{r}_j$ is larger.

Based on the previous first-principles calculations study and the results obtained by this study, the differences in the cubic to tetragonal phase transition between PT and BT can be summarized as follows. At phase transition temperature, the ferroactive Ti ion causes the change of the Ti-O orbital hybridization, thereby reducing symmetry from $Pm\bar{3}m$ to $P4mm$ [24] [25]. In the case of BT, O ions are displaced to opposite direction to the Ti displacement because the Ba-O bond is ionic. As a result, the Slater-mode-type atomic displacement pattern is realized. In the case of PT, orbital hybridization is formed between the approaching Pb and O ions, and some electrons occupy the bonding orbitals [26]. Through the Pb-O covalent bond, electrons are transferred from the Pb ion to O ions, and the remaining lone-pair electrons are localized in the direction opposite to the Pb-O bond. The Pb-O covalent bond and the stereochemically active lone-pair electrons shift the entire TiO_6 octahedron. As a result, the directions of the Ti and O atomic displacements are the same, and the atomic displacement pattern with a large contribution from the Last-mode-type atomic displacement pattern is realized. The Pb-O covalent bond and lone-pair electrons enhance the spontaneous lattice distortion, resulting in the large ionic polarization. The Pb ion is polarized due to the anisotropic distribution of the lone-pair electrons, which is the cause of the large electronic polarization. These are the origins of PT having a larger spontaneous polarization than BT.

§1.4.3. Brief summary

In part 1, the method to visualize the spatial distribution of valence electrons was deviced, and the valence electron density distributions of $PbTiO_3$ and $BaTiO_3$ in both the paraelectric phase and ferroelectric phase were determined using synchrotron radiation X-ray diffraction data with help of first-principles calculations. The electronic polarization of Pb due to the anisotropic distribution of lone-pair electrons of the Pb ion, which had been suggested by first-principles calculations, was presented. The spontaneous polarization of $PbTiO_3$ was successfully estimated by calculating both the ionic polarization and electronic polarization from the valence electron density distribution.

It is now possible to determine a valence electron density distribution comparable to that obtained by first-principles calculations. I hope that this method will lead to further development of research on the materials structure physics. The valence electron density distributions obtained experimentally include information about atomic fluctuations, such as thermal vibrations. This information is not included in the valence electron density distributions obtained by first-principles calculations. On the other hand, first-principles calculations allow us to investigate the electron density distribution for each orbital, which is difficult to do experimentally. Therefore, the complementary use of experiments and first-principles calculations is important for future research on the materials structure physics.

Part 2: Deposition mechanism of ferroelectric $Bi_4Ti_3O_{12}$ aerosol deposition film

Chapter 2.1: Introduction

§2.1.1. Aerosol deposition (AD) method

Conventinally, ceramics have been used in various industries, mainly as bulk materials. In recent years, however, new materials and components have been commercialized by covering the surface of the materials with ceramics or making it function as a thin film in order to take advantage of its high heat resistance, mechanical properties, and multifunctional characteristics. For example, the abrasion, corrosion, and oxidation resistance of ceramic coatings can be used to significantly improve product performance, lifespan, and range of use. Therefore, in the aircraft and automotive industries, ceramic coatings are beginning to be used not only to improve the heat resistance of engines, but also in a wide range of fields such as tools, molds, machine parts, semiconductor components, manufacturing equipment and industrial machinery. Coating technologies such as high integration, multilayer, and flexibility are also key parameters that determine device paformance in electronic components such as capacitors, filters, ceramic semiconductors, and transparent conductive films used in electronic devices and in sensing technologies that support IOT. Research and development of coating technologies such as chemical vapor deposition, palse laser deposition, vapor deposition, ion plating, sputtering, sol-gel method, and thermal spraying have been carried out for ceramics materials. However, in order to respond to the needs of industry, it is important to develop elemental technologies such as low temperature and high-speed processes, and dissimilar material layering and compositing [59].

Aerosol deposition (AD) method is a method to form a ceramic film by spraying aerosol consisting of ceramic fineparticles and gas onto a substrate material under reduced pressure at room temperature (RT) [60] [61] [62]. The AD method is positioned as an extension of the conventional thermal spraying technology in that crystalized ceramics are sprayed onto the substrate to form the film by gas transport. In the AD method, however, the particles are not melted as in the thermal spraying method, but are sprayed onto the substrate while still in the solid state by using the room temperature impact consolidation (RTIC) phenomenon [60] [63] [64] to form a film at RT. Fig. 2.1.1 shows the (a) schematic view and (b) photograph of the AD apparatus [60]. The AD apparatus consists of two chambers. The first is an aerosol-generation chamber and the second is a deposition chamber. The aerosol-generation chamber has a carrier gas system and a vibration system, which are used to generate aerosol. The deposition chamber contains a nozzle and a substrate holder and is used to form a film. The procedure for film formation in the AD method is shown below. First, the aerosol is generated by mixing starting powder and gas. The aerosol is transported into the deposition chamber due to the pressure difference between the two chambers. The aerosol is then sprayed onto the substrate through the nozzle and a film is formed. In the AD method, by optimizing the particle size of the starting powder and deposition conditions, dense, thick, and transparent films can be produced at high speed at RT. Fig. 2.1.2 shows typical AD films, (a) PZT film with thickness of over 500 μm, (b) α-Al_2O_3 film with thickness of 4 μm and transparency of 99% @ 400 – 900 nm, and (c) wide-area coating of 200×200 mm^2 [60].

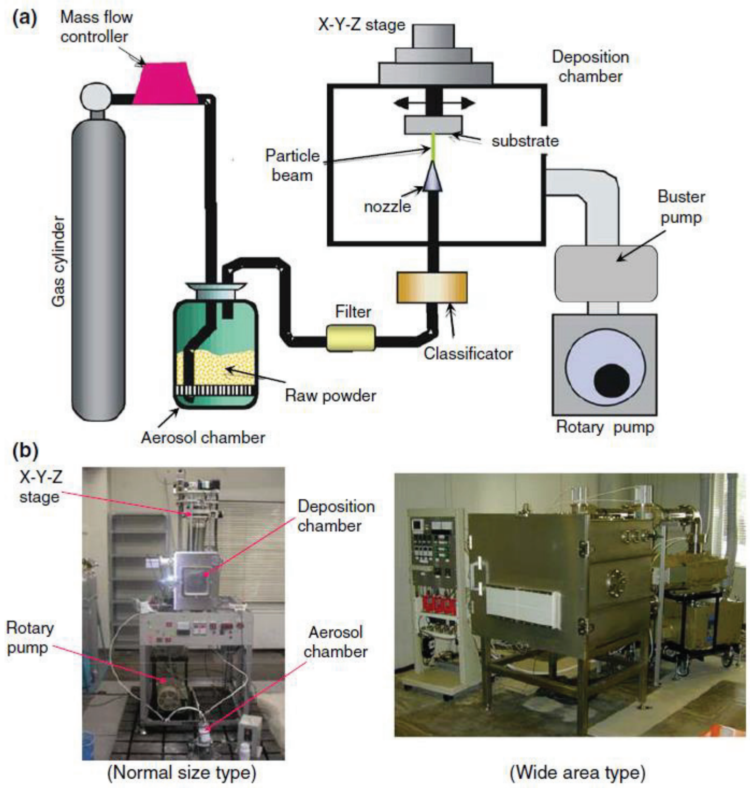

Fig. 2.1.1. Deposition apparatus for the AD method [60]. (a) Schematic view and (b) photographs.

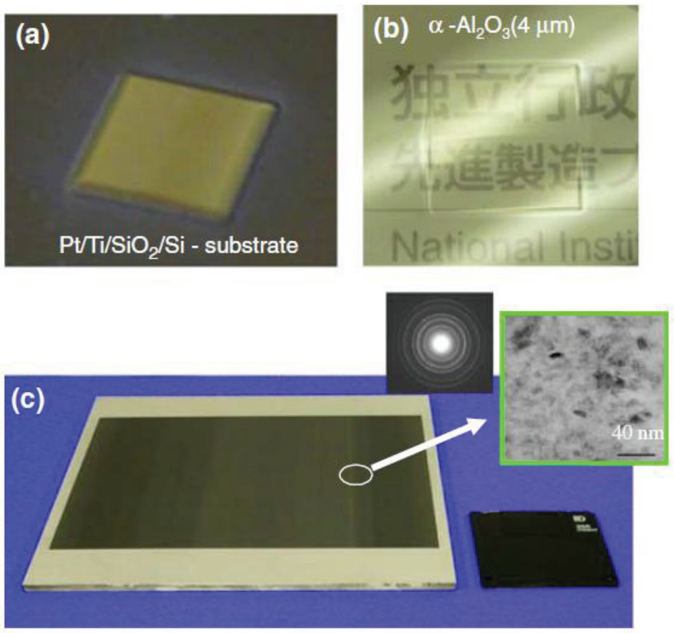

Fig. 2.1.2. Typical AD films. (a) Thick PZT film: over 500 µm, (b) transparent α-Al_2O_3 film: 99% @ 400 – 900 nm, and (c) wide area coating: 200 × 200 mm^2 [60].

Mechanisms of the AD method have been studied by experiments and simulations. The AD process can be separated into 2 steps. Fig. 2.1.3 shows stages of the AD film formation [61]. In the first step, a layer called the anchoring layer is formed on the substrate. In the second step, the film formation and growth are occured by RTIC. Fig. 2.1.4 shows microstructure of α-Al_2O_3 AD film [60], (a) cross-section Scanning Electron Microscope (SEM) image of the as-deposited AD film at RT, (b) comparison of XRD profiles for the starting powder, AD film and bulk sample, and (c) Transmission Electron Microscope (TEM) image of the starting powder, and as-depisited AD film at RT. In Fig. 2.1.4 (c), the anchoring layer with thickness of 100 – 200 nm was observed. Either amorphose layers or hetero structures were not observed at the boundary of the crystal grain. XRD profiles show that α-Al_2O_3 particles were retained in the AD film. However, the peak width of the AD film is broader than that of the srating powder and the peak position of the AD film slightly shifts compared to that of the starting powder, which is caused by the reduction of the crystallite size of the AD film and/or the distortion during the deposition.

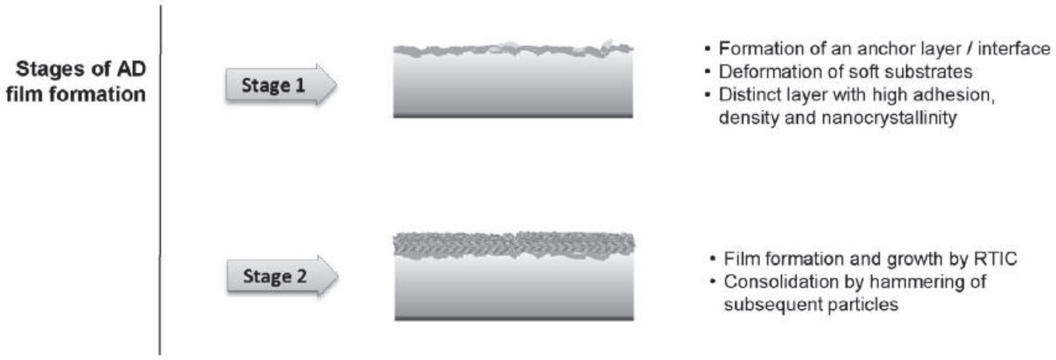

Fig. 2.1.3. Stages of AD film formation [61].

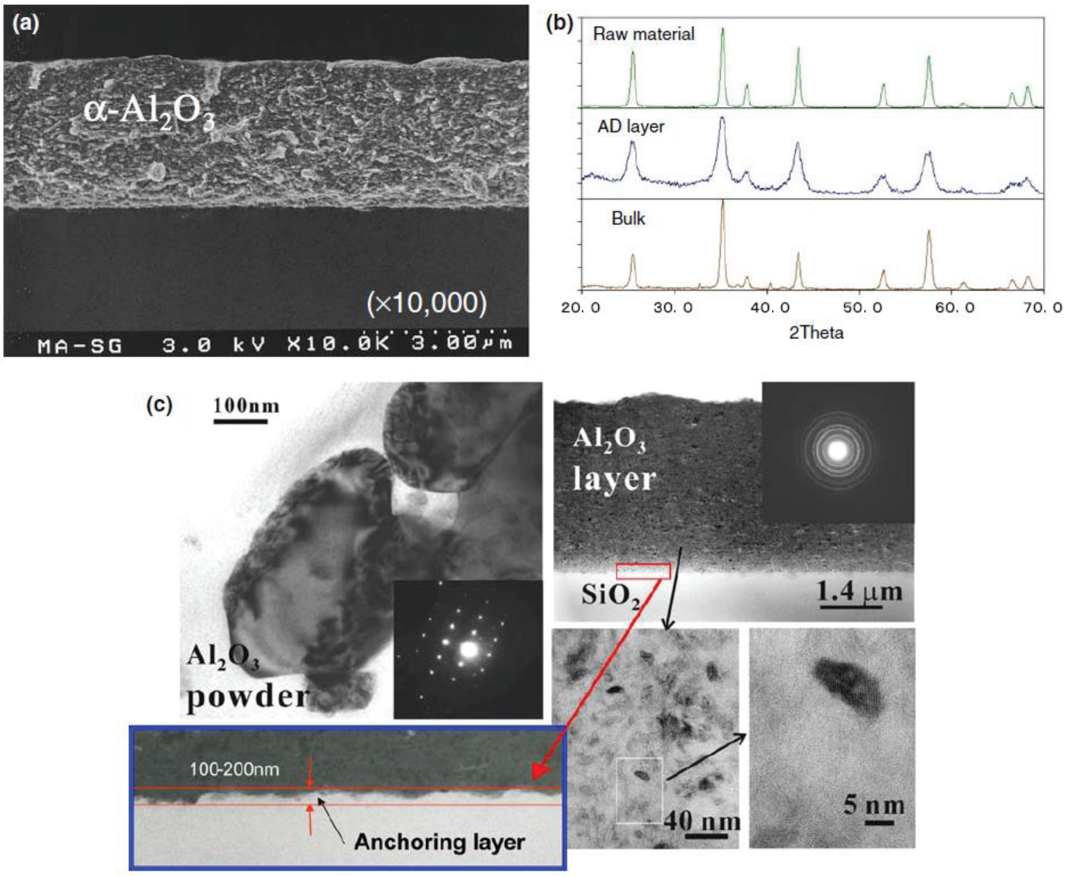

Fig. 2.1.4. Microstructure of α-Al_2O_3 AD film [60]. (a) Cross-section SEM imae of the as-deposited AD film at RT. (b) Comparison of XRD profiles for the starting powder, AD film and bulk sample. (c) TEM images of the starting powder and as-deoisited AD film at RT.

A velocity of the particles during the AD method was measured by a time-of -flight method [64]. The velocities of the particle impact were estimated to be from 150 to 500 m/s. Fig. 2.1.5 shows relationships between the velocity of particles and gas consumption with a nozzle of 10×0.4 mm^2 [60]. The critical velocity for RTIC, in other word, the minimum velocity that the AD film is formed, is about 150 m/s. This velocity is smaller than that in other methods. Fig. 2.1.6 shows comparison of various methods for film deposition by impact adhesion of solid particles [62]. Finite-element method (FEM) computational simulations were performed to simulate the local temperature rise and shock pressure at the point of impact between the particle and substrate douring the AD process using the measured velocity of the particle impact as shown in Fig. 2.1.7 [64]. In the simulation, the particle size and velocity of the particle were set to 0.3 μm and 300m/s, respectively. The maximum local temperature rise, and shock pressure were estimated to be less than 500 °C and 2.5 GPa, respectively. These results indicate that melting of the particles does not occure during the AD process. Therefore, it has been thought that the dense structure of the AD film is due to the reduction of the crystallite size by fracture and/or plastic deformation caused by the collision of the particles with the substrate.

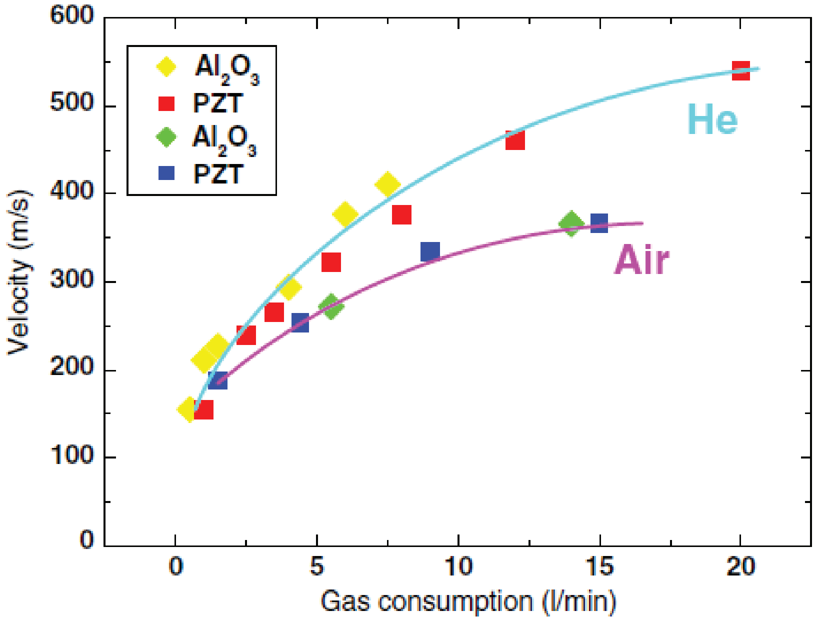

Fig. 2.1.5. Relationships between the velocity of the particles and gas consumption with a nozzle of 10 × 0.4 mm^2 [60].

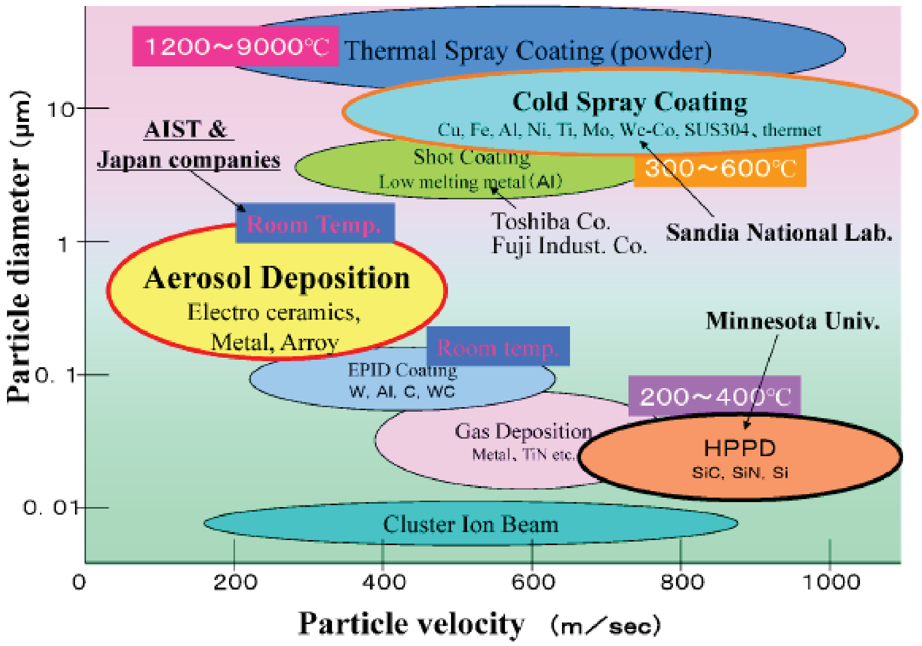

Fig. 2.1.6. Comparison of various methods for film deposition by impact adhesion of solid particles [62].

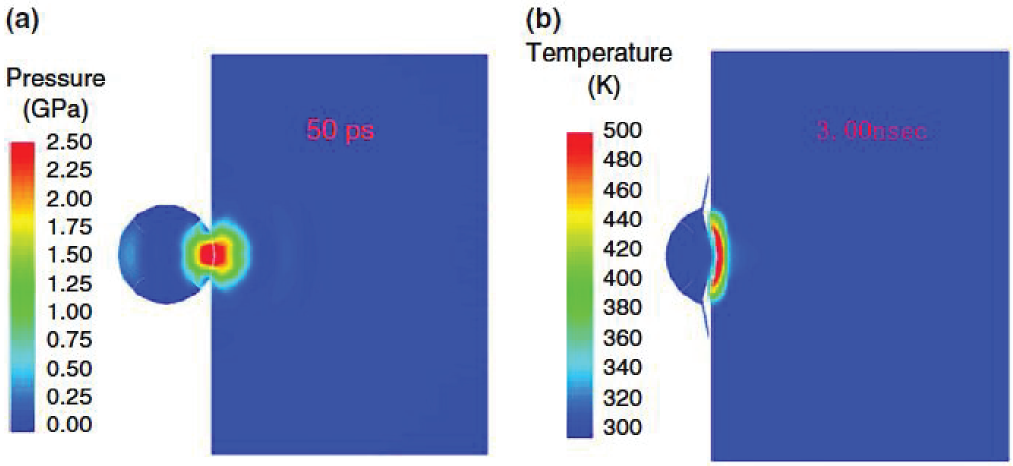

Fig. 2.1.7. Local (a) temperature rise and (b) shock pressure at the point of collision between the particle and substrate simulated by the FEM simulations [64]. The particle size was set to 0.3 μm. The velocity of the particle was set to 300 m/s.

In addition to the particle velocity, the particle size and mechanical properties of the starting powder also have a large effect on the film growth and film density. Fig. 2.1.8 shows the particle size of the starting powder dependence of the AD method [62]. When the α-Al_2O_3 powder with the particle size of sub-micron order and irregular particle shape was used as the starting powder and the particle collision velocity was 200 m/s, a dense and transparent AD film was formed. Hoevwer, when the α-$\mathrm{Al_2O_3}$ powder with the particle size of about 50 nm and sphericala shape was used as the starting powder and the particle collision velocity was 400 m/s, the AD film could not be formed, and a pressed compact was formed. Furthermore, when the α-$\mathrm{Al_2O_3}$ powder with the particle size of 5 μm or larger, which can be regarded as a single crystal, was used as the starting powder and the particle collision velocity was 200 m/s, the AD film was not formed and sandblasting-like etching of the substrate occurred.

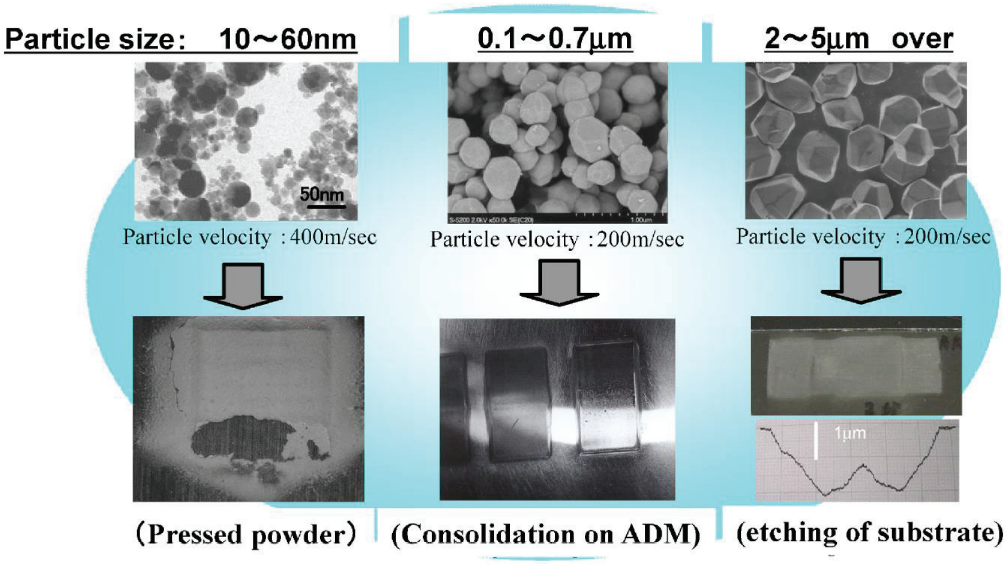

Fig. 2.1.8. Particle size of the starting powder dependence of the AD method [62]. The starting powder is α-$\mathrm{Al_2O_3}$.

D.-W. Lee *et al.* carried out sequential SEM and Atomic Force Microscope (AFM) experiments by increasing number of scans to investigate how dense and thick α-$\mathrm{Al_2O_3}$ AD films are formed at RT [65]. Fig. 2.1.9 shows SEM images of α-$\mathrm{Al_2O_3}$ AD films deposited on Cu substrates with increasing scans. They investigated that the use of 0.5 μm α-$\mathrm{Al_2O_3}$ particles resulted in the formation of high-hardness and dense AD films, in contrast to the use of larger particles or agglomerated particles. It was also concluded that the anchoring layer was formed by the plastic deformation of the starting powder.

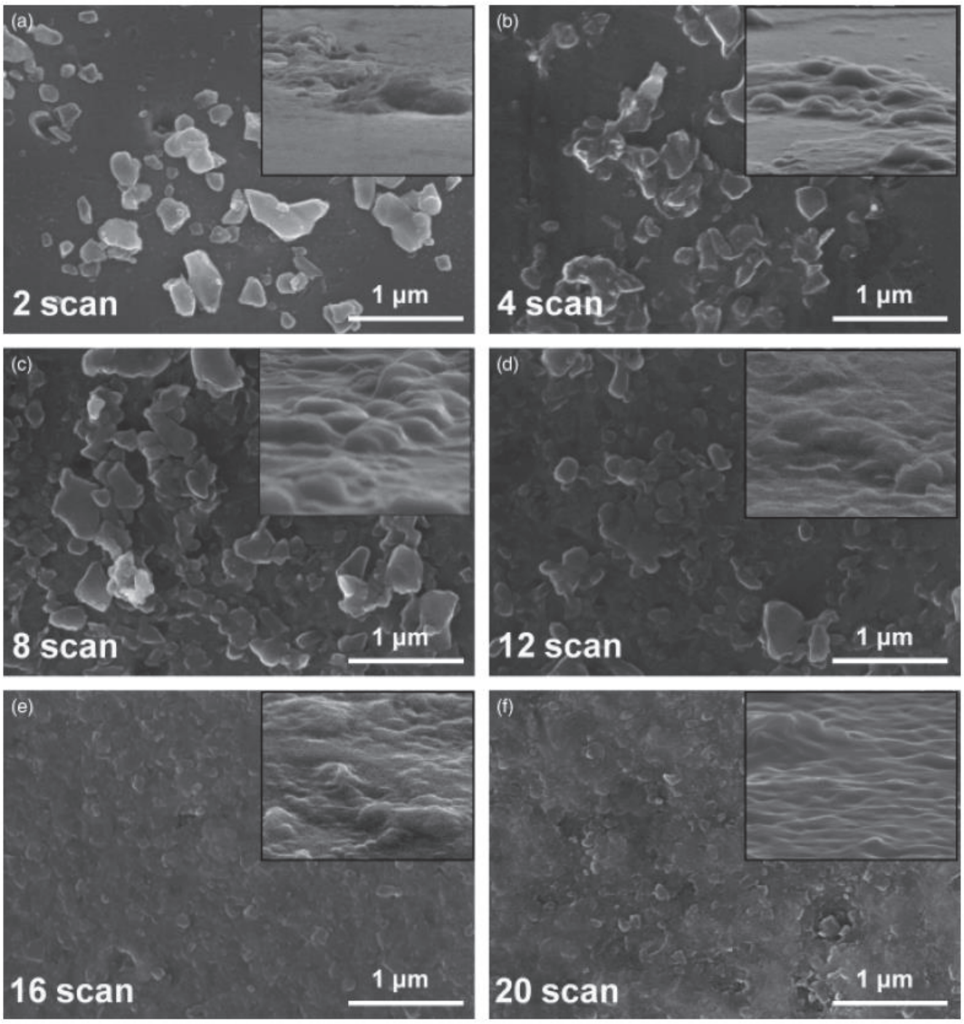

Fig. 2.1.9. SEM images of α-Al_2O_3 AD films deposited on flat Cu substrates with increasing scans [65].

M. Yoshida *et al*. developed a compression test system for a single particle to investigate whether the plastic deformation of the srating powder occurs at RT [66]. Fig. 2.1.10 shows schematic view of the compression test system, SEM images of the α-Al_2O_3 single particle before and after compression and cross-section TEM image of the α-Al_2O_3 single particle after compression [62] [66] [67]. When the particle size was 5 μm, no plastic deformation occurred, and a brittle failure occurred. On the other hand, when the particle size was sub-micron, the plastic deformation occurred once the elastic deformation region was exceeded. These results are in good agreement with the particle size of the starting powder dependence of the AD method shown in Fig. 2.1.8. Furethermore, the pressure calculated based on the particle size was 2 ~ 3 GPa, which was in good agreement with the FEM simulations shown in Fig. 2.1.7. In addition, in the compression test, the compresstion was applied slowly to maintain thermal equilibrium at RT, which means that the plastic deformation occurred at RT. Many additional experiments have been carried out on various brittle materials and it have been thought that when the particle size of the starting powder is sub-micron, under pressure due to particle collisions, the plastic deformation occurs at RT, resulting in a dense, nanometer-scale crystal structure which contains no amorphous phase. A bonding mechanism between the particles and between the particle and substrate has been thought that the formation and acitivation of the nascent surface of the particles by the plastic deformation promotes interparticle bonding even at RT, resulting in the formation of a dense and transparent AD film at RT [59]. However, the mechanism of the AD method is not yet fully understood.

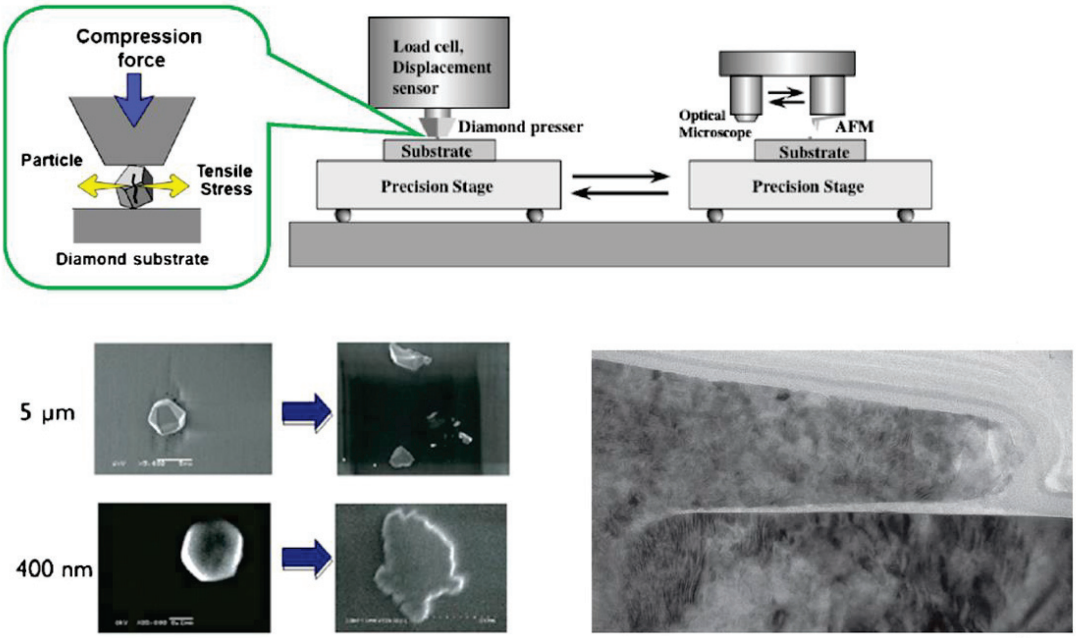

Fig. 2.1.10. Compresstion test for a single particle [62] [66] [67]. Schematic view of the compression test system, SEM images of α-Al_2O_3 single particle before and after compression and Cross-section TEM image of the α-Al_2O_3 single particle after compression.

§2.1.2. Application of AD method

The AD method is widely used in various fields. Here are some examples. TOTO Ltd. has commercialized low-dust-emission semiconductor materials for etching apparatus with yttria thick film coating by the AD method [68]. SEKISUI Chemical Co., Ltd. has commercialzed lightweight and flexible dye-sensitized soler cells by forming a nanoporous thick film of TiO_2 on a resin film by the AD method [69] [70]. Other applications of the AD film are being considered for medical related materials [71] [72], photocatalyst [73] [74], thermoelectric devices [75], solid oxide fuel cells [76] [77], all solid state battery [78], and so on.

J.-J. Park *et al*. prepared nanostructured TiO_2 films by a supersonic AD method and controlled a hydrophilicity of the film by changing the annealing temperature without exposure to UV light [79]. Fig. 2.1.11 shows the relationship between the annealing temperature and contact angle between the film and a water drop. With increasing the annealing temperature, the contact angle become smaller. When the annealing temperature is 500 °C, the contact angle is 0 degree displaying complete wetting. This superhydrophilic TiO_2 film has a potential to use as antifogging and self-cleaning coatings.

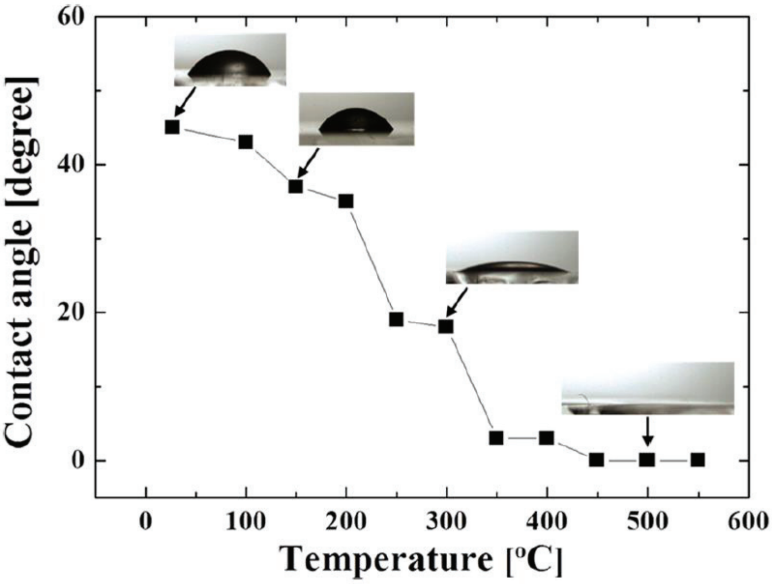

Fig. 2.1.11. Relationship between annealing temperature and contant angle between the film and a water drop for TiO_2 AD film [79].

Ferroelectric AD films have been also studied. Dense $BaTiO_3$ (BT) AD films fabricated on a resin substrate has been investigated for use in low-temperature co-fired ceramic devices [80]. BT AD films have been used as a capacitor for flexible electronics [81]. $Pb(Zr,Ti)O_3$ AD films have been produced for use as a component in a piezoelectric actuator [82] and a MEMS energy harvester [83].

Ceramics films formed by the AD method show enhanced dielectric properties. BT films fabricated by the AD method [84] show a higher permittivity than those fabricated by conventional method [85]. The AD method also enhances dielectric properties of $PbTiO_3$ filims [86], dielectric and electro-optical properties of $(Pb_{0.91},La_{0.09})(Zr_{0.65},Ti_{0.35})O_3$ films [86] [87], and polarization of $(Bi_{0.5}Na_{0.5})TiO_3$ [88] [89]. Oriented AD films have been also formed. T. Miyoshi *et al*. reported that the *c*-axis of PZT AD films deposited on the Pt/TiO_2/yttria-stabilized zirconia substrates was oriented in the normal direction to the film surface by firing at temperature over 1000 °C due to the inplane compressive stress [90]. Suzuki *et al*. formed *c*-axis grain-oriented $SrBi_2Ta_2O_9$ AD films with enhanced polarization properties [91], and recently succeeded to fabricate fairly *c*-axis oriented $Bi_4Ti_3O_{12}$ (BiT) AD films [92] . Fig. 2.1.12 shows a schematic view of the model for the densification mechinisum in the AD method using plate-like particles as the starting powder [92]. In the case of BiT AD films, the plate-like shape of starting powder has been thought to be the cause of the *c*-axis orientation. On the other hand, BiT is known to have a layered crystal structure.

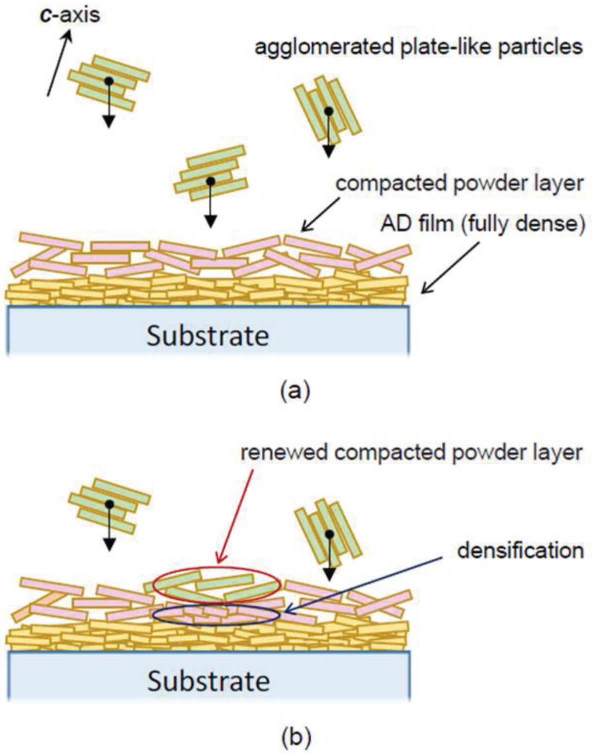

Fig. 2.1.12. Schematic view of the model for the densification mechanism in the AD method using plate-like particles as the starting powder [92].

The crystal structure of BiT is known as a layered structure consisting of alternating bismuth oxide layer and perovskite layer. In the high-temperature (paraelectric) phase, BiT has a tetragonal *I*4/*mmm* structure [93]. BiT undergoes a structural phase transition at 948 K [93]. The crystal structure of BiT in the low-temperature (ferroelectric) phase was reported to be monoclinic *B*1*a*1 from electrical and optical measurements [94] and pricise crystal structure analysis of a single crystal [95]. Recently, there is also the report that the space group is *P*1*a*1 from the single-crystal X-ray diffraction and transmission electron microscopy [96]. However, the crystal structure of BiT can be approximated by orthorhombic *B*2*cb* due to the quite small monoclinic distortion [93] [97] [98]. Fig. 2.1.13 shows the crystal structure of BiT in the low-temperature phase [97]. The spontaneous polarization values of BiT were repoted to be 30 ~ 50 $\mu C/cm^2$ along the *a*-axis and about 5 $\mu C/cm^2$ along the *c*-axis [99] [100]. BiT is expected to be a material for nonvolatile ferroelectric random access memory that does not contain the Pb atom.

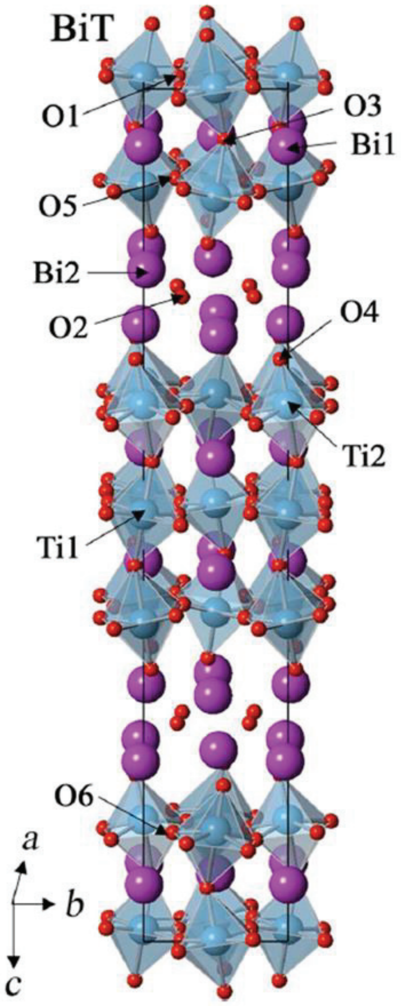

Fig. 2.1.13. Crystal structure of $Bi_4Ti_3O_{12}$ at 300 K [97].

§2.1.3. Purpose

The AD method is a technology to form a ceramic film by mixing ceramic particles with gas and spraying them onto a substrate. There has been much discussion on the mechanism of film formation by the AD method. One of them is that when ceramic particles become smaller than a few microns in size, plastic flow occurs at RT under pressure due to the particle impact, which promotes interparticle bonding by forming and activating the nascent surface of the particles, resulting in the formation of dense and transparent ceramic films at RT [59]. However, the mechanism is still not fully understood.

Recently, M. Suzuki *et al*, have succeeded in fabricating *c*-axis oriented BiT AD films [92]. In the case of BiT AD films, the shape of the starting powder was thought to be the cause of the preferred orientation. However, on the other hand, BiT is known to have a leyered crystal structure. If the mechanism of the AD film formation is related to the formation and activation of nascent surfaces at the time of particle collision, then the origin of the preferred orientation of BiT AD films may be primarily in the crystal structure.

In this study, non-plate-like BiT powder is synthesized as starting powder. The chemical bonding nature of the BiT starting powder and the orientation characteristics of BiT AD film are evaluated by synchrotron radiation X-ray diffraction. The deposition mechanism of the AD method is discussed based on the anisotropy of the chemical bonds in the crystal structure of the starting powder.

Chapter 2.2: Experiment

§2.2.1. Sample preparation

Figure 2.2.1 and 2.2.2 show sample preparation procedure and SEM images of $Bi_4Ti_3O_{12}$ powder grown by the molten salt synthesis at 900 °C and 1100 °C. The BiT powder has plate-like shape. In this study, to obtain the BiT starting powder with non-plate-like shape, the BiT starting powder was synthesized by conventional solid-state reaction method as shown in Fig. 2.2.3. Bi_2O_3 (purity: 99.9999 %, RARE METALIC Co., Ltd.) and TiO_2 (purity: 99.99 %, Kojundo Chemicak Lab. Co., Ltd.) were used as row materials. The row materials were weighted with composition of $Bi_4Ti_3O_{12}$. They were mixed by planetary ball milling for 1 h in ethanol and dried at 80 °C in air. The mixtures were calcined at 800 °C for 2 h in alumina crucibles. To keep the starting powder from getting plate-like shapes as much as possible, the calcined powder was ground by planetary ball milling for 1 h in ethanol, dried at 80 °C in air, and then the starting powder was synthesized at relatively low-temperature 800 °C for 2 h in aluminate crucibles again. Fig. 2.2.4 shows SEM image of BiT starting powder. The SEM observation demonstrated that the non-plate-like particles with sizes from sub μm to several μm were successfully obtained. By using the starting powder, the BiT AD film with a thickness of around 5 μm was deposited on a glass substrate with thickness of 0.5 mm. The aerosol consisting of dried air and the BiT starting powder was sprayed onto the substrate through a nozzle with an orifice of 10 mm × 400 μm size. The nozzle and substrate were 10 mm apart. The pressure of the deposition chamber was kept around 100 Pa during the AD process. Self-supported films were also prepared by peeling the AD films off the substrate. The BiT starting powder and BiT self-supported film were sealed in a quartz capillary with a diameter of 0.1 mm. The BiT samples and SEM images were provided by Dr. Muneyasu Suzuki in AIST.

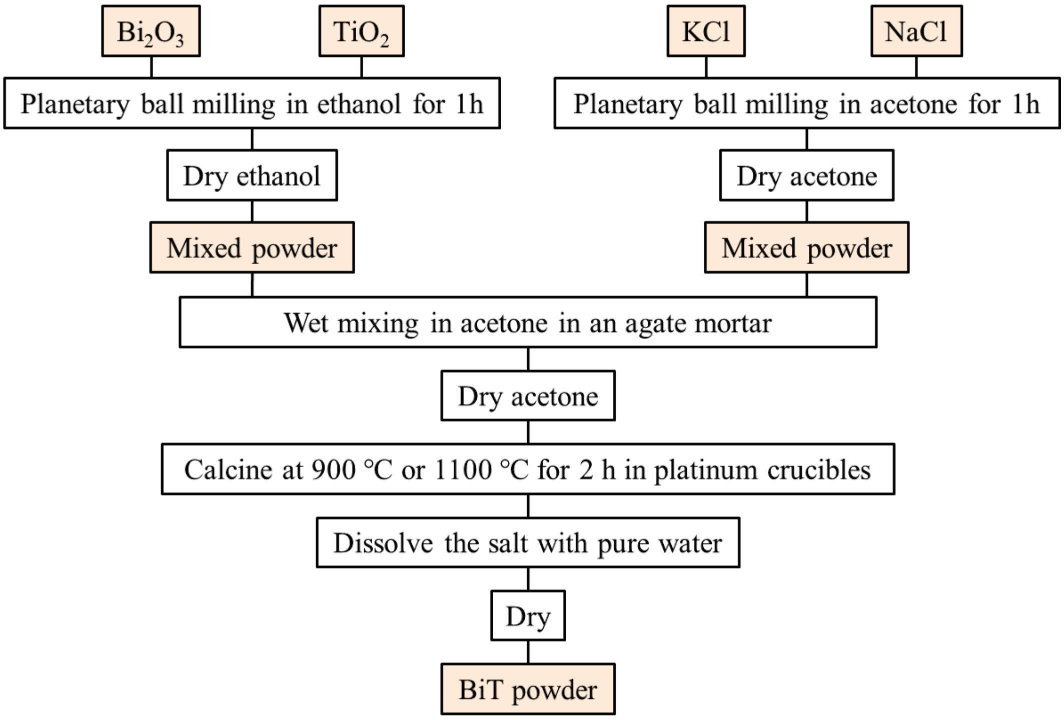

Fig. 2.2.1. Sample preparation procedure of $Bi_4Ti_3O_{12}$ powder by the molten salt synthesis.

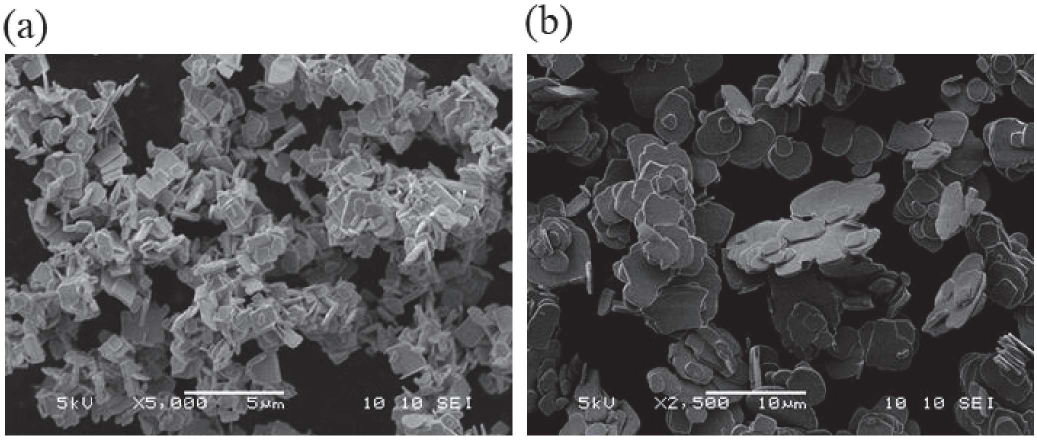

Fig. 2.2.2. SEM image of the $Bi_4Ti_3O_{12}$ powder grown by the molten salt synthesis. Calcined at (a) 900 ℃ and (b) 1100 ℃.

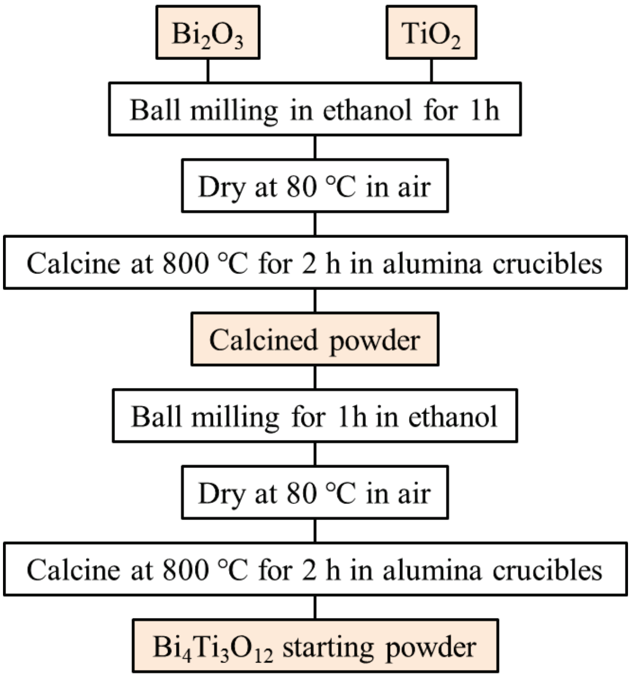

Fig. 2.2.3. Sample preparation procedure of $Bi_4Ti_3O_{12}$ starting powder by the solid-state reaction method.

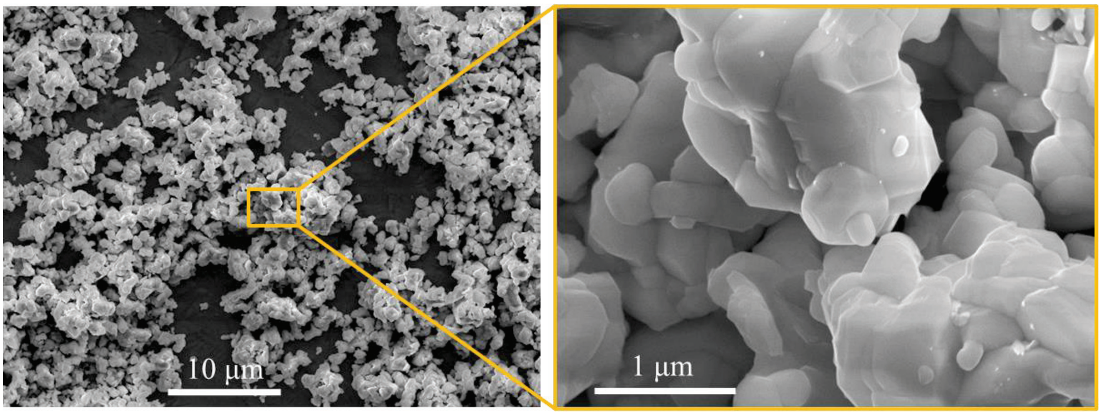

Fig. 2.2.4. SEM image of the $Bi_4Ti_3O_{12}$ starting powder grown by the solid-state reaction method.

§2.2.2. Experimental conditions

Synchrotron radiation X-ray diffraction experiments were performed at the powder diffraction beamline BL02B2 in SPring-8 as in Part 1. Fig. 2.2.5 shows the energy dependence of the linear absorption coefficient of (a) Bi, (b) Ti, and (c) O. High-energy E = 35.0 keV X-rays that can obtain more Bragg reflections and reduce the absorption effect were used for the electron density analysis of the BiT starting powder. The diffraction pattern was measured by the curved IP. While X-rays of 15.9 keV were used to evaluate the characteristics of the BiT AD film. The temperature dependence of the BiT self-supported film was measured using X-rays of 30.0 keV. A flat IP, curved IP and MYTHEN detector were used. Fig. 2.2.6 shows a photograph of the flat IP. The distance between the sample and flat IP was about 300 mm. Unlike the powder sample, the diffraction patterns of the AD film were measured with a reflection geometry instead of the transmition geometry. Fig. 2.2.7 shows a schematic view of the experimental setting for the AD film. First, alignment was carried out so that the sample was parallel to the incident X-rays and the lower half of the incident X-rays was irradiated on the sample. After that, the sample was tilted by 1° and the diffraction patterns were measured. The diffraction patterns of the starting powder were also measured by the flat IP as a reference. The details of the experimental conditions are shown in Table 2.2.1.

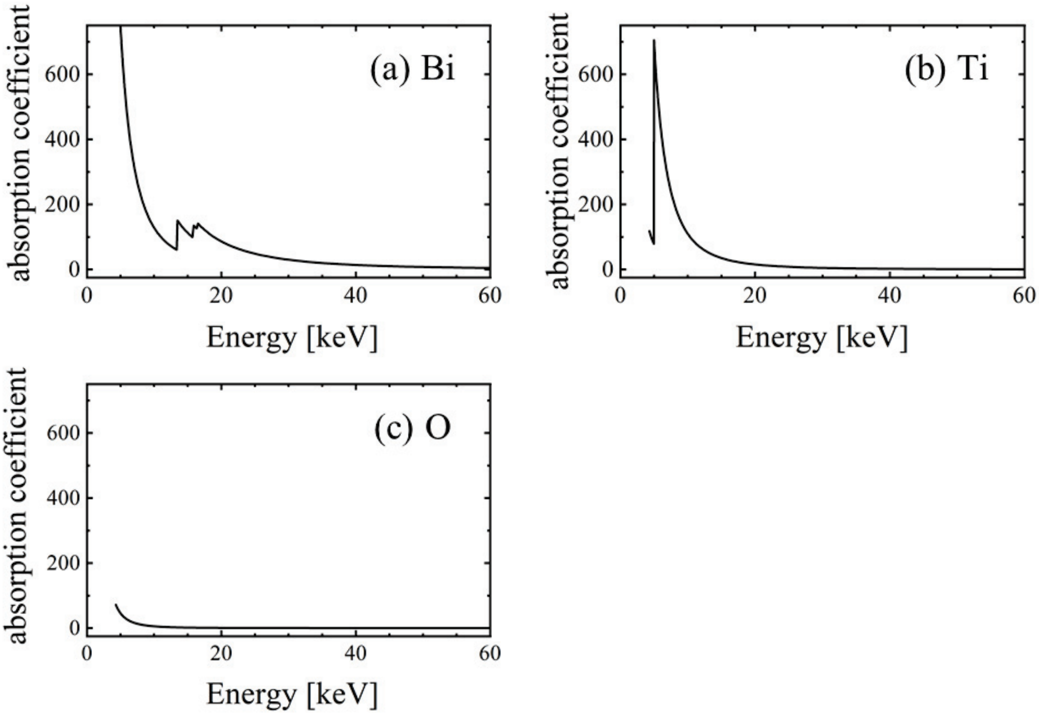

Fig. 2.2.5. Energy dependence of the absorption coefficient for (a) Bi, (b) Ti, and (c) O.

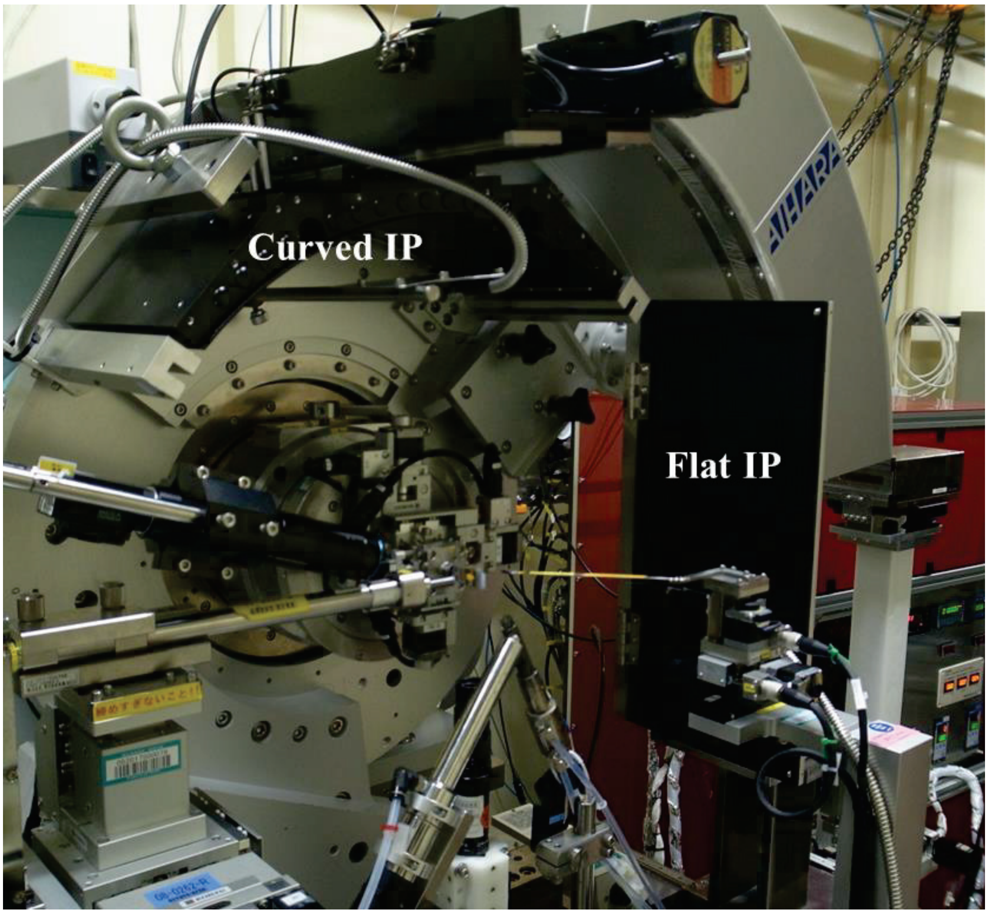

Fig. 2.2.6. Photograpg of the Flat IP.

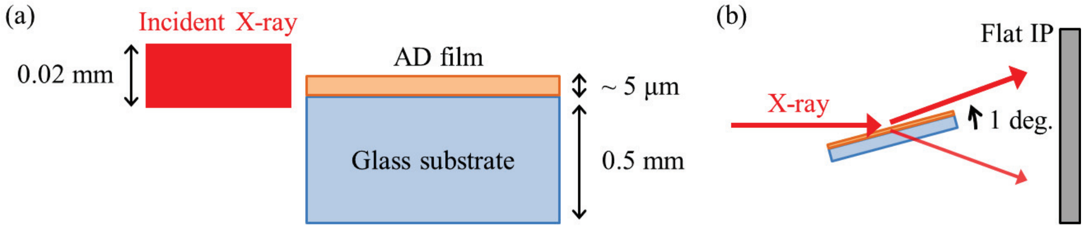

Fig. 2.2.7. Scematic view of the experimental setting for the AD film.

Table 2.2.1. Experimental conditions of the $Bi_4Ti_3O_{12}$ starting powder, AD film, and self-supported film.

Sample type	Wavelength [Å]	Temperature [K]	Measurement time [min]	Collimator [mm × mm]	Detector
Starting powder	0.354818(1)	RT	20	0.5 × 0.2	Curved IP
		1100	23	0.5 × 0.2	Curved IP
	0.779239(1)	RT	5	0.5 × 0.1	Flat IP
			5		Curved IP
		1100	5		FLAT IP
			5		Curved IP
	0.413034(1)	300 ~ 1100, 1100 ~ 300 (Rate = 20 K/min, ΔT = 5 K, 1 cycle)	14 sec / 1 data	0.5 × 0.2	MYTHEN
AD film	0.779239(1)	RT	5	0.02 × 0.1	Flat IP
			5		Curved IP
		1100	5		FLAT IP
			5		Curved IP
Self-supported film	0.413034(1)	300 ~ 1100, 1100 ~ 300 (Rate = 20 K/min, ΔT = 5 K, 2 cycle)	14 sec / 1 data	0.5 × 0.2	MYTHEN

Chapter 2.3: Analysis

The analysis methods are the same as in Part 1. Fig. 2.3.1 shows the diffraction angle dependence of the atomic scattering factors of Bi, Ti and O when using X-rays of 35 keV. Here, ion species Bi, Bi^{3+}, Ti, Ti^{2+}, Ti^{4+}, O and O^{1-} described in the International Tables for Crystallography C [41] are plotted.

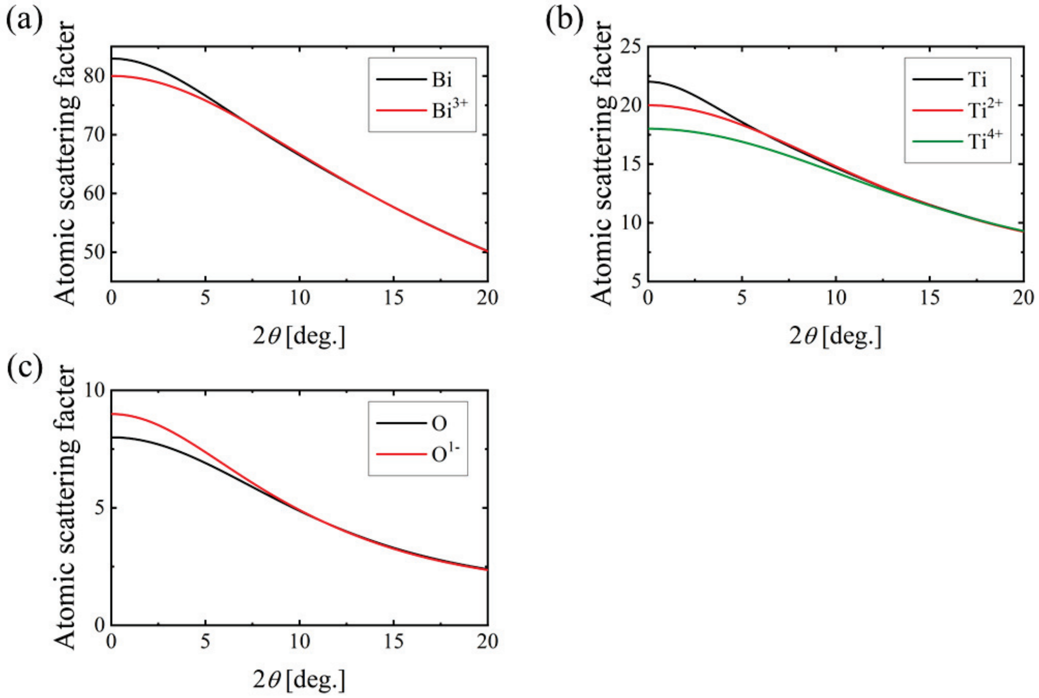

Fig. 2.3.1. Diffraction angle dependence of the scattering factor. (a) Bi, (b) Ti and O when using X-rays of 35 keV.

Chapter 2.4: Results and discussion

§2.4.1. Chemical bonding nature of the $Bi_4Ti_3O_{12}$ starting powder

First, the crystal structure analysis of the $Bi_4Ti_3O_{12}$ starting powder at 1100 K in the paraelectric phase was performed to confirm that the sample was certainly synthesized. Fig. 2.4.1 shows the Debye–Sherrer pattern of the BiT starting powder at 1100 K (paraelectric phase) recorded on the curved IP. The darker blacks indicate higher diffraction intensities. The intensities of the diffraction image were integrated with a width of 2.5 mm (51 pixel) with respect to the diffraction angle 2θ to create one-dimensional (1D) diffraction data.

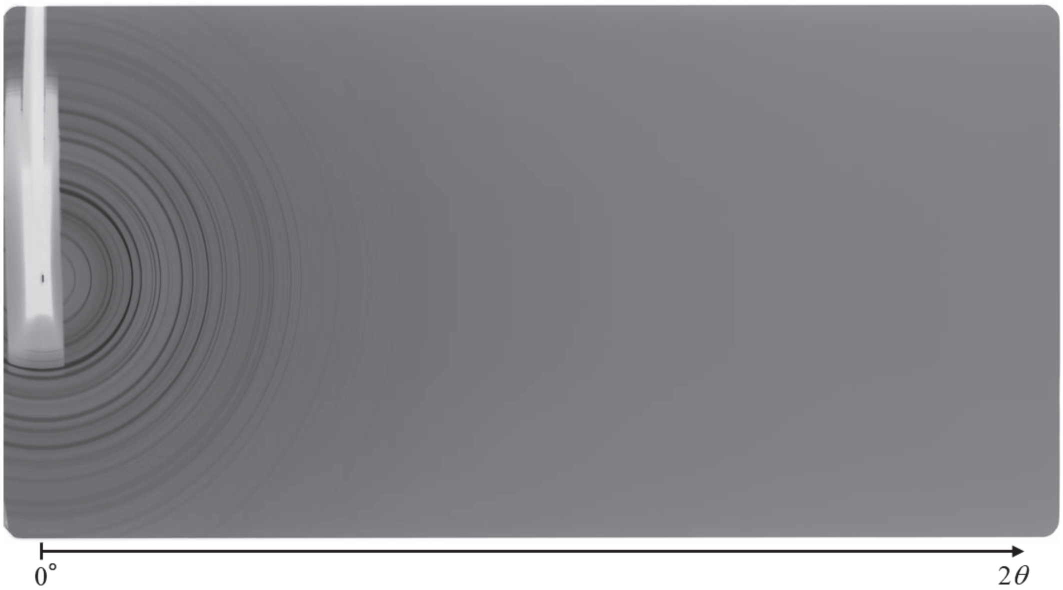

Fig. 2.4.1. Debye–Sherrer rings of the $Bi_4Ti_3O_{12}$ starting powder at 1100 K (paraelectric phase) recorded on the curved imaging plate.

Figure 2.4.2 shows Rietveld profile fitting result of the BiT starting powder at 1100 K. The analysis range was $2° \leq 2\theta \leq 40°$ ($d > 0.52$ Å). The final structure model is based on the application of a neutral atom model to the atomic scattering factors and an anisotropic model to the thermal vibration parameters of each atom. The coordinates and thermal vibration parameters of each atom were analyzed using data in the angular range of 15° $\leq 2\theta \leq$ 40°, where the atomic scattering factor is independent of ionic valence. The reliability factors are R_{wp} = 2.27%, R_{I} = 4.23% and R_{F} = 5.69%, respectively. Table 2.4.1 and Fig. 2.4.3 show the determined crystal structure parameters and ball-and-stick model of the crystal structure, respectively. The determined crystal structure agrees well with that determined in the previous study [93]. It was confirmed that BiT crystals were successfully synthesized even in the non-plate-like powder prepared in this study.

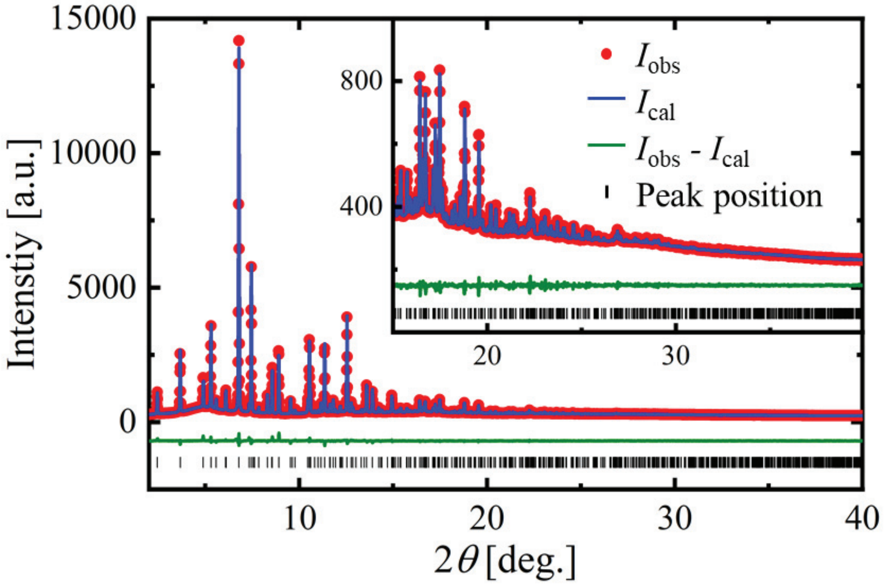

Fig. 2.4.2. Rietveld profile fitting result of the $Bi_4Ti_3O_{12}$ starting powder at 1100 K (paraelectric phase, space group: *I*4/*mmm*). The red dot, blue line, green line, and | represent the observed intensity, calculated intensity, residual from I_{obs} minus I_{cal}, and peak position, respectively. The analysis range is $d > 0.52$ Å ($2\theta < 40°$). The reliability factors are R_{wp} = 2.27%, R_{I} = 4.23% and R_{F} = 5.69%, respectively.

Table 2.4.1. Crystal structural parameters of the $Bi_4Ti_3O_{12}$ starting powder at 1100 K (paraelectric phase, space group: *I*4/*mmm*). Lattice parameters: $a = b = 3.8571(2)$ Å, $c = 33.243(1)$ Å, and $\alpha = \beta = \gamma = 90°$ for data with $d > 0.52$ Å.

Atom	x	y	z	U_{11} [Å^2]	U_{22} [Å^2]	U_{33} [Å^2]
Bi1	0.5	0.5	0.06787(5)	0.056(1)	$= U_{11}$	0.05.9(2)
Bi2	0.5	0.5	0.21165(4)	0.045(1)	$= U_{11}$	0.03.1(1)
Ti1	0.5	0.5	0.5	0.015(4)	$= U_{11}$	0.009(5)
Ti2	0.5	0.5	0.37097(9)	0.023(3)	$= U_{11}$	0.008(4)
O1	0.5	0	0	0.05(2)	0.14(5)	0.08(4)
O2	0.5	0	0.25	0.03(1)	$= U_{11}$	0.02(1)
O3	0.5	0.5	0.4414(5)	0.09(2)	$= U_{11}$	0.01(2)
O4	0.5	0.5	0.3197(6)	0.13(3)	$= U_{11}$	0.01(2)
O5	0.5	0	0.1155(7)	0.037(9)	0.06(2)	0.07(2)

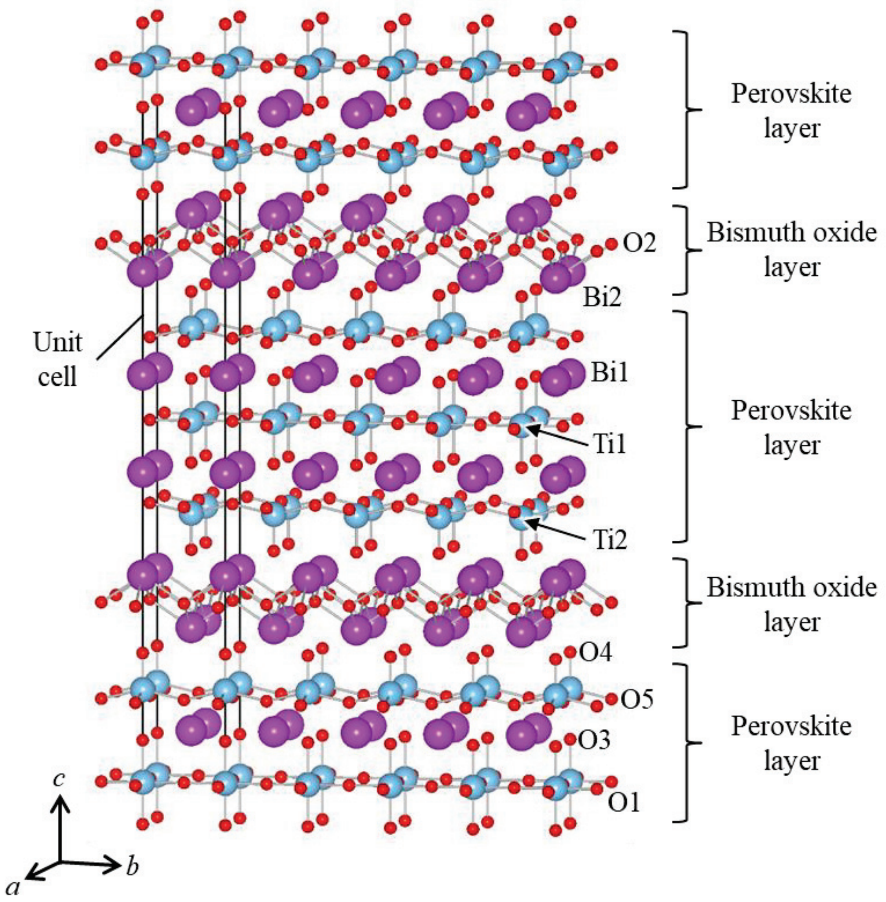

Fig. 2.4.3. Ball-and-stick model of the $Bi_4Ti_3O_{12}$ starting powder at 1100 K (paraelectric phase, space group: *I*4/*mmm*).

By the Rietveld analysis, 647 measured structure factors F_{obs} in the range of $d > 0.52$ Å were extractd. The weight for the MEM electron density analysis was considered. Fig. 2.4.4 shows the diffraction angle 2θ dependence of the standardized residuals $(|F_{\mathrm{obs}}| - |F_{\mathrm{MEM}}|) / \sigma_{\mathrm{obs}}$ and the histogram of the standardized residuals $(|F_{\mathrm{obs}}| - |F_{\mathrm{MEM}}|) / \sigma_{\mathrm{obs}}$ obtained as a result of the MEM electron density analysis. The normal distribution function with standard deviation $\sigma = 1$ is indicated by the black line in the figure of the histogram. The histogram should fit well with the normal distribution function if the MEM analysis is ideally performed. Fig. 2.4.4 (a) shows the results of the MEM analysis without considering the weight. In the left figure, the discrepancy is noticeable on the low-angle side, and the histogram in the right figure has a sharp distribution which does not match the normal distribution function. Fig. 2.4.4 (b) shows the results after considering the weight of $n = 1$. In the left figure, the discrepancy on the low-angle side is reduced and the variability is no longer strongly dependent on 2θ. The histogram in the right figure approaches the normal distribution function. $n = 1$ was adopted as the value of the weight, and the electron density distribution analyzed with the weight of $n = 1$ was used as the result.

For the paraelectric phase of the BiT starting powder, the unit cell was divided into 78 × 78 × 666 units and the total density distribution was obtained. One side of one voxel corresponds to about 0.05 Å. Fig. 2.4.5 shows the total electron density distribution of BiT starting powder at 1100 K. Fig. 2.4.5 (a) shows the three-dimensional (3D) electron density distribution for one unit cell. The face drawn in yellow is an iso-electron density surface of $0.5e$ Å^{-3}, that is, the shape of an electron cloud with the electron density of $0.5e$ Å^{-3}. Fig. 2.4.5 (b) and (c) show two-dimensional (2D) electron density distributions for the (100) and (200) planes, respectively. The contour lines are drawn in $0.5e$ Å^{-3} steps, ranging from $0.5e$ Å^{-3} to $3.0e$ Å^{-3}. In Fig. 2.4.5 (a), there is an overlap of electron clouds between Bi2 and O2, which means that the Bi2-O2 bond is covalent. On the other hand, there is no overlap of electron clouds between Bi1 and O atoms which means that the Bi1-O bonds are ionic. The overlap of the electron clouds between the O atoms located perpendicular to the *c*-axis is common in Ti1 and Ti2. Ti1 has an electron clouds overlap between both the upper and lower O atoms, while Ti2 has only an overlap of the electron cloud between the upper or lower O atom. In other words, Ti1 has a six-fold coordination, while Ti2 has a five-fold coordination. These features can be easily seen in the 2D electron density distribution (Fig. 2.4.5 (b) and (c)). Networks of covalent bonds are formed in the direction perpendicular to the *c*-axis, and there is no overlap of electron clouds between each network. This result indicates that the BiT starting powder has a layered crystal structure with layers stacked along the *c*-axis in the paraelectric phase.

(a) Without weight ($n = 0$)

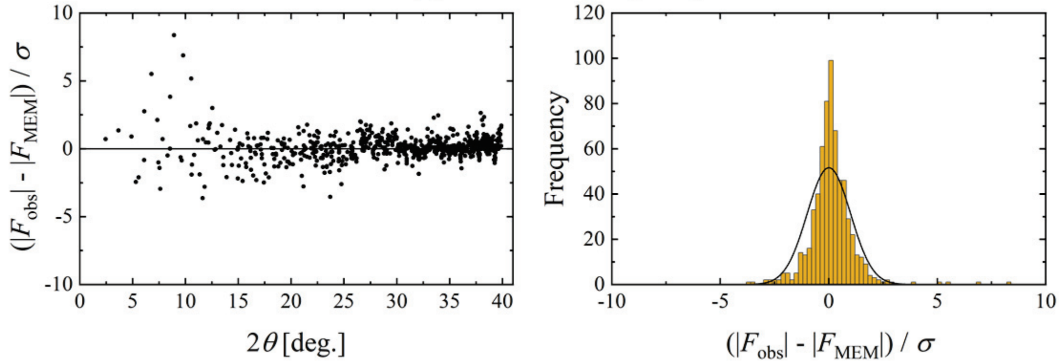

(b) With weight ($n = 1$)

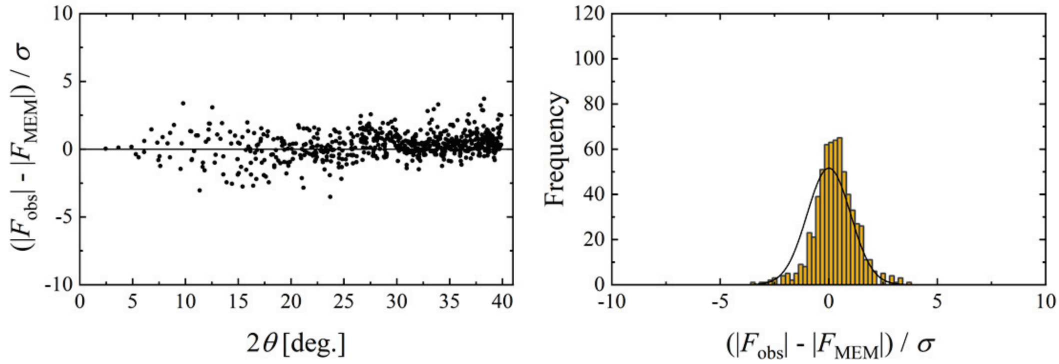

Fig. 2.4.4. Consideration of the weight for the MEM analysis of the $Bi_4Ti_3O_{12}$ starting powder at 1100 K (paraelectric phase). The left figure and right figure show the standardized residuals $(|F_{obs}| - |F_{MEM}|) / \sigma_{obs}$ as a function of diffraction angle 2θ and the histogram of the standardized residuals $(|F_{obs}| - |F_{MEM}|) / \sigma_{obs}$, respectively. The histogram ideally follows a normal distribution function with standard deviation $\sigma = 1$, wrriten as a black line. (a) Without weight. (b) With weight. The number of structure factors F_{obs} is 647.

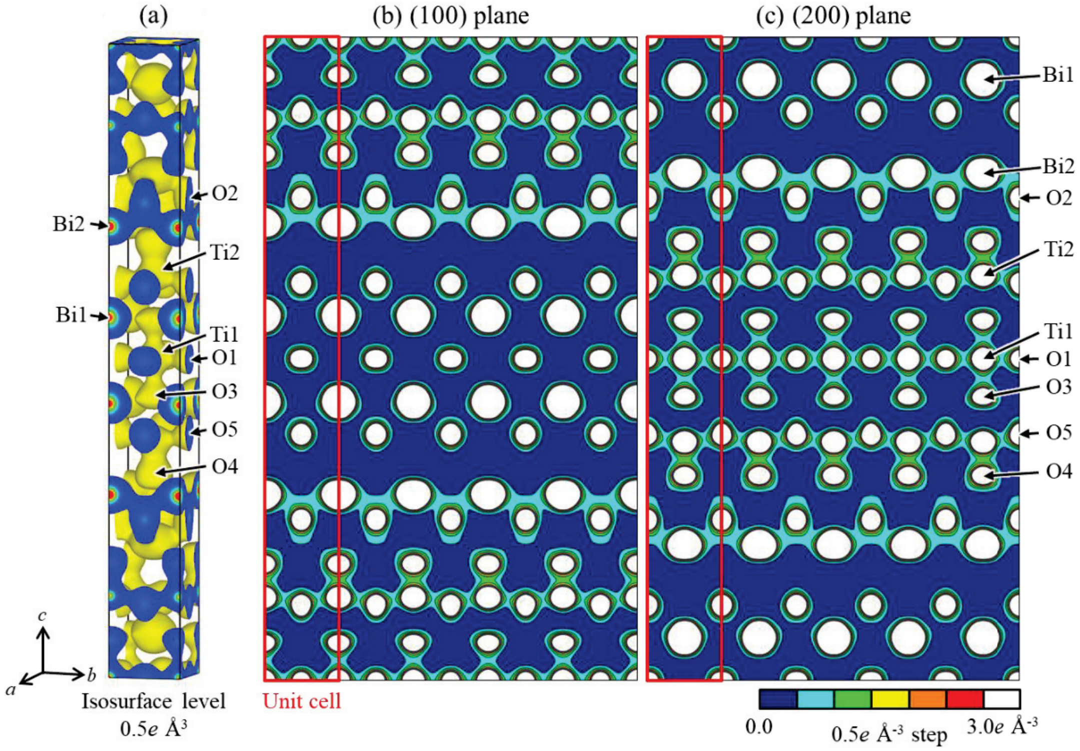

Fig. 2.4.5. Total electron density distribution of the $Bi_4Ti_3O_{12}$ starting powder at 1100 K (paraelectric phse, space group: *I*4/*mmm*). (a) Three-dimensional electron density distribution for one unit cell. The isosurface level is 0.5*e* Å^{-3}. Two-dimensional electron density distribution for the (b) (100) and (c) (200) planes. The contour lines are drawn in 0.5*e* Å^{-3} steps, ranging from 0.5*e* Å^{-3} to 3.0*e* Å^{-3}.

Rietveld analysis of the BiT starting powder at 1100 K confirmed that BiT was properly synthesized. However, the deposition in the AD method takes place at RT. The MEM/Rietveld analysis for the RT data was also performed in the same way.

Figure 2.4.6 shows the Debye–Sherrer pattern of the BiT starting powder at RT (ferroelectric phase) recorded on the curved IP. The intensities of the diffraction image were integrated with a width of 2.5 mm (51 pixel) with respect to the diffraction angle 2θ to create 1D diffraction data.

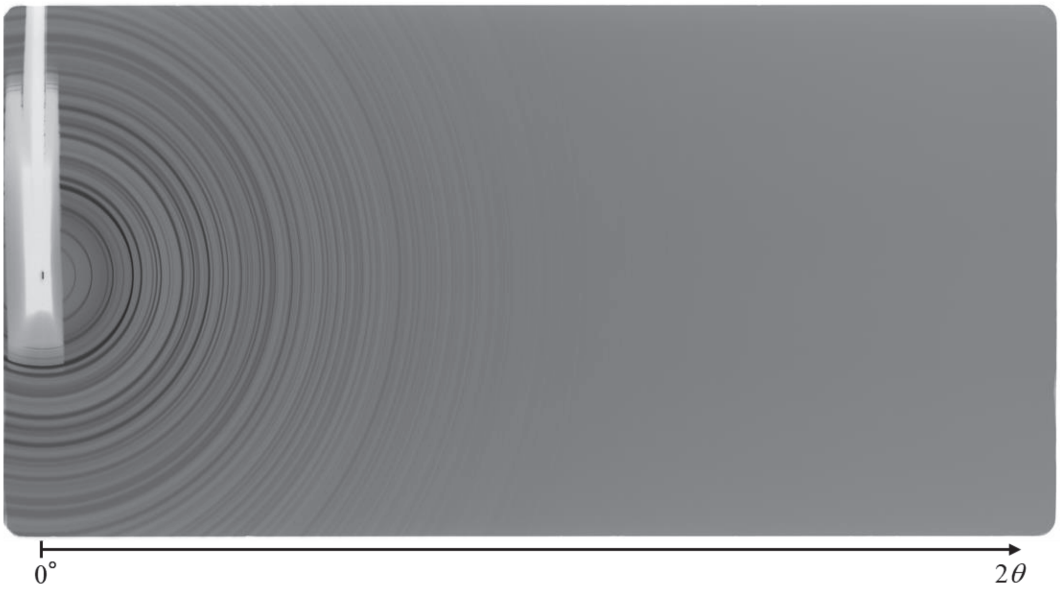

Fig. 2.4.6. Debye–Sherrer rings of the $Bi_4Ti_3O_{12}$ starting powder at RT (ferroelectric phase) recorded on the curved imaging plate.

Figure 2.4.7, Table 2.4.2, and Fig. 2.4.8 show the Rietveld profile fitting result, determined crystal structure parameters, and ball-and-stick model of crystal structure of the BiT starting powder at RT. As shown in §2.1.2, the space group of BiT in the ferroelectric phase has been reported to be $B1a1$ and $P1a1$, however, because they can be approximated by $B2cb$, the Rietveld analysis was performed by assuming the space group of BiT as $B2cb$. The analysis range was $2° \leq 2\theta \leq 52°$ ($d > 0.39$ Å). The final structure model is based on the application of a neutral atom model to the atomic scattering factors and an isotropic model to the thermal vibration parameters of each atom. The coordinates and thermal vibration parameters of each atom were analyzed using data in the angular range of $15.2° \leq 2\theta \leq 52°$, where the atomic scattering factor is independent of ionic valence. The reliability factors are $R_{wp} = 2.30\%$, $R_I = 3.28\%$ and $R_F = 2.15\%$, respectively. The a-axis in the paraelectric phase corresponds to the (110) direction in the ferroelectric phase. In the ferroelectric phase, there are rotation and deformation of the oxygen octahedron.

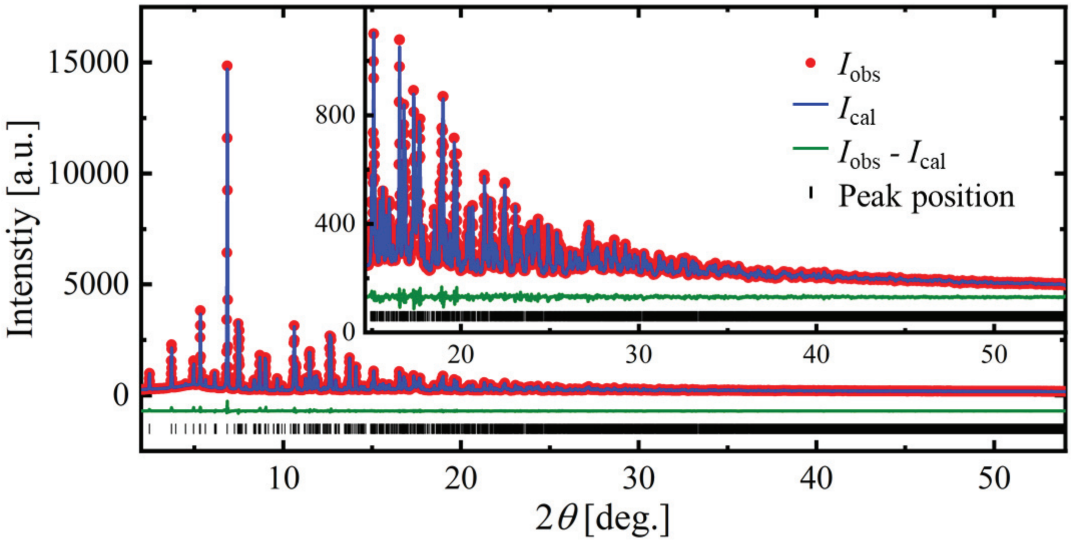

Fig. 2.4.7. Rietveld profile fitting result of the $Bi_4Ti_3O_{12}$ starting powder at RT (ferroelectric phase, space group: *B*2*cb*). The red dot, blue line, green line, and | represent the observed intensity, calculated intensity, residual from I_{obs} minus I_{cal}, and peak position, respectively. The analysis range is $d > 0.39$ Å ($2\theta < 52°$). The reliability factors are $R_{wp} = 2.30\%$, $R_I = 3.28\%$ and $R_F = 2.15\%$, respectively.

Table 2.4.2. Crystal structural parameters of $Bi_4Ti_3O_{12}$ starting powder at RT (ferroelectric phase, space group: *B*2*cb*). Lattice parameters: $a = 5.4426(1)$, $b = 5.4039(1)$ Å, $c = 32.7913(7)$ Å, and $\alpha = \beta = \gamma = 90°$ for data with $d > 0.39$ Å.

Atom	x	y	z	U_{iso} [10^{-2} Å^2]
Bi1	0	0.9979(2)	0.06679(1)	0.638(9)
Bi2	0.9942(4)	0.0202(1)	0.21138(1)	0.648(8)
Ti1	0.0455(8)	0	0.5	0.28(6)
Ti2	0.0458(5)	1.004(1)	0.37154(7)	0.36(4)
O1	0.324(3)	0.258(3)	0.0068(5)	1.7(4)
O2	0.215(3)	0.235(5)	0.2491(9)	0.3(2)
O3	0.074(3)	1.056(3)	0.4423(5)	0.17(4)
O4	1.050(4)	0.936(3)	0.3234(6)	2.1(4)
O5	0.280(4)	0.213(3)	0.1119(5)	0.2(2)
O6	0.145(4)	0.201(4)	0.8762(6)	0.9(3)

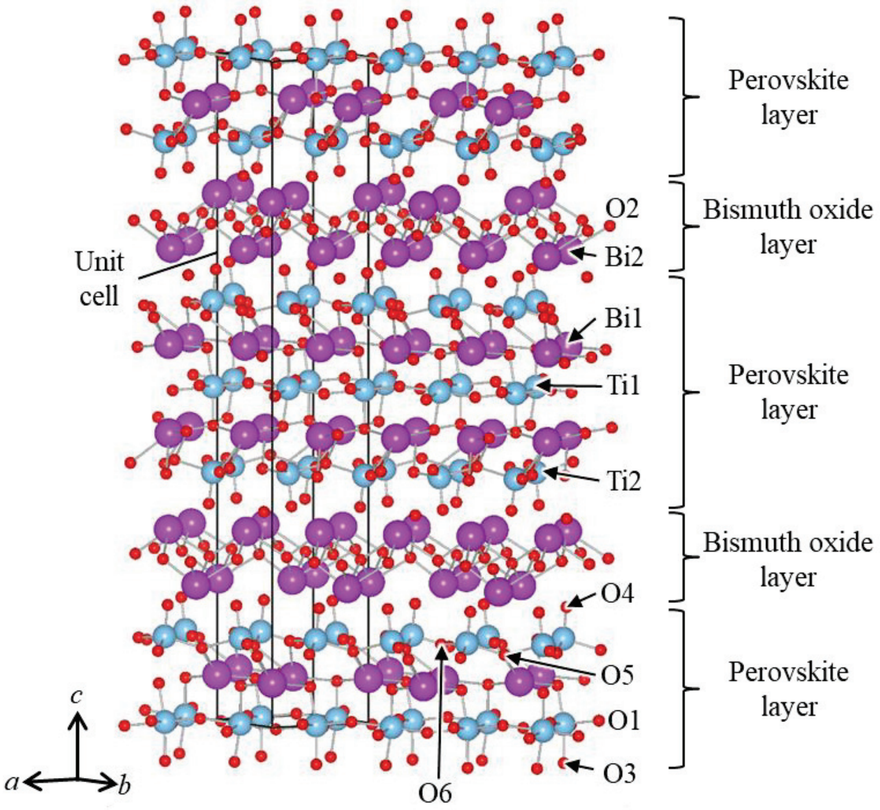

Fig. 2.4.8. Ball-and-stick model of the $Bi_4Ti_3O_{12}$ starting powder at RT (ferroelectric phase, space group: *B*2*cb*).

By the Rietveld analysis, 4464 measured structure factors F_{obs} in the range $d > 0.39$ Å were extractd. The weight for the MEM electron density analysis was considered. Fig. 2.4.9 shows the diffraction angle 2θ dependence of the standardized residuals $(|F_{\mathrm{obs}}| - |F_{\mathrm{MEM}}|) / \sigma_{\mathrm{obs}}$ and the histogram of the standardized residuals $(|F_{\mathrm{obs}}| - |F_{\mathrm{MEM}}|) / \sigma_{\mathrm{obs}}$ obtained as a result of the MEM electron density analysis. The normal distribution function with standard deviation $\sigma = 1$ is indicated by the black line in the figure of the histogram. Fig. 2.4.9 (a) shows the results of the MEM analysis without considering the weight. In the left figure, the discrepancy is noticeable on the low-angle side, and the histogram in the right figure has an extremely sharp distribution which does not match the normal distribution function. Fig. 2.4.9 (b) shows the results after considering the weight of $n = 1$. In the left figure, the discrepancy on the low-angle side is reduced and the variability is no longer strongly dependent on 2θ. The histogram in the right figure approaches the normal distribution function. $n = 1$ was adopted as the value of the weight, and the electron density distribution analyzed with the weight of n = 1 was used as the result.

(a) Without weight (n = 0)

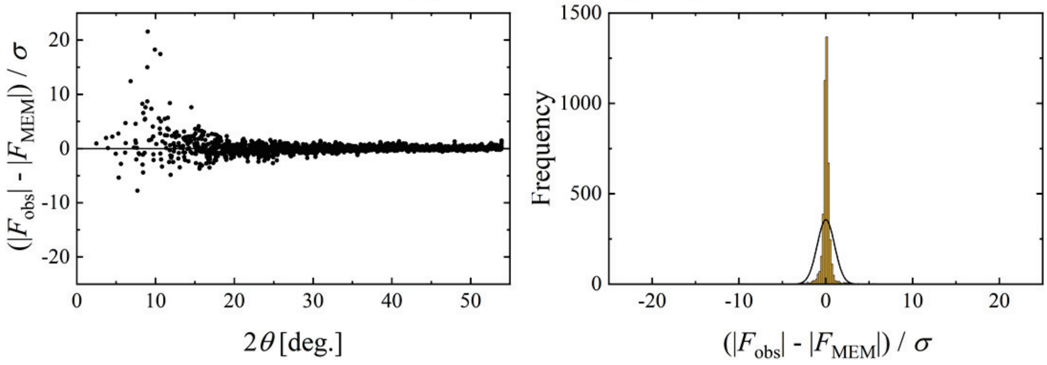

(b) With weight (n = 1)

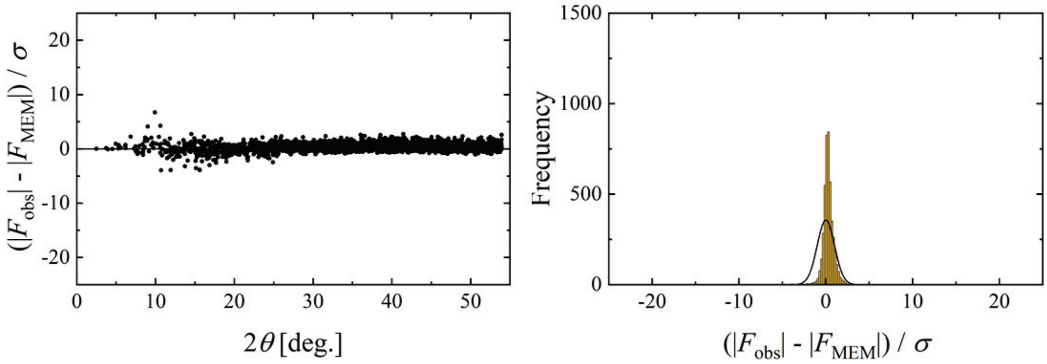

Fig. 2.4.9. Consideration of the weight for the MEM analysis of the $Bi_4Ti_3O_{12}$ starting powder at RT (ferroelectric phase). The left figure and right figure show the standardized residuals $(|F_{\mathrm{obs}}| - |F_{\mathrm{MEM}}|) / \sigma_{\mathrm{obs}}$ as a function of diffraction angle 2θ and the histogram of the standardized residuals $(|F_{\mathrm{obs}}| - |F_{\mathrm{MEM}}|) / \sigma_{\mathrm{obs}}$, respectively. The histogram ideally follows a normal distribution function with standard deviation $\sigma = 1$, wrriten as a black line. (a) Without weight. (b) With weight. The number of structure factors F_{obs} is 4464.

For the ferroelectric phase of the BiT starting powder, the unit cell was divided into 108 × 108 × 654 units and the total density distribution was obtained. One side of one voxel corresponds to about 0.05 Å. Fig. 2.4.10 shows the total electron density distribution of BiT starting powder at RT. Fig. 2.4.10 (a) shows the 3D electron density distribution for one unit cell. The face drawn in yellow is an iso-electron density surface of 0.5e Å^{-3}. Fig. 2.4.10 (b) and (c) show 2D electron density distributions for the (220) and (110) planes, respectively. The contour lines are drawn in 0.5e Å^{-3} steps, ranging from

0.5*e* Å^{-3} to 3.0*e* Å^{-3}. The electron density distribution of the BiT starting powder in the ferroelectric phase looks slightly different from that in the paraelectric phase. An overlap of electron clouds between Bi1 and O is observed. Ti2 has a four-fold coordination. Despite these differences, BiT in the ferroelectric phase has a similar layered structure as in the paraelectric phase.

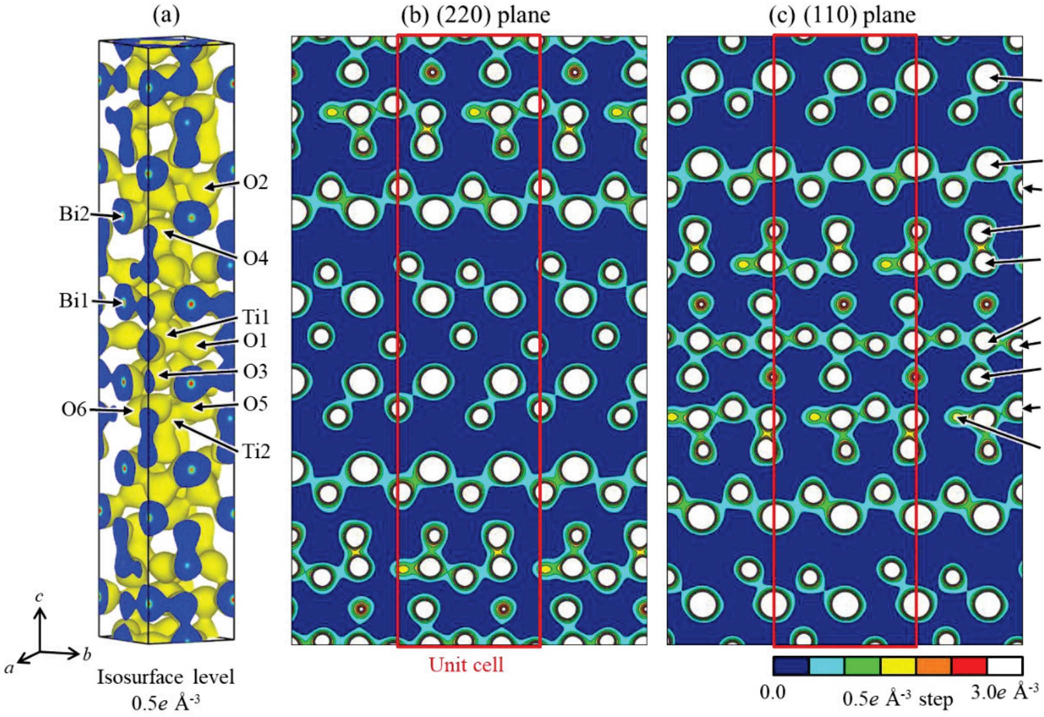

Fig. 2.4.10. Total electron density distribution of the $Bi_4Ti_3O_{12}$ starting powder at RT (ferroelectric phase, space group: *B*2*cb*). (a) Three-dimensional electron density distribution for one unit cell. The isosurface level is 0.5*e* Å^{-3}. Two-dimensional electron density distribution for the (b) (220) and (c) (110) planes. The contour lines are drawn in 0.5*e* Å^{-3} steps, ranging from 0.5*e* Å^{-3} to 3.0*e* Å^{-3}.

From above results, it has been found that the BiT starting powder has essentially a layered crystal structure in both ferroelectric phase and paraelectric phase.

§2.4.2. Orientation characteristics of the $Bi_4Ti_3O_{12}$ AD film

Figure 2.4.11 shows the temperature dependence of the Debye−Sherrer rings of the BiT AD film and starting powder recorded on the flat IP. Fig. 2.4.11 (b) is enlarged views of the range indicated by the square in Fig. 2.4.11 (a). The arrow at the top of the figure shows the thermal history, and the measurements were performed at RT (as-deposited state), 1100 K and RT (after heiting). In the X-ray diffraction experiments, concentric Debye−Sherrer rings are obtained when a flat 2D detector is used, as shown in Fig. 2.4.11 (a). In the case of the powder sample, the intensity distribution on the Debye−Sherrer ring is uniform. The uniformity of the intensity distribution can be used to check whether the material is preferentially oriented or not. Since a number of Debye−Sherrer rings were observed for the AD film, it was found that polycrystalline films were basically formed in the AD method instead of single crystal films. In Fig. 2.4.11 (b), however, the intensity distribution of the (00*l*) peaks of the BiT AD film at RT (as-deposited state) is not uniform on the Debye−Sherrer ring. The intensity in the direction perpendicular to the file surface is stronger than that in the in-plane direction. This result demonstrates that the *c*-axis is aligned in the perpendicular direction in the BiT AD film, that is, the BiT AD film is oriented in the *c*-axis. The non-uniformity of the intensity distribution of the (00*l*) peaks of the BiT AD film did not change even at 1100 K and RT after heating, and it was found that the *c*-axis orientation of the BiT AD film was not relaxed. T. Miyoshi *et al*. reported the *c*-axis orientation of $Pb(Zr,Ti)O_3$ AD films on Pt/TiO_2/yttria-stabilized zirconia substrates due to the in-plane compressive stress by heating avobe 1000°C. In the case of BiT, it was revealed in this study that not only after heating but also in the as-deposited state, the BiT AD film is *c*-axis oriented.

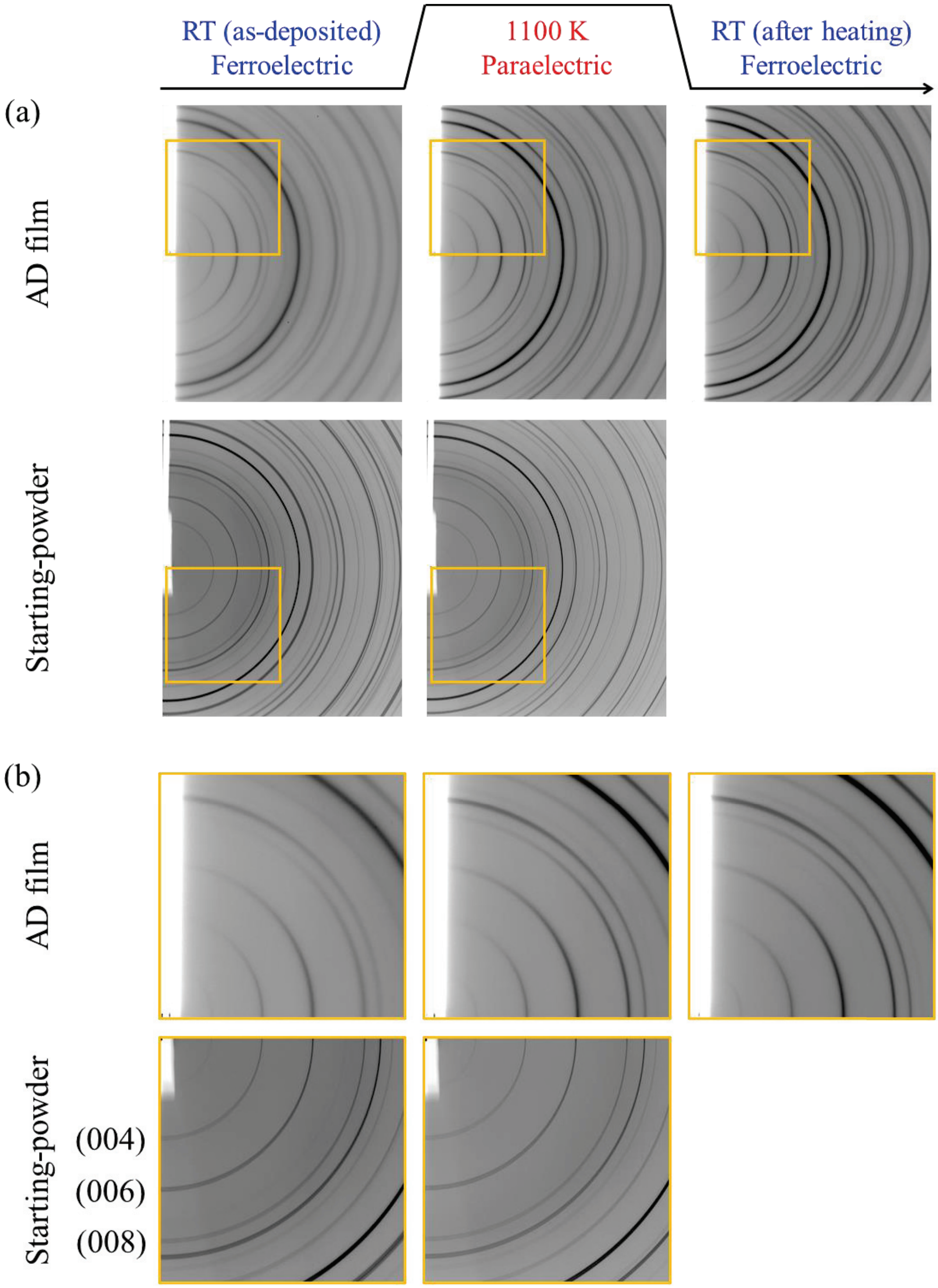

Fig. 2.4.11. Temperature dependence of the Debye–Sherrer rings of the $Bi_4Ti_3O_{12}$ AD film and starting powder recorded on the flat imaging plate at RT (as-deopsited state), 1100 K and RT (after heating). (b) is an enlarged view of the area indicated by the square in (a). The arrow at the top of the figure shows the thermal history.

Figure 2.4.12 shows the 1D diffraction patterns of the (a) BiT AD film and (b) BiT starting powder in the perpendicular direction corresponding to Fig. 2.4.11. Fig. 2.4.13 shows the Rietveld fitting result of the AD film at RT (as-deposited state). The Rietveld analysis was performed using the space group of *B*2*cb*. In Fig. 2.4.12, the intensity ratio of the (00*l*) peaks of the BiT AD film is larger than that of the BiT starting powder. In Fig. 2.4.13, the observed intensities of the (00*l*) peaks are considerably larger than the calculated intensities of the (00*l*) peaks. These results also show that the BiT AD film is *c*-axis oriented. The diffraction peaks of the BiT AD film became sharper as the temperature was raised. This could be due to the grain growth and reduction of defects due to the temperature rise.

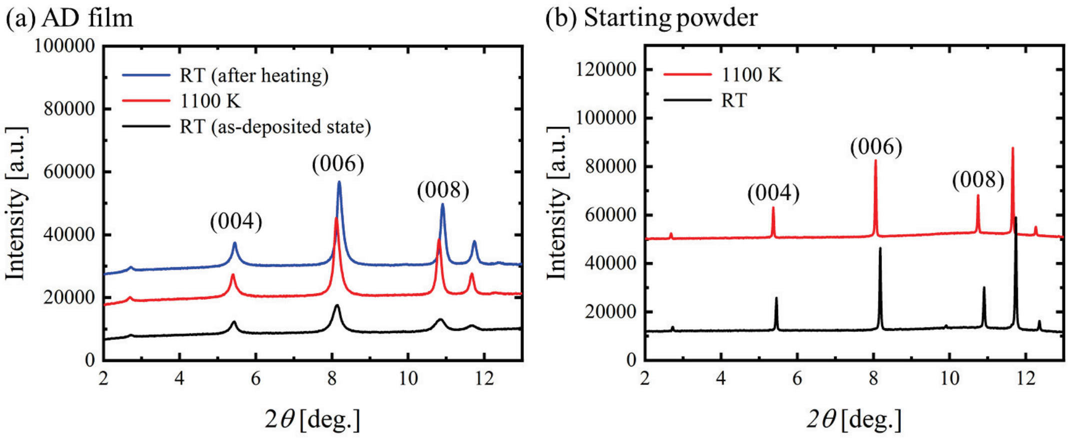

Fig. 2.4.12. Temperature dependence of the 1D diffraction patterns of the $Bi_4Ti_3O_{12}$ (a) AD film and (b) starting powder in the perpendicular direction at RT (as-deposited state), 1100 K and RT (after hearting).

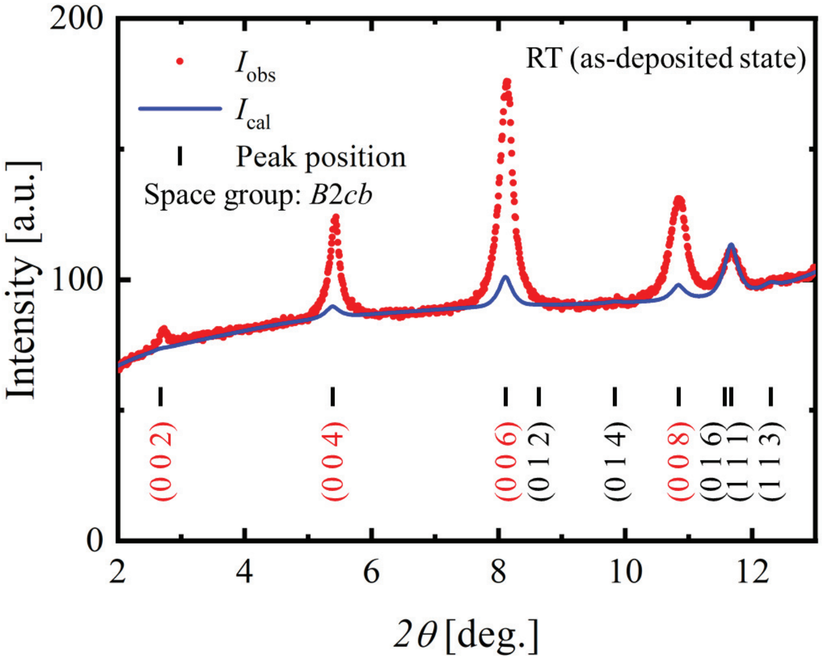

Fig. 2.4.13. Rietveld profile fitting result of the $Bi_4Ti_3O_{12}$ AD film at RT (as-deposited state). The Rietveld analysis was performed using the space group of *B*2*cb*. The red dot, blue line, and | represent the observed intensity, calculated intensity, and peak position, respectively.

A degree of preferred orientation of the BiT AD film at RT (asdeposited state) was roughly estimated. Fig. 2.4.14 shows (a) (004) peak and background diffraction patterns along the Debye−Sherrer ring (β direction) of the BiT AD film at RT (as-deposited state), and (b) peak fitting result of the ((004) peak – background) using the Pseudo-Voigt function. The β scan was performed using the PyFAI library [101]. The degree of preferred orientation A is represented as follows [102]:

$$A = \frac{180 - w}{180} \times 100[\%], \tag{2.4.1}$$

where w is FWHM of the peak. This equation calculates the extent to which the peaks are present within the 180° angular range and will be zero for randomly oriented samples. The degree of preferred orientation of the BiT AD film at RT (as-deposited state) was estimated to be about 67% with $w = 60°$.

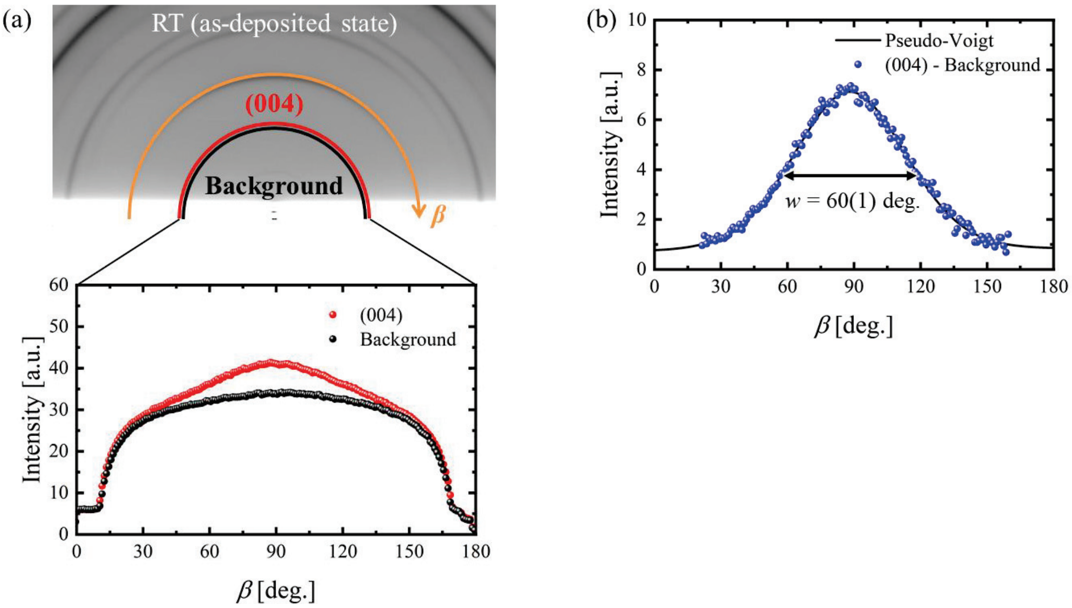

Fig. 2.4.14. (a) (004) peak and background diffraction patterns along the Debye–Sherrer ring (β direction) of the $Bi_4Ti_3O_{12}$ AD film at RT (as-deposited state). (b) Peak fitting result of the (004) peak – background using the Pseudo-Voigt function.

§2.4.3. Temperature dependence of the $Bi_4Ti_3O_{12}$ self-supported film

Figure 2.4.15 shows temperature dependence of the diffraction patterns of the BiT self-supported film for the (a) first cycle and (b) second cycle and (c) the BiT starting powder. The left and right figures show the heating process and cooling process, respectively. Horizontal axis indicates 2θ, vertical axis indicates temperature, and color indicates diffraction intensity. The phase transition temperature T_C for each process were estimated from the rate of change of the d value of the (008) peak, $\Delta d_{(008)}$, expressed as follows:

$$\Delta d_{(008)} = \frac{d^{T}_{(008)} - d^{T_0}_{(008)}}{d^{T_0}_{(008)}}. \tag{2.4.2}$$

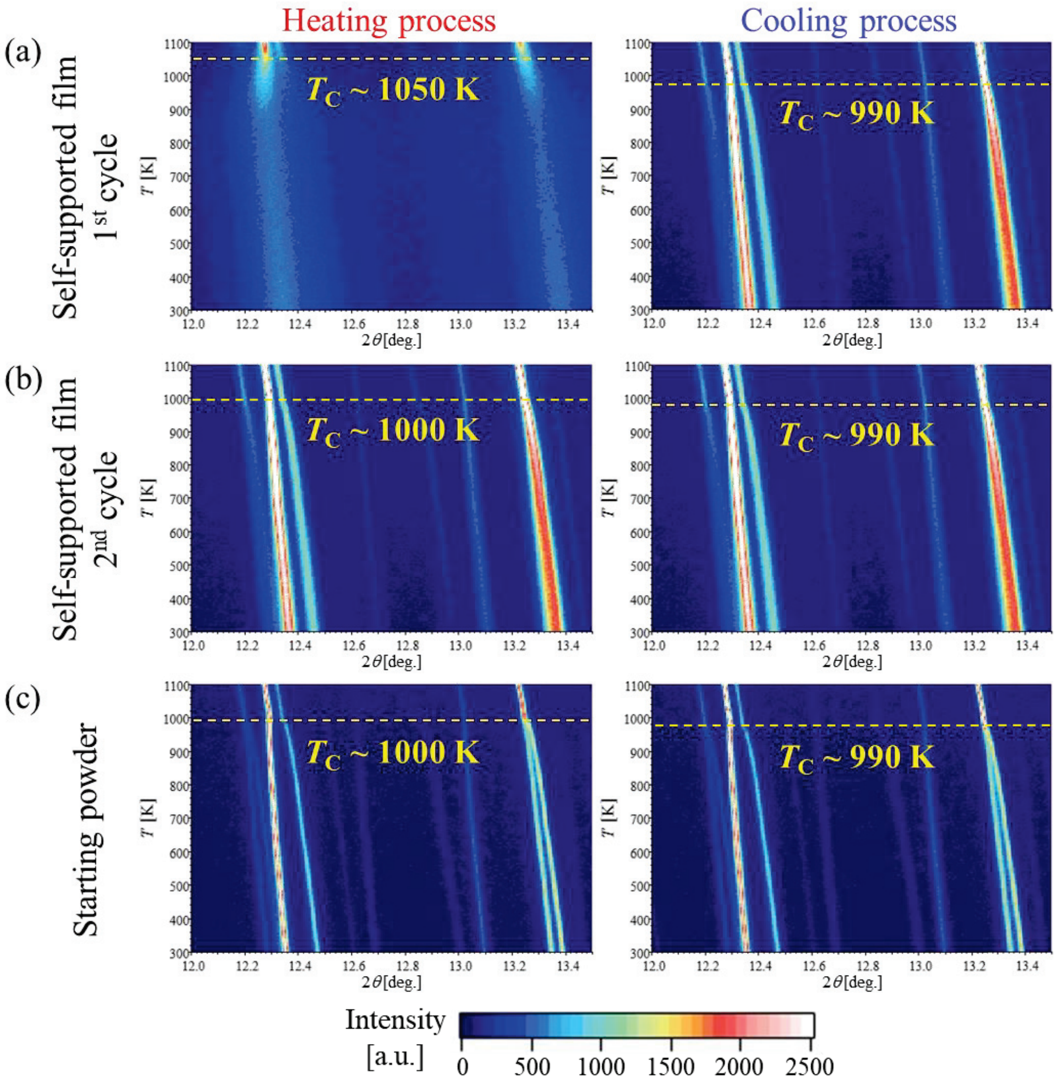

Fig. 2.4.15. Temperature dependence of the diffraction patterns. $Bi_4Ti_3O_{12}$ self-supported film for the (a) 1st cycle and (b) 2nd cycle. (c) $Bi_4Ti_3O_{12}$ starting powder. The left and right figures show the heating process and cooling process, respectively. Horizontal axis indicates 2θ, vertical axis indicates temperature, and color indicates diffraction intensity. Yellow dashed lines indicate the estimated phase transition temperature.

The reasons for choosing the (008) peak are that the (008) peak is a single peak in both the ferroelectric phase and paraelectric phase and that there are no other peaks around it. Fig. 2.4.16 shows the temperature dependence of the (008) peak and $\Delta d_{(008)}$ of the BiT self-supported film for the (a) first-cycle and (b) second cycle and (c) the BiT starting powder. As for the BiT AD film, the peaks of the BiT self-supported film became sharper with increasing temperature although broader than those of the BiT starting powder. T_C

of the BiT self-supported film was found to be higher than that of the BiT starting powder only in the heating process of the first cycle, and almost the same as that of the BiT starting powder in subsequent processes. It is not yet revealed why the T_C of the BiT self-supported film is higher than that of the BiT starting powder only in the heating process of the first cycle. Anyway, it is interesting that the T_C increases, and the ferroelectric order stabilizes in the as-deposited state.

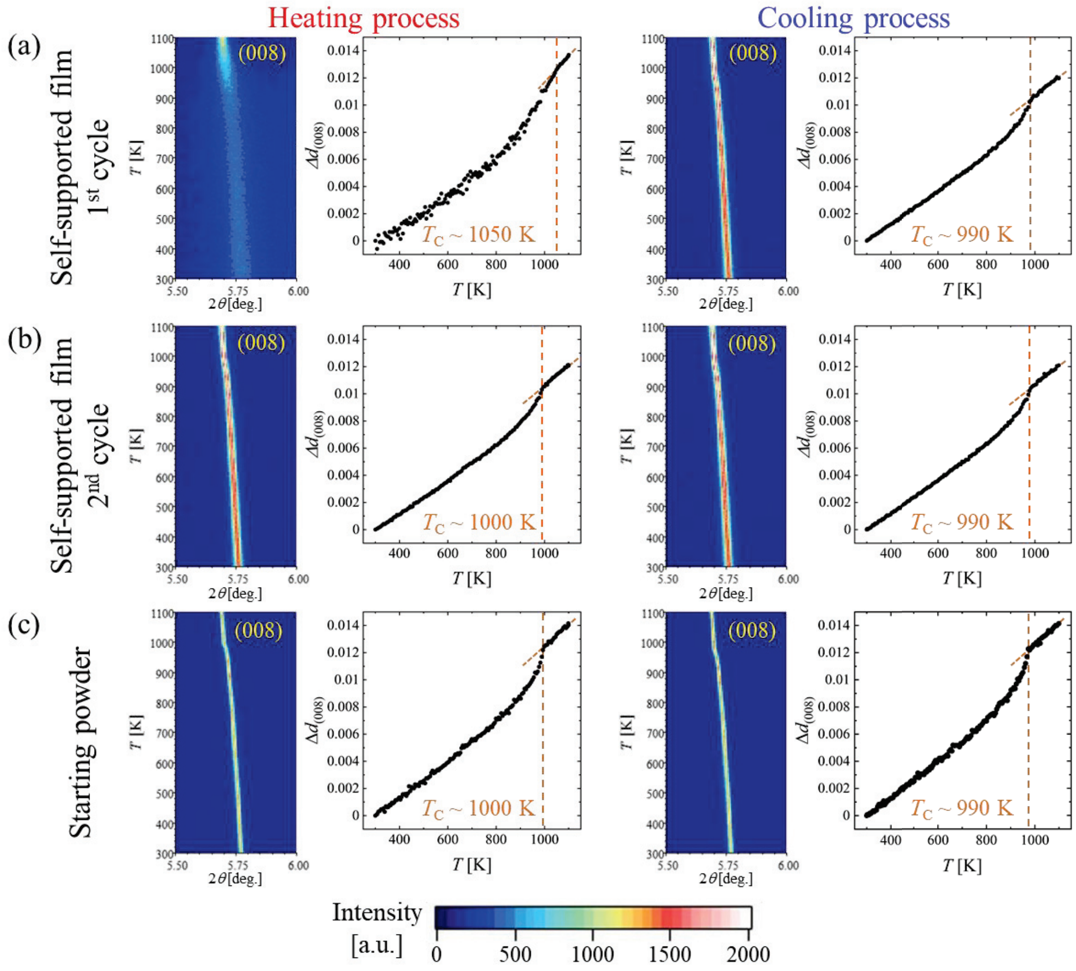

Fig. 2.4.16. Temperature dependence of the (008) peak and $\Delta d_{(008)}$ of the $Bi_4Ti_3O_{12}$ self-supported film for the (a) first-cycle and (b) second cycle and (c) the BiT starting powder.

§2.4.4. Brief summary

In part 2, to confirm the mechanism of the AD method that the plastic deformation of the particles occurs at RT due to particle impact, and a nascent surface is formed on the particle surface, and the nascent surface are recombined to form a dense and transparent ceramic film, the non-plate-like $Bi_4Ti_3O_{12}$ powder was successfully synthesized by the solid-state reaction method as a starting powder.

The chemical bonding nature of the $Bi_4Ti_3O_{12}$ starting powder was characterized by determining the total electron density distribution by analysing synchrotron radiation X-ray powder diffraction data. It has been revealed that the $Bi_4Ti_3O_{12}$ starting powder has an essentially layered crystal structure in both the ferroelectric phase and paraelectric phase.

The orientation characteristics of the $Bi_4Ti_3O_{12}$ AD film was evaluated by synchrotron radiation X-ray diffraction experiments. It has been found that the $Bi_4Ti_3O_{12}$ AD film is *c*-axis oriented even if the starting powder has non-plate like shape, and the *c*-axis orientation of the $Bi_4Ti_3O_{12}$ AD film is not relaxed by heat treatment.

These results indicate that the origin of the *c*-axis orientation of $Bi_4Ti_3O_{12}$ AD films is not the shape, but the layered crystal structure, i.e., the anisotropy of chemical bonds of the starting powder. Therefore, it is suggested that the AD film is formed by the recombination of weakly bound surfaces due to the formation and activation of nascent surfaces on the particle surface by particle impact.

Summary

In this work, structural studies of ferroelectric titanetes were performed using synchrotron radiation X-ray diffraction (SXRD).

In part 1, a method to visualize spatial distributions of only valence electrons, i.e., valence electron density distribution was developed. The valence electron density distributions of perovskite-type ferroelectric $PbTiO_3$ and $BaTiO_3$ in both the paraelectric phase and ferroelectric phase were experimentally determined by analyzing SXRD data with help of first-principes calculations. The determined valence electron density distribution is comparable to the valence electron density distribution obtained by first-principles calculations. In the ferroelectric phase of $PbTiO_3$, Pb is cleary demonstrated to be electronically polarized, which is attributed to the anisotropic spatial distribution of the lone-pair electrons of the Pb ion due to the Pb-O bond. The spontaneous electric polarization of $PbTiO_3$ was estimated by calculating both the ionic polarization and electronic polarization using the valence electron density distribution. The electronic polarization of $PbTiO_3$ accounts for about 33% of the spontaneous polarization, with a particularly large contribution from the Pb ion. In $BaTiO_3$, Ba is fully ionized to Ba^{2+} ion and does not contribute to the ferroelectric phase transition. These results agree with those obtained by first-principles calculations. The chemical bonding natures revealed from the electron density distribution map suggest that in the ferroelectric phase, $PbTiO_3$ has a two-dimensional layered structure, whereas Ba^{2+} ions are located in a three-dimensional network of Ti-O covalent bonds in $BaTiO_3$. The further development of research on materials structure physics is expected by combining the valence electron density analysis and first-principles calculations.

In part 2, the mechanism of the aerosol deposition (AD) method that "when the particle size of the ceramic particles to be sprayed is less than a few microns, the particle collision causes plastic deformation at room temperature, which forms a nascent surface on the particle surface, and the surface recombines resulting in a dense and transparent ceramic film" was confirmed. It was thought that the plate-like shape of the starting powder was the cause of the *c*-axis orientation of $Bi_4Ti_3O_{12}$ AD films. In this study, $Bi_4Ti_3O_{12}$ powder with a non-plate-like shape was prepared as the starting powder, and the orientation characteristics of the $Bi_4Ti_3O_{12}$ AD film was evaluated. $Bi_4Ti_3O_{12}$ powders with non-

plate-like shape were successfully synthesized by a solid-state reaction method. The characteristics of the chemical bonding of the $Bi_4Ti_3O_{12}$ starting powder were investigated from the electron density distribution map. The $Bi_4Ti_3O_{12}$ starting powder was found to have an essentially *c*-axis stacked layered crystal structure. The orientation characteristics of the $Bi_4Ti_3O_{12}$ AD film were investigated by SXRD. The $Bi_4Ti_3O_{12}$ AD film was found to be *c*-axis oriented in the as-deposited state, even though the starting powder was not plate shaped. It was also found that the *c*-axis orientation was not relaxed by heat treatment. These results indicate that the origin of the *c*-axis orientation of the $Bi_4Ti_3O_{12}$ AD film is not the plate-like shape of the starting powder but the layered crystal structure, that is, the anisotropy of the chamichal bonds. Therefore, in the AD method, it is considered that the ceramic films are formed by recombination of weakly bonded planes due to the formation and activation of nascentsurfaces on the particle surface by particle impact at room temperature.

In part 1, $PbTiO_3$ was found to have a two-dimensional layered structure. Therefore, the AD film of $PbTiO_3$ is also expected to be *c*-axis oriented.

Acknowledgement

I would like to express my sincere gratitude to all the people who gave me advice and support throughout this study. Thanks to all of you, I was able to finish my doctoral thesis.

I would like to express my sincere gratitude to Prof. Yoshihiro Kuroiwa. He taught me many things, not only about physical science but also other things. I am grateful for the opportunities he has given me to present my work at national and international conferences.

I would like to express my sincere gratitud to Prof. Chikako Moriyoshi. She taught me many things, including how to proceed with experiments and analysis. She also helped me to prepare presentations for the conferences.

I would like to express my appliciation to Dr. Eisuke Magome. He taught me the basics of experiments and analysis. He also taught me how to teach students when I was a teaching assiatant for student experiments.

I would like to express my appliciation to Dr. Sangwook Kim for his help in submitting the paper.

I would like to express my deepest respect to Prof. Makoto Sakata, Prof. Eiji Nishibori, and Prof. Masaki Takata for establishing the MEM/Rietveld method.

I would like to express my appliciation to Dr. Shogo Kawaguchi, Dr. Kunihisa Sugimoto, and Mr. Michitaka Takemoto, who are the beamline staff at SPring-8, for their help with all the experients at SPring-8. They immediately responded to our suggestions on experimental methods, etc., and helped us to performe the experiments smoothly.

I would like to express my appliciation to Prof. Hiroshi Tanaka and Mr. Yuta Hanato of Shimane University for their help in the valence electron density analysis.

I would like to express my appliciation to Prof. Yuji Noguchi of Kumamoto University for providing us with $PbTiO_3$ single crystals.

I would like to express my appliciation to Dr. Jun Akedo, Dr. Rintaro Aoyagi, Dr. Kentaro Shinoda, and Dr. Muneyasu Suzuki of AIST for providing us with $Bi_4Ti_3O_{12}$ samples and SEM images.

I would like to thank my seniors in the lab, Mr. Shoichi Takeda, Mr. Masaru Ohmoto, Mr. Daichi Tsuru, Ms. Yuki Nakahira, Dr. Zhi-Gang Zhang, and Dr. Qing Zhao. They taught me many things about experiments and analysis, and discussed many things about

our research with me.

I would like to thank Mr Daichi Ichihashi, Mr Yuya Sunada, and Mr. Yu Morita, classmates in the lab. They helped me to discuss about research and to support me in experiments. Ialso have good memories of our dinners together often.

I would like to thank my lab members, Mr Lin Wu, Ms. Mao Hattori, Ms. Misato Hattori, Mr. Hikaru Kaneshima, Mr. Yusuke Yatabe, Mr. Reiji Yamauchi, Ms. Haduki Yoshida, Mr. Takayasu Shigemasu, Mr. Ryohei Matsumura, Mr. Takahiro Hokii, and Ms. Tomoko Hiromi. They have helped me in many ways. They also went out to dinner with me.

Thanks to all of you, I was able to enjoy my life in the laboratory.

Reference

[1] A. Von Hippel, R. G. Breckenridge, F. G. Chesley, and L. Tisza, Ind. Eng. Chem. **38**, 1097 (1946).

[2] B. Wul and I. M. Goldman, C. R. Acad. Sci. USSR **51**, 21 (1946).

[3] 青柳忍, 岡山大学博士論文 (2002).

[4] 寺戸良博, 広島大学博士論文 (2008).

[5] 中村輝太郎，強誘電体と構造相転移　裳華房．76 (1988).

[6] R. D. Shannon, Acta Cryst. A **32**, 751 (1976).

[7] 水流大地，広島大学修士論文 (2017).

[8] R. Blinc and B. Zeks, Soft Modes in Ferroelectrics and Antiferroelectrics, 2 (1974).

[9] A. M. Glazer, Acta Cryst. B **28**, 3384 (1972).

[10] P. M. Woodward, Acta Cryst. B **53**, 32 (1997).

[11] A. von Hippel, Rev. Mod. Phys. **22**, 221 (1950).

[12] G. Shirane, S. Hoshino, and K. Suzuki, Phys. Rev. **80**, 1105 (1950).

[13] F. Jone and G. Shirane, "Ferroelectric Crystals" (Dover Publications, Inc, New York, 1962).

[14] M. E. Lines and A. M. Glass, Principles And applications of ferroelectrics and related materials (Clarendon Press, Oxford 1977).

[15] G. Shirane, R. Pepinsky, and B. C. Frazer, Acta Cryst. **9**, 131 (1956).

[16] H. H. Wieder, Phys. Rev. **99**, 1191 (1955).

[17] V. G. Gavrilyachenko, R. I. Spinko, M. A. Martynen, and R. G. Fesenko, Sov. Phys. Solid State **12**, 1203 (1970).

[18] H. T. Evans, Acta. Cryst. **4**, 377 (1951).

[19] R. J. Nelmes and W. F. Kuhs, Solid State Commun. **54**, 721-723 (1985).

[20] G. Shirane, H. Danner, A. Pavlovic, and R. Pepinsky, Phys. Rev. **93**, 672-673 (1954).

[21] S. Triebwasser, Phys. Rev. **101**, 993-998 (1956).

[22] A. W. Hewat, J. Phys. C: Solid State Phys. **6**, 2559 (1973).

[23] G. A. Samara, T. Sakudo, and K. Yoshimitsu, Phys. Rev. Lett. **35**, 1767 (1975).

[24] R. E. Cohen and H. Krakauer, Ferroelectrics **136**, 65 (1992).

[25] R. E. Cohen, Nature **458**, 136 (1992).

[26] H. Miyazawa, E. Natori, S. Miyashita, T. Shimoda, F. Ishii, and T. OguchiH. Miyazawa, E. Natori, S. Miyashita, T. Shimoda, F. Ishii, and T. Oguchi, Jpn. J. Appl. Phys. **39**, 5679 (2000).

[27] Y. Kuroiwa, S. Aoyagi, A. Sawada, J. Harada, E. Nishibori, M. Tanaka, and M. Sakata, Phys. Rev. Lett. **87**, 217601 (2001).

[28] H. Tanaka, Y. Kuroiwa, and M. Takata, Phys. Rev. B **74**, 172105 (2006).

[29] 石沢伸夫，日本結晶学会誌 **42**, 155-159 (2000).

[30] E. Nishibori, M. Takata, K. Kato, M. Sakata, Y. Kubota, S. Aoyagi, Y. Kuroiwa, M. Yamakata, N. Ikeda, Nucl. Instrum. Methods Phys. Res. A **467-468**, 1045-1048 (2001).

[31] S. Kawaguchi, M. Takemoto, K. Osaka, E. Nishibori, C. Moriyoshi, Y. Kubota, Y. Kuroiwa, and K. Sugimoto, Rev. Sci. Instrum. **88**, 085111 (20017).

[32] E. Nishibori, E. Sunaoshi, A. Yoshida, S. Aoyagi, K. Kato, M. Takata, and M. Sakata, Acta Cryst. A**63**, 43-52 (2007).
[33] H. Kasai and E. Nishibori, Phys. Scr. **91**, 043009 (2016).
[34] H. Kasai and E. Nishibori, Sci. Rep. **7**, 41375 (2017).
[35] M. Takata, E. Nishibori, and M. Sakata, Z. Kristallogr. **71**, 216, (2001).
[36] まてりあ **40**, 267 (2001).
[37] H. M. Rietveld, J. Appl. Cryst. **2**, 65 (1969).
[38] M. Sakata and M. Sato, Acta Cryst. A **46**, 263 (1990).
[39] H. Tanaka, M. Takata, E. Nishibori, K. Kato, T. Ishii, and M. Sakata, J. Appl. Cryst. **35**, 282-286 (2002).
[40] K. Momma and F. Izumi, J. Appl. Cryst. **41**, 653-658 (2008).
[41] A. J. C. Wilson,　INTERNATIONAL TABLES FOR CRYSTALLOGRAPHY Volume C, Dordrecht, Boston, London (1995).
[42] Charles Kittel, Introduction to Solid State Physics 7th ed (1996) §3, John Wiley & Sons, Inc.
[43] 中井泉，泉富士夫編著，日本分析化学会 X 線分析研究懇談会編，粉末 X 線解析の実際-リートベルト法入門，朝倉書店 (2002).
[44] 坂田誠，高田昌樹，西堀英治，固体物理 **35**, 707 (2000).
[45] 高田昌樹，坂田誠，電子顕微鏡 **38**, 104 (2003).
[46] M. Sakata and N. Kato, Acta Cryst. A **42**, 469 (1986).
[47] L. Palatinus and S. van Smaalen, Acta Cryst. A **58**, 559 (2002).
[48] K. Momma and F. Izumi, Z. Kristallogr. Proc. **1**, 195 (2011).
[49] R. Y. De Vries, W. J. Briels, and D. Feil, Acta Cryst. A **50**, 383 (1994).
[50] M. Takata, Acta Cryst. A, **64**, 232, (2008).
[51] T. Hoshina, S. Wada, Y. Kuroiwa, and T. Tsurumi, Appl. Phys. Lett. **93**, 192914 (2008).
[52] T. Hoshina, J. Ceram. Soc. Jpn. **121**, 156-161 (2013).
[53] E. Magome, Y. Kuroiwa, H. Yoshimura, C. Moriyoshi, K. Yamashita, I. Fujii, K. Nakashima, N. Kumada, and S. Wada, Jpn. J. Appl. Phys. **51**, 09LE05 (2012).
[54] J. P. Desclaux, Comp. Phys. Commun. **1**, 216 (1969).
[55] J. P. Desclaux, Comp. Phys. Commun. **9**, 31 (1975).
[56] S. Kitou, T. Fujii, T. Kawamoto, N. Katayama, S. Maki, E. Nishibori, K. Sugimoto, M. Takata, T. Nakamura, and H. Sawa, Phys. Rev. Lett. **119**, 065701 (2017).
[57] S. Kitou, T. Manjo, N. Katayama, T. Shishidou, T. Arima, Y. Taguchi, Y. Tokura, T. Nakamura, T. Yokoyama, K. Sugimoto, and H. Sawa, Phys. Rev. Res. **2**, 033503 (2020).
[58] W. Tang, E. Sanville and G. Henkelman, J. Phys.: Condens. Matter **21**, 0843204 (2009).
[59] J. Akedo, Ceramics **55**, 708-715 (2020) [in Japanese].
[60] J. Akedo, J Therm. Spray Technol. **17**, 181-198 (2008).
[61] D. Hanft, J. Exner, M. Schuber, T. Stocker, P. Fuierer and R. Moos, J. Ceram. Sci. Tech. **06**, 147-182 (2015).
[62] J. Akedo, J. Ceram. Soc. Jpn. **128**, 101-116 (2020).
[63] J. Akedo and M. Lebedev, Jpn. J. Appl. Phys. **38**, 5397-5401 (1999).
[64] J. Akedo, J. Am. Ceram. Soc. **89**, 1834-1839 (2006).

[65] D.-W. Lee, H.-J. Kim, Y.-H. Kim, Y.-H. Yun, and S.-M. Nam, J. Am. Ceram. Soc. 94, 3131-3138 (2011).

[66] M. Yoshida, H. Ogino, S. Nakao, and J. Akedo, Rev. Sci. Instrum. **76**, 093905 (2005).

[67] J. Akedo edit., "Aerosol deposition (AD) process: the basic and applications" CMC publishing (2008) [in Japanese]

[68] J. Iwasawa, R. Nishimizu, M. Tokita, M. Kiyohara, and K. Uematsu, J. Ceram. Soc. Jpn. **114**, 272-276 (2006).

[69] AIST press release,
https://www.aist.go.jp/aist_j/press-release/pr2013/pr20131206/pr20131206.html

[70] SEKISUI CHEMICAL CO., LTD.,
https://www.sekisui.co.jp/news/2017/1302064_29186.html

[71] B.-D. Hahn, J.-M. Lee, D.-S. Park, J.-J. Choi, J. Ryu, W.-H. Yoon, B.-K. Lee, D.-S Shin, and H.-E. Kim, Thin Solid Films **518**, 2194-2199 (2010).

[72] B.-D. Hahn, D.-S. Park, J.-J. Choi, J. Ryu, W.-H. Yoon, B.-K. Lee, and H.-E. Kim, J. Am. Ceram. Soc. **92**, 793-799 (2009).

[73] J. O. Kim, W. Y. Choi, B. K. Choi, and J. T. Jeong, Mater. Sci. Forum **510-511**, 1-4 (2006).

[74] G.-J. Yang, C.-J. Li, S.-Q. Fan, Y.-Y. Wang, and C.-X. Li, J. Therm. Spray Technol. **16**, 873-880 (2007).

[75] W.-H. Yoon, J. Ryu, J-.J Choi, B.-D. Hahn, J. H. Choi, B.-K. Lee, J.-H. Cho, and D.-S. Park, J. Am. Ceram. Soc. **93**, 2125-2127 (2010).

[76] J.-J Choi, J.-H. choi, J. Ryu, B.-D. Hahn, J.-W. Kim, C.-W. Ahn, W.-H. Yoon, and D.-S. Park, J. Arroys Compd. **545**, 186-189 (2012).

[77] J.-J. Choi, J. Ryu, B.-D. Hahn, W.-H. Yoon, B.-K. Lee, J.-H. Choi, and D.-S. Park, J. Am. Ceram. Soc **93**, 1614-1618 (2010).

[78] Y. Iriyama, M. Wadaguchi, K. Yoshida, Y. Yamamoto, M. Motoyama, and T. Yamamoto, J. Power Sources **385**, 55-61 (2018).

[79] J.-J. Park, D.-Y. Kim, S. S. Latthe, J.-G. Lee, M. T. Swihart, and S. S. Yoon, Appl. Mater. Interfaces **5**, 6155-6160 (2013).

[80] Y. Imanaka, N. Hayashi, M. Takenouchi, and J. Akedo, J. Eur. Ceram. Soc. **27**, 2789 (2007).

[81] Y. Imanaka, H. Amada, and F. Kumasaka, Jpn. J. Appl. Phys. **52**, 05DA02 (2013).

[82] J. Akedo, M. Lebedev, H. Sato, and J. Park, Jpn. J. Appl. Phys. **44**, 7072 (2005).

[83] S.-C. Lin and W.-J. Wu, J. Micromech. Microeng. **23**, 125028 (2013).

[84] T. Hoshina, T. Furuta, Y. Kigoshi, S. HattaN. Horiuchi, H. Takeda, and T. Tsurumi, Jpn. J. Appl. Phys. **49**, 09MC02 (2010).

[85] D. Damjanovic, Rep. Prog. Phys. **61**, 1267 (1998).

[86] M. Nakada, K. Ohashi, and J. Akedo, Jpn. J. Appl. Phys. **44**, 6918 (2005).

[87] M. Nakada, K. Ohashi, M. Lebedev, and J. Akedo, Jpn. J. Appl. Phys. **42**, 5960 (2003).

[88] M. Suzuki, J. Ceram. Soc. Jpn. **123**, 9-16 (2015).

[89] M. Suzuki and J. Akedo, J. Ceram. Soc. Jpn. **121**, 664 (2013).

[90] T. Miyoshi, M. Nakajima, and H. Funakubo, Jpn. J. Appl. Phys. **48**, 09KD09 (2009).

[91] M. Suzuki, Y. Nishihara, Y. Uesu, and J. Akedo, Jpn. J. Appl. Phys. **51**, 09LA17 (2012).

[92] M. Suzuki, T. Tsuchiya, and J. Akedo, Jpn. J. Appl. Phys. **56**, 06GH02 (2017).

[93] C. H. Hervohes, and P. Lightfoot, Chem. Mater. **11**, 3359-3364 (1999).

[94] S. E. Cummins, and L. E. Cross, Appl. Phys. **39**, 2268 (1968).

[95] A. D. Rae, J. G. Thompson, R. L. Withers, and A. C. Willis, Acta. Crystallogr. B **46**, 474-487 (1990).

[96] D.Urushihara, M. Komabuchi, N. Ishizawa, M. Iwata, K. Fukuda, and T. Asaka, J. Appl. Phys. **120**, 142117 (2016).

[97] S. J. Kim, C. Moriyoshi, S. Kimura, and Y. Kuroiwa, Appl. Phys. Lett. **91**, 062913 (2007).

[98] K. R. Chakraborty, S.N. Achary, S.J. Patwe, P.S.R. Krishna, A.B. Shinde, and A.K. Tyagi, Ceramics International **33**, 601-604 (2007).

[99] S. E. Cummins and L. E. Cross, J. Appl. Phys. **39**, 2268-2274 (1968).

[100] M. Iwata, C-.H. Zhao, R. Aoyagi, M. Maeda, and Y. Ishibashi, Jpn. J. Appl. Phys. **46**, 5894 (2007).

[101] G. Ashiotis, A. Deschildre, Z. Nawaz, J. P. Wright, D. Karkoulis, F. E. Picca, and J. Kieffer, J. Appl. Cryst. **48**, 510-519 (2015).

[102] Yukiko Namatame and Keigo Nagao, Rigaku Journal **49**, 12-19 (2018) [in Japanese].